

Site-controlled nanostructure fabrication  
by selective area deposition  
through shadow masks

submitted to the Department of Physics  
of the University of Paderborn  
for the degree  
**-Dr. rer. nat.-**

Dissertation

by

Viktoryia Zolatanosha  
from Belarus

Paderborn, January 2020

1. Reviewer: Prof. Dr. Dirk Reuter
2. Reviewer: Prof. Dr. Cedrik Meier

*in memory of my dear grandmother and uncle*

This page has been intentionally left blank

# Contents

	Page
<b>Contents</b>	<b>iv</b>
<b>List of Figures</b>	<b>vii</b>
<b>List of Tables</b>	<b>xiv</b>
<b>List of Abbreviations</b>	<b>xv</b>
<b>Deutsche Zusammenfassung</b>	<b>xvi</b>
<b>Abstract</b>	<b>xvii</b>
<b>1 Introduction</b>	<b>1</b>
1.1 Motivation . . . . .	1
1.2 Thesis overview . . . . .	4
<b>2 Fundamentals</b>	<b>5</b>
2.1 Semiconductors . . . . .	5
2.1.1 Group III-arsenides . . . . .	6
2.2 Epitaxy . . . . .	11
2.2.1 Growth modes . . . . .	12
2.3 Semiconductor nanostructures . . . . .	15

2.3.1	Semiconductor Quantum Dots . . . . .	16
2.3.2	Site-controlled Quantum Dots formed by shadow mask approach. Stranski-Krastanow <i>vs</i> Volmer-Weber growth fashion . . . . .	18
<b>3</b>	<b>Growth and characterization methods of III-V semiconduc- tor nanostructures</b>	<b>25</b>
3.1	Principles of Molecular Beam Epitaxy . . . . .	25
3.1.1	Molecular Beam Epitaxy System . . . . .	28
3.2	Atomic Force Microscopy . . . . .	33
3.3	Scanning Electron Microscopy . . . . .	36
<b>4</b>	<b>Fabrication of Si/Si<sub>3</sub>N<sub>4</sub>-mask</b>	<b>38</b>
4.1	Main description. Technical aspects . . . . .	38
4.2	Mask fabrication procedure . . . . .	42
4.3	Compatibility with UHV system . . . . .	51
4.3.1	Temperature measurement during shadow masked Se- lective Area Epitaxy . . . . .	56
4.3.2	<i>In-situ</i> aperture size reduction . . . . .	60
<b>5</b>	<b>Sample growth and characterization</b>	<b>64</b>
5.1	Selective Area Droplet Epitaxy procedure . . . . .	65
5.2	Key aspects of the deposition through a shadow mask . . . . .	69
5.3	Optimization of a site-controlled droplet formation through the shadow mask . . . . .	79
5.3.1	Pre-coverage layer thickness and its effect on droplet formation . . . . .	82
5.3.2	Coverage layer thickness . . . . .	87
5.3.3	Two-step deposition procedure <i>vs</i> direct deposition at elevated temperatures . . . . .	91

<b>Summary</b>	<b>98</b>
<b>Bibliography</b>	<b>100</b>
<b>Appendix A: Wafer datasheets</b>	<b>116</b>
<b>Appendix B: Mathematical representation of Si (100) etching</b>	<b>118</b>
<b>Appendix C: List of Samples</b>	<b>120</b>
<b>List of Publications</b>	<b>165</b>
<b>Acknowledgements</b>	<b>167</b>

# List of Figures

2.1	The periodic chart of the chemical elements, after [24]. Gallium, aluminum and arsenic are colored in blue, green and red boxes, respectively. . . . .	7
2.2	Crystal structure of GaAs. The bonds are depicted in light gray color. . . . .	8
2.3	The low-temperature energy band gap diagram of different semiconductors with diamond and zinc-blende structures <i>vs</i> their lattice constants, adopted from[29]. Solid lines, as well as dashed lines, denote <i>direct</i> and <i>indirect</i> band gap semiconductors, respectively. The major objective of this thesis, arsenides, are highlighted in <b>black</b> . . . . .	9
2.4	Processes considered for the kinetic description of the epitaxial growth, after[31]. . . . .	11
2.5	Three classical epitaxial growth modes with respect to different coverages in monolayers (ML). Depicted in gray and red are the substrate and deposited layers, respectively. . . . .	13
2.6	Schematic diagram of 3D, 2D, 1D and 0D heterostructures (a) and corresponding DOS of these structures (b). . . . .	16
2.7	Schematics of the DE growth procedure of GaAs QNs, after[60]	20



2.8	Existence range of surface reconstructions forming during the MBE of GaAs depending on growth parameters. Surface reconstructions ( $2 \times 4$ ), $c(4 \times 4)$ and ( $4 \times 6$ ) are highlighted, reproduced after[69] . . . . .	22
2.9	Diagram of the GaAs zinc-blende structure in the (001) direction <b>(a)</b> and side views of the proposed structural models of the GaAs (001) $c(4 \times 4)$ , ( $2 \times 4$ ) and ( $4 \times 6$ ) surface reconstructions <b>(b1)</b> - <b>(d)</b> . Filled and empty circles represent As and Ga, respectively, adopted from[73]-[76]. . . . .	23
3.1	3D-schematic of the III-V MBE system in Paderborn, after [84].	28
3.2	Schematic of the <i>growth</i> and <i>preparation chambers</i> , after [85], [86], [87] . . . . .	29
3.3	Technical drawing of mask and substrate plates, after [88]. . . . .	31
3.4	Working principle of AFM <b>(a)</b> . AFM image of an array Ga droplets <b>(b)</b> deposited through the mask <i>M15-2</i> with $0,23 \mu\text{m}$ openings. . . . .	33
3.5	An example of the surface map of sample A0384. The scratches L1, L2 and L3 pass through alignment markers along the whole sample <b>(a)</b> . Distances d1, d2 and d3 are measured by SEM (see SEM image of a single active window <b>(b)</b> ). As a result, grown structures can be easily found and characterized by AFM knowing the distances between the active areas embedded in the mask design as well as recently measured distances d1, d2 and d3, respectively. . . . .	35
3.6	Schematic of SEM. High-energy electrons are emitted at the gun and focused by two-stage lenses on the sample, after <i>Encyclopaedia Britannica, Inc.</i> 2012 . . . . .	36

4.1	Technical drawings of the mask inside the plate <b>(a)</b> and mask itself <b>(b)</b> , after [104]. The array of squares in the middle of the shadow mask <b>(b)</b> illustrates an active mask region, <b>black</b> squares at the edge are alignment markers. The technical drawings of the mask plate itself can be found in Sections 3.1.1 and 4.3. . . . .	39
4.2	The main sketch of the mask, after [108]. The rectangular hole is etched in <i>Si</i> -wafer through the whole wafer (gray color) and a holey membrane is made on the <i>backside</i> of the wafer (royal blue color). Size of each circular opening is 100 nm. . . . .	41
4.3	The mask fabrication process. The procedure is discussed step by step (from <b>1</b> to <b>9</b> ). . . . .	44
4.4	Photos of <i>Si/Si<sub>3</sub>N<sub>4</sub></i> -mask after applying following steps: <b>(a)</b> OL and RIE on <i>front side</i> of <i>Si</i> -wafer, <b>(b)</b> OL, RIE and KOH on the <i>front side</i> , <b>(c)</b> OL and RIE on the <i>backside</i> . The shiny gray areas are areas of bare <i>Si</i> surface, the royal blue color corresponds to <i>Si<sub>3</sub>N<sub>4</sub></i> layer. . . . .	46
4.5	Laser microscope image of four free-standing <i>Si<sub>3</sub>N<sub>4</sub></i> membranes within the active region. The royal blue and gold colors correspond to <i>Si<sub>3</sub>N<sub>4</sub></i> layer and free-standing <i>Si<sub>3</sub>N<sub>4</sub></i> membranes, respectively . . . . .	47
4.6	A single active window is divided into areas with different hole sizes highlighted in different colors: orange for a 5 μm hole opening with a pitch 10 μm (5 μm/10 μm), pink for 2 μm/5 μm, yellow for 1 μm/3 μm, purple for 0.5 μm/ 1.5 μm, gray for 0.3 μm/ 0.9 μm, blue for 0.2 μm/ 0.8 μm and light green for 0.1 μm/ 0.6 μm, respectively. . . . .	49
4.7	Laser microscope image of the single <i>Si<sub>3</sub>N<sub>4</sub></i> membrane before <b>(a)</b> and after <b>(b)</b> the cleaning procedure. . . . .	50

4.8	The complete mask view. 3D mask sketch is depicted in the middle. The SEM picture <b>2</b> , above the 3D mask sketch, shows the <i>front side</i> of the shadow mask with pyramidal holes. Free-standing holey $Si_3N_4$ membranes are depicted below the sketch in SEM images <b>3</b> . SEM picture <b>4</b> shows an alignment marker. . . . .	52
4.9	Photos of an empty mask holder ( <b>a</b> ), a holder with mask <i>front side</i> view ( <b>b</b> ) and <i>backside</i> view ( <b>c</b> ). Molybdenum ( <i>Mo</i> )-frame and <i>Si</i> -stripes were used to fix the mask inside the holder and push the setback out to allow a close contact between the mask and GaAs substrate during the deposition through the shadow mask procedure. . . . .	53
4.10	The mass spectrum read out during the <i>Si/Si<sub>3</sub>N<sub>4</sub></i> -mask outgassing procedure. The rise in <i>Arsenic</i> , <i>Oxygen</i> and <i>Nitrogen</i> pressures over the time indicates that the outgassing procedure is operating properly: <i>Arsenic</i> is present in the chamber due to the opened As cracker cell as well as some amounts of <i>Nitrogen</i> and <i>Oxygen</i> are usually present in normal MBE usage[122]. $1 \times 10^{-12}$ mbar is used as an indicator of the noise floor. . . . .	55
4.11	Laser microscope images of free-standing holey $Si_3N_4$ membranes before ( <b>a</b> ) and after the deposition of GaAs 100 nm ( <b>b</b> ). The aperture size here is $5 \mu\text{m}$ . . . . .	61
4.12	SEM images of holey mask with the smallest apertures before ( <b>a</b> ), after deposition of 100 nm GaAs ( <b>b</b> ) as well as after re-evaporation procedures ( <b>c</b> ), after [108]. . . . .	62
5.1	Schematics of the shadow masked SAE, after [108]. The distance between the mask and the substrate is <b>d</b> . . . . .	65

5.2	Illustration of the mask-substrate sandwich formation process. This is described step by step from <b>(a)</b> to <b>(f)</b> . . . . .	66
5.3	The coarse <i>Mo</i> -mask <b>(a)</b> . The <i>front side</i> view of the shadow <i>Si/Si<sub>3</sub>N<sub>4</sub></i> -mask after the deposition of alignment markers <b>(b)</b> . . . . .	67
5.4	Examples of growth recipes of sample A0176. In the first recipe, 100 nm of GaAs were deposited with a subsequent Ga-termination of the surface <b>(a)</b> . In the second recipe, 250 nm thick GaAs alignment markers were deposited through the outer part of the shadow mask. This was followed by a Ga deposition of 4.5 ML within the active mask region <b>(b)</b> . . . . .	69
5.5	The influence of the system geometry on the lateral resolution, after [56]. The best pattern transfer can be achieved only for an incoming Ga flux along the mask normal and with no gap present between the mask and the substrate. . . . .	72
5.6	Results of 4.5 ML Ga deposition at different $T_{sub}$ through the 5 $\mu\text{m}$ apertures employing mask <i>M2</i> – 1. Growth protocols can be found in <b>Appendix C</b> . . . . .	75
5.7	Comparison between results of 4.5 ML Ga deposition through the 5 $\mu\text{m}$ apertures with 40 $\mu\text{m}$ mask-substrate gap <b>(a)</b> and in close contact <b>(b)</b> , after [108]. . . . .	76
5.8	Results of 4.5 ML Ga deposition through different aperture sizes from 5 $\mu\text{m}$ down to 100 nm and pitches from 10 $\mu\text{m}$ to 600 nm. . . . .	77
5.9	SEM image of an array of Ga deposits <b>(a)</b> , after [108]. AFM picture of a single local deposit <b>(b)</b> . . . . .	78
5.10	Results of 4.5 ML Ga deposition through 5 $\mu\text{m}$ and 2 $\mu\text{m}$ openings. The deposition was performed with a switched-on <b>(a)</b> and a switched-off cryopump <b>(b)</b> . . . . .	81

5.11 SEM images of local Ga deposits reproducing the mask pattern for every single window in the active membrane region, after [133]. Without deposition of a pre-coverage layer, a strong out-diffusion can be seen <b>(a)</b> . . . . .	82
5.12 AFM images of Ga deposits obtained through 0.34 $\mu\text{m}$ opening. The scan area was $3 \times 3 \mu\text{m}^2$ . The pre-coverage layer thickness was varied from sample A0519 to sample A0522. . . . .	85
5.13 Array of Ga droplets deposited through 0.14 $\mu\text{m}$ openings. The deposition was performed at optimum conditions. . . . .	88
5.14 Results of local Ga deposition through apertures having different sizes. The coverage thickness was varied from 2.75 ML to 40 ML. . . . .	90
5.15 SEM images showing results of Ga deposition in a two-step procedure for two different Ga amounts, after [133]. These results can be compared to results of the depositions through the same aperture sizes but annealed at $T_{anneal}=400 \text{ }^\circ\text{C}$ . . . . .	93
5.16 SEM images of Ga deposits annealed at different $T_{anneal}$ . . . . .	94
5.17 SEM images of Ga deposits deposited at different temperatures. The aperture size is 1 $\mu\text{m}$ . . . . .	95
5.18 Arrays of Ga droplets deposited at $T_{sub}=100 \text{ }^\circ\text{C}$ with a subsequent annealing at $T_{anneal}=400 \text{ }^\circ\text{C}$ <b>(a)</b> and deposited directly at $T_{sub}=400 \text{ }^\circ\text{C}$ <b>(b)</b> . The aperture size in the shadow mask is 0,23 $\mu\text{m}$ . Pre-coverage and coverage layer thicknesses are 1.2 ML and 40 ML, respectively. . . . .	95
5.19 Array of Ga droplets obtained by a deposition through 0,23 $\mu\text{m}$ apertures, after [133]. . . . .	96

5.20	Array of Ga droplets deposited through $0,23 \mu\text{m}$ . SEM images of droplet and hole arrays were combined into one picture <b>(a)</b> . The array of droplets repeats the mask pattern. The spatial dimensions are depicted in <b>(b)</b> . . . . .	97
5.21	Datasheet of <i>Si</i> -wafers supplied for the mask fabrication by <i>CrysTec GmbH</i> . . . . .	116
5.22	Datasheet of GaAs (100) wafers supplied for the sample production by <i>Wafer Technology Ltd.</i> . . . . .	117
5.23	Schematic representation of the etched profile of a square-shaped opening in the mask geometry in <i>Si</i> (100): a sketch of a cross-section of the square groove etched in <i>Si</i> (100) <b>(a)</b> and a SEM image of the square groove itself <b>(b)</b> , respectively. . . . .	119

# List of Tables

2.1	Basic properties of GaAs, AlAs and InAs at 0 K. . . . .	10
4.1	Temperature values for different substrate-mask sandwiches. . .	59
4.2	The aperture diameters before and after the deposition of 100 nm GaAs, as well as after the re-evaporation procedure. . . . .	62
5.1	An estimated Ga coverage <i>vs</i> an aperture size with respect to $S_{membrane}$ . . . . .	71
5.2	Diameters and heights of Ga droplets with respect to aperture sizes and pre-coverage layer thicknesses. . . . .	84
5.3	Structural properties of Ga droplets. The fraction of Ga in the droplets was calculated considering the average droplet volume. For each data set at least 20 droplets were evaluated, after [133]. . . . .	86
5.4	The diameter, height and number of Ga droplets deposited per each aperture size with respect to a deposited Ga coverage layer thickness. . . . .	89

# List of Abbreviations

<b>Abbreviation</b>	<b>Expanded</b>
AFM	Atomic Force Microscopy
AlGaAs	Aluminum Gallium Arsenide
BEP	Beam Equivalent Pressure
EBL	Electron Beam Lithography
HS	Heating Station
KOH	Potassium Hydroxide
MBE	Molecular Beam Epitaxy
ML	Monolayer
$nD$	$n$ -dimensional ( $n= 0, 1, 2, 3$ )
OL	Optical Lithography
PYRO	Pyrometer
QD	Quantum Dot
QN	Quantum Nanostructure
RHEED	Reflection High Energy Electron Diffraction
RIE	Reactive Ion Etching
SADE	Selective Area Droplet Epitaxy
SEM	Scanning Electron Microscopy
$Si_3N_4$	Silicon Nitride
TC	Thermocouple
UHV	Ultra High Vacuum



# Deutsche Zusammenfassung

Die Schattenmasken-gestützte Molekularstrahlepitaxie wurde auf GaAs (100) in *Volmer – Weber*-Form angewandt, um die ortsselektive III-V Halbleiternanostrukturen herzustellen. Bei der ortsselektive Epitaxie-Prozedur wurde Gallium lokal durch die Öffnungen in der Schattenmaske abgeschieden. Indem die Größe der Öffnung mit der mittleren Entfernungscharakteristik für eine selbstorganisierte Nanotröpfchenformation vergleichbar gemacht wurde, war es möglich, ein einzelnes Nanotröpfchen mit hoher Genauigkeit zu positionieren.

Im ersten Teil der Arbeit wurde ein Schattenmaskendesign entwickelt. Die Schattenmaske wurde prozesstechnisch auf Silizium-Basis realisiert. Die Kompatibilität mit dem Molekularstrahlepitaxie-Verfahren wurde nachgewiesen. Zusätzlich wurde eine unschädliche *in-situ* Reinigung der Maskenbehandlung festgestellt.

Im zweiten Teil der Arbeit wurde die Tröpfchenepitaxie-Methode für Schattenmasken-gestützte Epitaxie angepasst. Jeder Tröpfchenepitaxie-Schritt wurde optimiert und mit Rasterelektronenmikroskopie und Rasterkraftmikroskopie analysiert. Die Hauptarbeit bezieht sich auf die Optimierung der Gallium-Abscheidungsparameter. Die Substrattemperatur, die Gallium-Abscheidungsrate sowie die Gallium-Menge wurden ausgewählt, um ein einzelnes Nanotröpfchen pro Öffnung zu erhalten.

# Abstract

Selective area epitaxy employing a movable shadow mask was applied to form site-controlled III-V semiconductor nanostructures on GaAs (100) in *Volmer – Weber* fashion by molecular beam epitaxy. In selective area epitaxy procedure, gallium is deposited locally through apertures in the shadow mask. By making the size of the aperture comparable to the mean distance characteristic for a self-assembled nanodroplet formation, it is possible to position of a single nanodroplet with high accuracy.

This requires two major steps, a shadow mask fabrication and an optimization of the droplet epitaxy method for a shadow masked selective area epitaxy. For that, the shadow mask design is developed. This is realized on silicon/silicon nitride-basis in terms of silicon process technology. Its compatibility with molecular beam epitaxy procedure is proven. In addition, a gentle *in-situ* cleaning of the mask treatment is found. Consequently, the droplet epitaxy method is adapted for a shadow masked selective area epitaxy. Due to the droplet epitaxy itself is a multi-step growth procedure, every single step is improved and analyzed separately using both scanning electron and atomic force microscopy. The optimization of the gallium deposition parameters is performed. A substrate temperature, a gallium deposition rate, as well as a gallium amount, were selected to obtain a single nanodroplet per aperture occupancy.

# Chapter 1

## Introduction

### 1.1 Motivation

Nanometer-sized III-V semiconductors in general and quantum dots (QDs) in particular have been a subject of intense study for the past decades due to their electrical and optical properties[1]. These properties can be tuned by controlling nanostructure morphology[2]. III-V semiconductor nanostructures have found a variety of applications in electronic and optoelectronic devices, including transistors, lasers, photodetectors and solar cells[3], [4], as well as in the field of quantum information science, where single photon sources are key resources[5], [6].

Therefore, the development of techniques allowing a defect-free nanostructure fabrication is a key interest for many research groups. Currently, several fabrication techniques already exist. They can be classified as ‘top-down’ and ‘bottom-up’ methods. In contrast to the ‘bottom-up’ approach typically being favored due to the combination of several lithography and etching steps, the ‘top-down’ one degrades the material quality leading to deteriorated physical properties of nanostructures. At the moment, the most promising fabri-

cation technique is molecular beam epitaxy (MBE), which provides precise control of the composition and dimensionality of semiconductor nanostructures with high growth procedure purity.

Selective area epitaxy (SAE) approach was developed to enhance the capacity of the conventional MBE procedure[7]. The SAE can be performed as a growth either on pre-patterned substrates[8] or through a shadow mask[9]. The patterned SAE is a well-established technique for *in-situ* fabrication of QDs on predefined places[10]. In patterned SAE, lithography and etching procedures are used for patterning either a mask overlayer, e. g.,  $SiO_2$ , or a substrate itself. The growth of nanostructures then only takes place in the areas not covered with the shadow mask. Self-organization concepts, orientation-dependent growth rates, as well as a migration enhancement from areas with the mask towards non-covered ones, force the nanostructure formation on predefined places. During patterned SAE, the substrate is directly involved in the time-consuming procedures of patterning, etching and cleaning. This leads to an increase in undesired substrate contamination probability. In its turn, shadow masked SAE is an approach with higher flexibility, but due to its complicity, only several groups have demonstrated the potential of this method[11], [12] and it has not been yet implemented into the site-controlled growth of QDs. The idea to use once fabricated shadow mask during all growth campaigns as well as to have an opportunity to clean it *in-situ* looks very promising.

Thereby, the objective of this thesis is a fabrication of site-controlled nanostructures *via* shadow masked SAE approach. For that, robust shadow masks on silicon/ silicon nitride ( $Si/Si_3N_4$ )-basis were successfully fabricated by several lithography and etching steps. The mask was designed to have several apertures, where the smallest ones should force a single nanostructure formation on predefined by aperture area places. The fabricated masks were thoroughly cleaned, and their compatibility with an epitaxial growth proce-

ture was examined.

This thesis not only includes the mask fabrication but, additionally, the site-controlled growth of III-V semiconductor nanostructures has to be accomplished in terms of shadow masked SAE. The presence of the mask underneath the substrate during deposition stages imposes certain technological requirements to the growth procedure itself. First of all, the control of the substrate temperature, material fluxes, as well as surface reconstructions, becomes complex and, at some point, impossible to implement. Well-established growth of QDs on lattice-mismatched substrates in *Stranski – Krastanov* fashion, e. g., InAs QDs on GaAs (100), is not the first choice here as it demands a good control the substrate temperature as well as group III and group V fluxes[13]. In contrast to that, a droplet epitaxy (DE) is a unique growth technique that can be successfully applied to fabricate a rich variety of nanostructures[14]. Unlike conventional epitaxy, which uses simultaneous delivery of elements both groups (III and V) to the substrate surface, the unique DE growth protocol allows the separation of groups III and V elements. In other words, the metal group III nanodroplets are formed during the first stage, and at the second one they are crystallized using group V flux. As a result, DE has several advantages over the growth *via Stranski – Krastanov* mode, such as its wide growth temperature range and capability of fabrication different types of nanostructures from both lattice-matched and lattice-mismatched systems[15].

DE growth technique was successfully implemented into the shadow masked SAE procedure. As a result, group III metal nanodroplets were formed during the droplet formation stage in predefined by shadow mask places. The main growth parameters, such as a substrate temperature, a deposition rate and an amount of group III were optimized in order to reach a single nanodroplet occupancy for the case, where the deposition was performed through the smallest mask apertures. For that, all optimization experiments were

performed on GaAs (100) with GaAs/ $\text{Al}_x\text{Ga}_{1-x}\text{As}$  material system, i. e., gallium (Ga) was deposited through the apertures in the shadow mask either on GaAs or  $\text{Al}_x\text{Ga}_{1-x}\text{As}$  (100) surfaces depending on the purpose of the growth campaign.

## 1.2 Thesis overview

In the present chapter, the motivation for starting this work was given. Chapter 2 outlines the relevant background for the rest of the thesis. Specifically, basic concepts related to III-V semiconductor nanostructure and its fabrication are discussed. The third chapter gives a brief description of the growth and characterization techniques used in this thesis.

Chapter 4 discusses the mask design and its fabrication procedure. In addition, the mask compatibility with the ultra-high vacuum (UHV) system is proven as well. Chapter 5 is reserved for details concerning the selective area droplet epitaxy (SADE) itself and for an optimization of growth parameters obligatory for a site-controlled formation of III-V semiconductor nanostructures employing such an approach.

Finally, the results are summarized in the last chapter. As an integral part of this thesis, supplementary information is provided in several appendices. In Appendix A, wafer datasheets are supplied. In Appendix B, the mathematical representation of  $S_i$  (100) etching process in potassium hydroxide (KOH) is described, which is, in particular, relevant for redesigning the shadow mask. In the last Appendix C, the growth protocols are given, which contain important information regarding the MBE growth: substrate temperatures, background pressures, deposition rates and Ga amounts at different deposition stages.

# Chapter 2

## Fundamentals

This introductory chapter prepares the ground for the rest of the thesis. The description of the basic concepts related to semiconductor nanostructures is presented in the following pages.

Section 2.1 gives a brief survey of semiconductors and their properties, in particular, of arsenide-based semiconductors. Section 2.2 is reserved for a description of the general principles of the epitaxy process, which are mainly used for the fabrication of III-V compound semiconductors. Section 2.3 introduces the concept of a nanostructure in general and a quantum dot in particular with a subsequent literature review of recent developments in quantum dot fabrication, especially in the droplet epitaxy, as in major objective of this thesis.

### 2.1 Semiconductors

The historic development of semiconductor physics and technology began in the second half of the 19th century, starting from the discovery of semiconductor properties of PbS by *T.J. Seebeck*[16], [17]. In 1947, the realization

of the first transistor by *William Shockley, John Bardeen* and *Walter Brattain* at the *Bell Labs* was the impetus to a fast development that created the electronics and photonics industries[16], [18]. However, in between these two events much work of several scientists lie.

The term ‘Halbleiter’ (a semiconductor in English) was introduced for the first time by *J. Königsberger* and *J. Weiss*[16], [19]. Since that time semiconductors have been, and are, used in various forms: as mechanically cut slices from a single crystal ingot **i**, as thin crystal films **ii** deposited on suitable substrates by chemical or physical deposition processes, as glass-like elements **iii**, as polycrystalline or glassy thin films **iv** [20]. In the great majority of these applications, an essential part of the process is concerned with growing a high-quality bulk single-crystal either to serve directly as an active material or to act as a substrate for epitaxial film growth[20]. This, therefore, requires a subsequent development of the crystal growth industry.

Digressing from the general consideration of electronic structure, semiconductors are observed in the periodic table between metals of the *column* 13, appearing to the left side, and non-metals of the *column* 15, appearing to the right side (see Figure 2.1). As a result, they have intermediate properties between metals and non-metals. Under a close look, *column* 14 in the periodic chart is a location of the elemental semiconductors of group IV, i. e., *Si* and germanium (Ge) (see Figure 2.1). Although *Si* is still the most dominant in the electronics, the compound semiconductors III-V and II-IV also exist and are successfully implemented into a device fabrication. One of the most widely used compound semiconductors is gallium arsenide (GaAs), which, itself and its alloys, are the research objectives of this thesis.

### 2.1.1 Group III-arsenides

III-V compound semiconductors are widely used as materials for optoelec-



PERIOD

GROUP

1 1.008 H HYDROGEN 2 4.0026 He HELIUM

3 6.94 Li LITHIUM 4 9.0122 Be BERYLLIUM 10 20.180 Ne NEON

11 22.990 Na SODIUM 12 24.305 Mg MAGNESIUM 13 10.81 B BORON 14 12.011 C CARBON 15 14.007 N NITROGEN 16 15.999 O OXYGEN 17 18.998 F FLUORINE 18 39.948 Ar ARGON

19 39.098 K POTASSIUM 20 40.078 Ca CALCIUM 21 44.956 Sc SCANDIUM 22 47.867 Ti TITANIUM 23 50.942 V VANADIUM 24 51.996 Cr CHROMIUM 25 54.938 Mn MANGANESE 26 55.845 Fe IRON 27 58.933 Co COBALT 28 58.693 Ni NICKEL 29 63.546 Cu COPPER 30 65.38 Zn ZINC 31 69.723 Ga GALLIUM 32 72.64 Ge GERMANIUM 33 74.922 As ARSENIC 34 78.971 Se SELENIUM 35 79.904 Br BROMINE 36 83.798 Kr KRYPTON

37 85.468 Rb RUBIDIUM 38 87.62 Sr STRONTIUM 39 88.906 Y YTIORIUM 40 91.224 Zr ZIRCONIUM 41 92.906 Nb NIObIUM 42 95.95 Mo MOLYBDENUM 43 (98) Tc TECHNETIUM 44 101.07 Ru RUTHENIUM 45 102.91 Rh RHODIUM 46 106.42 Pd PALLADIUM 47 107.87 Ag SILVER 48 112.41 Cd CADMIUM 49 114.52 In INDIUM 50 118.71 Sn TIN 51 121.76 Sb ANTIMONY 52 127.60 Te TELLURIUM 53 126.90 I IODINE 54 131.29 Xe XENON

55 132.91 Cs CAESIUM 56 137.33 Ba BARIUM 57-71 La-Lu Lanthanide 72 178.49 Hf HAFNIUM 73 180.95 Ta TANTALUM 74 183.84 W TUNGSTEN 75 186.21 Re RHENIUM 76 190.23 Os OSMIUM 77 192.22 Ir IRIUM 78 195.08 Pt PLATINUM 79 196.97 Au GOLD 80 200.59 Hg MERCURY 81 204.38 Tl THALLIUM 82 207.2 Pb LEAD 83 208.98 Bi BISMUTH 84 (209) Po POLONIUM 85 (210) At ASTATINE 86 (222) Rn RADON

87 (223) Fr FRANCIUM 88 (226) Ra RADIUM 89-103 Ac-Lr Actinide 104 (267) Rf RUTHENIUM 105 (268) Db DUBNIUM 106 (271) Sg SEABORGIUM 107 (272) Bh BOHRIUM 108 (277) Hs HASSIUM 109 (276) Mt MEITNERIUM 110 (281) Ds DARMSTADIUM 111 (280) Rg ROENTGIUM 112 (285) Cn COPERNICIUM 113 (285) Nh NIHOIUM 114 (287) Fl FLEROVIUM 115 (289) Mc MOSCOVIUM 116 (291) Lv LIVERMORIUM 117 (294) Ts TENNESSE 118 (294) Og OGANESSON

Copyright © 2017 Eri Generale

LANTHANIDE

57 138.91 La LANTHANUM 58 140.12 Ce CERIUM 59 140.91 Pr PRASEODYMIUM 60 144.24 Nd NEODYMIUM 61 (145) Pm PROMETHIUM 62 150.36 Sm SAMARIUM 63 151.96 Eu EUROPIUM 64 157.25 Gd GADOLINIUM 65 158.93 Tb TERBIUM 66 162.50 Dy DYSPROSIUM 67 164.93 Ho HOLMIUM 68 167.26 Er ERBIUM 69 168.93 Tm THULIUM 70 173.05 Yb YTTERBIUM 71 174.97 Lu LUTETIUM

ACTINIDE

89 (227) Ac ACTINIUM 90 232.04 Th THORIUM 91 231.04 Pa PROTACTINIUM 92 238.03 U URANIUM 93 (237) Np NEPTUNIUM 94 (244) Pu PLUTONIUM 95 (243) Am AMERICIUM 96 (247) Cm CURIUM 97 (247) Bk BERKELIUM 98 (251) Cf CALIFORNIUM 99 (252) Es EINSTEINIUM 100 (257) Fm FERMIUM 101 (258) Md MENDELEVIUM 102 (259) No NOBELIUM 103 (262) Lr LAWRENCIUM

Figure 2.1: The periodic chart of the chemical elements, after [24]. Gallium, aluminum and arsenic are colored in blue, green and red boxes, respectively.

tronic devices, such as light-emitting diodes, laser diodes and photodetectors, as well as for electronic transport devices, such as field-effect transistors, high electron mobility transistors and heterojunction bipolar transistors [21]-[23]. GaAs, aluminum arsenide (AlAs), indium arsenide (InAs) and various alloys on their basis provide examples of III-V compound semiconductors. Generally speaking, in III-V compound semiconductors, one element comes from group III of the periodic table and the other one from the group V. Furthermore, the bonding in III-V compounds is similar to the elemental semiconductors so that the electron deficiency of the group III element is compensated by extra electrons of the elements of the group V. As a result, such semiconductors have essentially the same electronic structures as elemental ones. Crystal structure, the type of bonding in a solid and, ultimately, the

electron wave functions are the key parameters defining electronic properties of the III-V compound semiconductors[25].

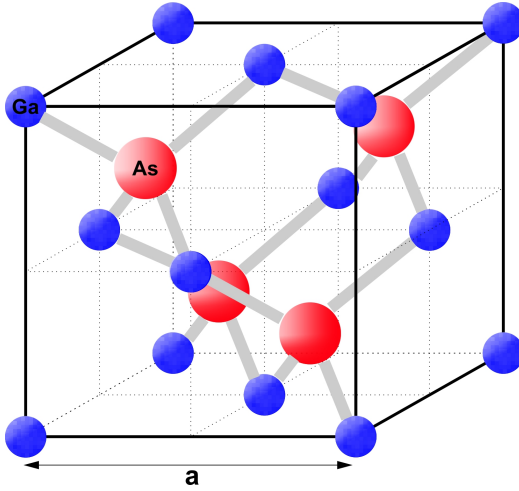


Figure 2.2: Crystal structure of GaAs. The bonds are depicted in light gray color.

The arsenide-based III-V semiconductors have a zincblende (sphalerite, ZnS) structure. In the zincblende structure, the base of the primitive unit cell consists of two atoms, which generally have different polarity and are located at  $(0,0,0)$  and  $(1,1,1) \times \frac{a}{4}$ , where  $a$  is the lattice constant[26]. In other words, the structure is composed of a face-centered cubic (*fcc*) lattice of cations and a *fcc* lattice of anions, which are represented by blue and red spheres in Figure 2.2, respectively, and are displaced by a quarter of the cube diagonal, i. e., by  $\frac{\sqrt{3}}{4} \times a$ [26]. This results in a tetrahedral bond configuration, so that each ion is tetrahedrally surrounded by four ions of the opposite polarity, as depicted in Figure 2.2.

In the III-V compound semiconductors the mixture of elements on *fcc* sublattices in zincblende crystal can be varied. This, in general, affects the material properties. As an example, in the ternary compound  $Al_xGa_{(1-x)}As$ , the composition of the alloy can be varied by choosing the molar fraction of Al or Ga atoms (the group III element). Thus, according to the empirical *Vegard's rule*[27], the lattice constant of  $Al_xGa_{(1-x)}As$ ,  $a_{0,Al_xGa_{(1-x)}As}$ , can be derived from the lattice constants of both materials AlAs,  $a_{0,AlAs}$ , and GaAs,  $a_{0,GaAs}$ , which have the same crystal structure, and is given by the following relation:

The arsenide-based III-V semiconductors have a zincblende (sphalerite, ZnS) structure. In the zincblende structure, the base of the primitive unit cell consists of two atoms, which generally have different polarity and are located at  $(0,0,0)$  and  $(1,1,1) \times \frac{a}{4}$ , where  $a$  is the lattice constant[26]. In other words, the structure is composed of a face-centered cubic (*fcc*) lattice of cations and a *fcc* lattice of anions, which are represented by blue and red spheres in Figure 2.2, respectively, and are displaced by a quarter of the cube diagonal, i. e., by  $\frac{\sqrt{3}}{4} \times a$ [26]. This results in a tetrahedral bond configuration, so that each ion is tetrahedrally surrounded by four ions of the opposite polarity, as depicted in Figure 2.2.

$$a_{0,Al_xGa_{(1-x)}As} = xa_{0,AlAs} + (1-x)a_{0,GaAs} \quad (1)$$

In its turn, the band gap of the ternary compound semiconductor  $E_{g,Al_xGa_{(1-x)}As}$  is given by

$$E_{g,Al_xGa_{(1-x)}As} = xE_{g,AlAs} + (1-x)E_{g,GaAs} - bx(1-x) \quad (2)$$

where  $E_{g,AlAs}$  and  $E_{g,GaAs}$  are the band gaps of AlAs and GaAs, respectively, and  $b$  is a bowing parameter. The bowing parameter value at the  $\Gamma$ -point for  $Al_xGa_{(1-x)}As$  is given by relation  $b = 0.127 + 1.310x$ [28].

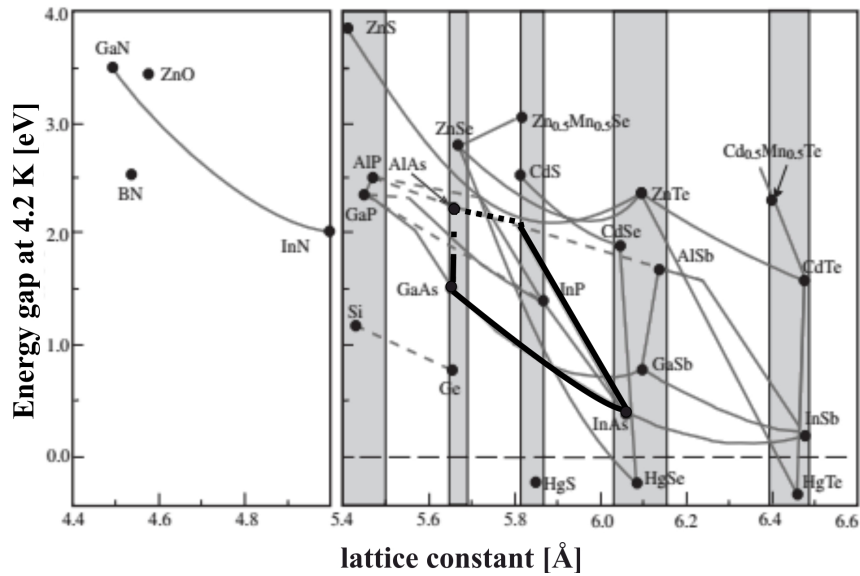


Figure 2.3: The low-temperature energy band gap diagram of different semiconductors with diamond and zinc-blende structures *vs* their lattice constants, adopted from[29]. Solid lines, as well as dashed lines, denote *direct* and *indirect* band gap semiconductors, respectively. The major objective of this thesis, arsenides, are highlighted in **black**.

Table 2.1: Basic properties of GaAs, AlAs and InAs at 0 K.

property	GaAs	AlAs	InAs
direct energy gap $E_g$ [eV]	1.519	3.099	0.417
zincblende lattice constant $a_0$ [Å]	5.643	5.661	6.050

Figure 2.3 represents values of low-temperature energy band gaps  $E_g$  and lattice constants  $a_0$  for various diamond and zincblende semiconductors, as well as their alloys. The gray zones highlight several families of semiconductors, which have similar lattice constants. Thus, upon a closer examination of material properties of GaAs and AlAs (see Table 2.1), nanostructures on their base, especially  $Al_xGa_{(1-x)}As$ , can be described as a strain-free, because lattice constants of these two materials are almost identical, e. g., the misfit is 0.33 % at 0 K. In contrast, the misfit in InAs/GaAs system is 6.74 %.

Due to an increase of the Al molar fraction in ternary  $Al_xGa_{(1-x)}As$  alloy tends to change the type of semiconductor from a *direct* band gap semiconductor to an *indirect* one with subsequent changes of its electrical and optical properties, only alloys with molar fractions below 0.33 are studied in this thesis.

All samples in this thesis are grown on GaAs (100) wafers by molecular beam epitaxy (MBE). The explanation of the epitaxy process as well as the MBE technique itself and the MBE system used for the sample growth in this thesis, are presented in the following Sections 2.2, 3.1 and 3.1.1, respectively. Important material parameters, such as lattice constants and band gap energies of GaAs, AlAs and InAs are listed in Table 2.1.

## 2.2 Epitaxy

*Louis Royer* introduced the term *epitaxy* from the Greek  $\epsilon\pi\iota$  (*epi*, upon, attached to) —  $\tau\alpha\xi\iota\sigma$  (*taxis*, arrangement, order) and concluded its general rules[26]. Inherently, *epitaxy* refers to a growth of a new crystalline layer on a crystalline substrate, where such a layer is oriented with respect to the substrate[30]. It may either be performed close to the thermodynamic equilibrium using, e. g., liquid phase epitaxy, or far away from the equilibrium using, e. g., MBE. Consequently, the growth of a crystalline solid itself represents a transition between two phases (vapor or liquid) to a crystalline phase and proceeds by an attachment of particles (atoms or molecules) to the substrate surface[26]. This process, undoubtedly, requires a force to drive particles from one phase of the system across the interface zone towards a solid phase. Such a driving force is a difference in the chemical potential between the phases[26].

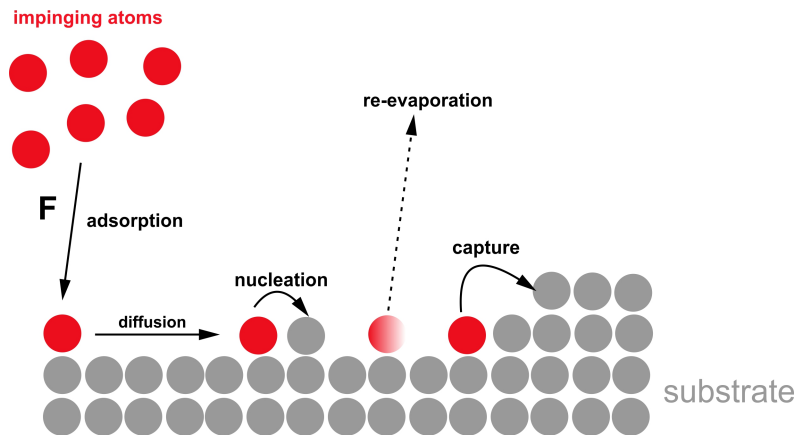


Figure 2.4: Processes considered for the kinetic description of the epitaxial growth, after[31].

The growth process can be described as a number of consecutive steps, as depicted in Figure 2.4. In the atomistic model, impinging atoms arrive from

the material source at an externally controlled flux  $\mathbf{F}^1$  and are adsorbed on the surface[26]. Atoms may then diffuse over the surface until they meet other atoms to nucleate/ to be attached to existing islands or to defects, e. g., steps on the surface, or they re-evaporate/ dissolve in case of a liquid ambient[26]. Each single thermally activated kinetic process of epitaxy, i. e., a diffusion, a re-evaporation or a dissolution, is governed by characteristic parameters entering an Arrhenius dependence with an activation energy  $E$  and may be expressed using its rate equation[26]

$$\tau^{-1}(T) = \nu_0 e^{-\frac{E}{k_B T}} \quad (3)$$

where  $E$  is the barrier, which has to be surmounted in the process, the prefactor  $\nu_0$  is the attempt-rate constant for each given process,  $k_B$  is the Boltzmann constant and  $T$  is the temperature. As a particular example, the process of atom diffusion can be expressed concerning the diffusion coefficient, which is described as  $D = \nu e^{-\frac{E_d}{k_B T}}$ , where  $E_d$  and  $\nu$  are the surface diffusion activation energy and the vibrational frequency, respectively. The vibrational frequency is given by  $\nu = \frac{2k_B T}{h}$ , where  $h$  is the *Planck* constant[26].

The described above system is simplified. Therefore, contributions from surface reconstructions, interdiffusion processes, as well as chemical reactions between the substrate and deposited material, are neglected.

### 2.2.1 Growth modes

As mentioned before, the crystalline layer growth is performed by the attachment of atoms to the substrate surface. In the initial stage of the epitaxial growth, a formation of small clusters on the substrate is required. Such clusters of atoms form nuclei of the solid on the substrate surface. When the stable nuclei are formed, the crystal starts to grow according to the conditions

---

<sup>1</sup>can be described as the number of atoms per unit area and per unit time

controlled by properties of the applied phase transition and adjusted growth parameters[26], [32]. The nucleation and growth processes, themselves, are characterized by a growth mode, which depends on various parameters, such as the driving force **i** and the misfit between substrate and the layer **ii**.

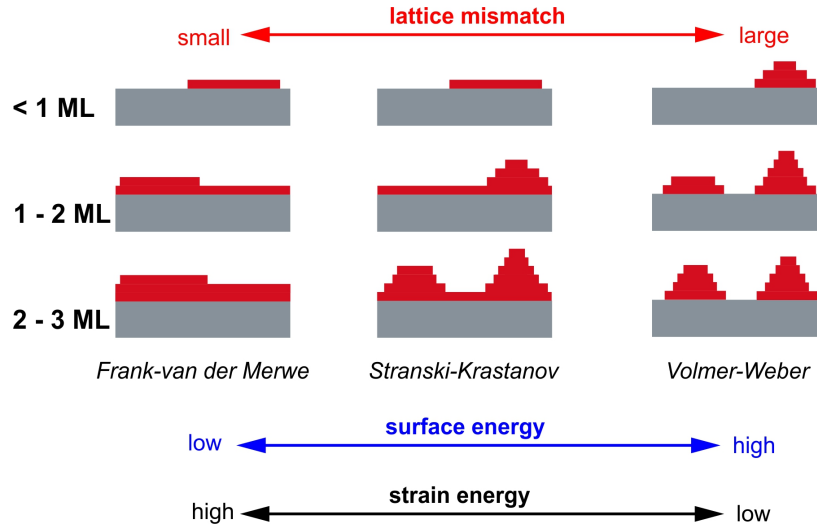


Figure 2.5: Three classical epitaxial growth modes with respect to different coverages in monolayers (ML). Depicted in gray and red are the substrate and deposited layers, respectively.

The depicted in Figure 2.5 growth modes arise from a thermodynamic consideration of the interface energies[26], [34]. The balance of interface tensions<sup>2</sup> at the line of contact between the three phases of metastable ambient (index  $a$ ), nucleus ( $n$ ) and substrate ( $s$ ) is given by three quantities, which represent the energies needed to create an unit area of each of the three interfaces[26]. Young's relation for the absolute values of tensions in balance is

$$\gamma_{as} = \gamma_{ns} + \gamma_{an} \cos\theta \quad (4)$$

<sup>2</sup>surface tension  $\gamma$  is defined as a work required to build a surface of unit area

if a nucleus with the shape of a spherical cap on the substrate is assumed[26].

In general, the epitaxy aims a layer deposition with a smooth growth surface, i. e., this means that a wetting angle in Young's relation (4) is 0 or  $\gamma_{as} = \gamma_{ns} + \gamma_{an}$ [26].

If this condition applies or  $\gamma_{as}$  exceeds the sum of the two other interface energies, so that Young's relation reads as  $\gamma_{as} \geq \gamma_{ns} + \gamma_{an}$ , the complete wetting of the grown layer onto the substrate surface is obtained[26]. For atoms in the layer, this means that they are more strongly attracted to the substrate than to themselves. Thus, the growth may then proceed in an atomically flat two-dimensional (2D) layer-by-layer growth referred to as *Frank – Van der Merve* growth mode[35]. Such a growth mode is the most preferable in epitaxy, as it provides growth of smooth planar films. However, crystals are not perfect and contain defects, which can be spread over macroscopic distances due to a continuity of the growth in *Frank – Van der Merve* fashion[33]. The optimum homogeneity of grown layers can be initiated by a precise controlled small angle misorientation of the substrate[36].

In contrast to that, different surface morphology of the grown layer is observed if layer atoms are more strongly attracted to each other than to the substrate[26]. This situation is expressed in Young's relation (4) by a wetting angle of  $\pi$ , or  $\gamma_{ns} = \gamma_{as} + \gamma_{an}$ , so that the grown layer does not wet the substrate surface. As a result, 3D island growth is obtained on the substrate, which is referred to as *Volmer – Weber*[37]. The growth proceeds as follows: in the first stage of the growth a large number of surface nuclei are formed, and in the second one, they spread. Such a growth mode is mainly used to fabricate self-assembled 3D quantum nanostructures (QNs)<sup>3</sup> by DE technique. This is used as the main growth technique in this thesis and further

---

<sup>3</sup>QDs, quantum dot molecules, nanorings, nanodots and so on



described in detail in Sections 2.3.2 and 5.1.

Often the intermediate *Stranski – Krastanov* growth mode is found, also termed as a layer-plus-island growth[38]. Here, the condition for *Frank – Van der Merve* growth applies solely for the first deposited MLs and after exceeding a certain value of the coverage (critical thickness) the growth changes to the *Volmer – Weber* case[26]. The critical thickness lies below the value, which is required for the formation of misfit dislocations, so that *Stranski – Krastanov* growth is widely used in recent years as an approach for a fabrication of defect-free QDs, especially in InAs/GaAs(100) material system[39].

## 2.3 Semiconductor nanostructures

The unique properties of low-dimensional structures essentially originate from the modification of the electronic density-of-states (DOS) produced by the confinement of charge carriers[26].

A solid (3D), when confined in all three spatial dimensions (0D) to length scales comparable to or smaller than the electron *de Broglie* wavelength  $\lambda_{deBroglie}$ <sup>4</sup>, gives a rise to discrete electron energy levels[39]. As a result, such structures acquire new and unique electronic and optical properties, which are not found in solid structures confined in only one direction (1D), i. e., a quantum well, or two directions (2D), i. e., a quantum wire. These structures are usually called QDs and they represent a particular class of semiconductor nanostructures[40]. The confinement can be realized by embedding a semiconductor material into another one having a larger band gap.

---

<sup>4</sup> $\lambda_{deBroglie} = \frac{h}{3m^*k_B T}$ , where  $h$ ,  $m^*$ ,  $k_B$  and  $T$  are the Planck constant, the effective mass, the Boltzmann constant and the temperature, respectively[43]

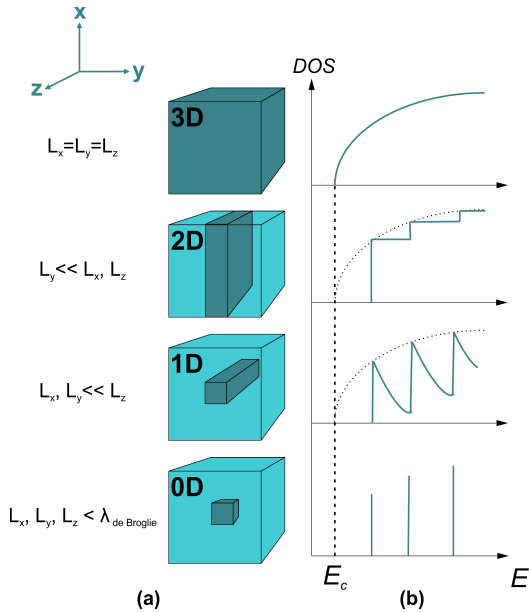


Figure 2.6: Schematic diagram of 3D, 2D, 1D and 0D heterostructures (a) and corresponding DOS of these structures (b).

Due to the reduction of the semiconductor size, the energy levels and DOS follow the quantum size effect and behave accordingly[41]. In a bulk semiconductor material, the charge carriers behave like free carriers in all three directions because length scales of semiconductor in all three dimensions are much larger than the wavelength of the charge carriers, i. e., *de Broglie* wavelength. For 2D, 1D and 0D confinement cases, as well as for bulk material, the DOS are schematically shown in Figure 2.6 (b), where  $E_c$  is the lower edge of the conduction band.

QDs are often called as superatoms or artificial atoms due to their sharp DOS,[42]. Obviously, they are much bigger than real atoms. The lateral dimensions for the QDs are usually in a range of several tens nanometers, while the *Bohr* radius is just  $a_B \approx 0.5\text{\AA}$ .

### 2.3.1 Semiconductor Quantum Dots

Over the last decades semiconductor QDs have gained much interest due to their electronic properties[43], [44]. Among QD fabrication techniques developed since its discovery, the most promising approach is a fabrication of defect-free QDs in a self-assembled manner *via Stranski – Krastanov* growth fashion. Such QDs are highly attractive due to possibility to use

them in optoelectronics: many devices use arrays of randomly distributed self-assembled QDs because the spatial order of QDs is not required, e. g., QD lasers[45]. In contrast to that, for novel advanced single QD devices, such as single photon[46] or single-electron[121] turnstile devices, the precise control over the QD position in an array plays a critical role, since it defines a further high integration of the whole device unit[44]. Hence, techniques for a single QD positioning or a perfect QD arrangement into an array have to be developed.

Several approaches to order self-assembled QDs were proposed and realized. Usually, all of them are based on a regular nucleation of QDs on the artificially modulated surfaces. Regular QD arrays were realized by controlling the nucleation sites on nanohole arrays prepared by electron-beam lithography (EBL)[48], [49]. Site-controlled QDs, in turn, were successfully fabricated using *in-situ* scanning tunneling microscope- (STM-Probe-Assisted)[50],[51] or atomic force microscope-assisted (AFM-Probe-Assisted)[92] methods. The artificial modulation of the surface creates difficulties in the formation of high-quality structures because a contamination of the substrate during preparation steps leads to a corresponding deterioration of the QD quality.

The use of a shadow mask to define patterns on a substrate is very attractive compared to all aforementioned approaches. Once fabricated the shadow mask can be used many times for an *in-situ* translation of the mask pattern onto the substrate. The main added value of this technique is that it does not rely on photoresist processes, so no multi-step preparations are applied to the substrate, as a result, no defects are induced in the crystal growth. Obviously, the effectiveness of such mask will depend on the mask-surface contact, a mask thickness, edge effects, the mask alignment on the surface and the mask cleanliness itself.

The approach to use shadow masks for the deposition on isolated areas is not

new. In 1984 *G. Kaminsky from AT & T Bell Laboratories* has described the fabrication of mechanical shadow masks for an *in-situ* stripe definition of thin films in MBE[53]. In subsequent years, the lead chalcogenide buried heterostructure lasers were successfully fabricated using the growth through a *Si* shadow mask and showed similar properties to those of photolithographically obtained. The mask-substrate contact does not appear to affect the laser properties[54]. In addition, *Shunsuke Ohkouchi and others* designed a mask for selective growth of InAs QDs in narrow regions[55]. These results show that the proposed approach employing a shadow mask allows a *in-situ* selective growth of semiconductor structures by MBE technique. The emphasis in the aforementioned studies is made on that the openings in shadow masks are greater than 4  $\mu\text{m}$ . Thus for the formation of site-controlled QDs, the mask design, as well as deposition parameters, have to be optimized in order to reach the aperture sizes comparable to the mean distance characteristic for a self-assembled QD formation, i. e., 100 - 200 nm.

### **2.3.2 Site-controlled Quantum Dots formed by shadow mask approach. Stranski-Krastanow *vs* Volmer-Weber growth fashion**

The use of a shadow mask for a site-controlled QD fabrication by MBE imposes certain requirements not only on the mask but on the deposition process itself. On the one hand, the mask must be non-contaminative and compatible with MBE processes (deposition, heating and cooling steps under ultra high vacuum (UHV) conditions). On the other hand, the geometry of the deposition system plays not the latest role: it defines the quality of the pattern transfer from the mask to the substrate. Important parameters here are: a source width **i**, a source-mask distance **ii**, a mask-substrate gap **iii** and the angle of the incoming material flux **iv**[56]. The best pattern transfer

can be achieved for an incoming flux of the material along the normal of the mask with no gap present between the mask and the substrate[56]. Although a good pattern transfer has been demonstrated despite the presence of a separation between the mask and the substrate, it can limit the quality of the pattern transfer, depending on the angle of an incoming material with the mask and the material diffusivity on the substrate [57], [58]. In case of a single dot per aperture occupancy it may have a huge effect. A characterization study of the influence of the mask-substrate gap on dimensions of grown structures is planned and further described in Section 5.2. Depending on the deposited material and its amount, apertures in the shadow mask can be slowly decreased in size due to clogging. This limits a quality of the pattern transfer as well as the re-usability of the mask itself. Efforts have to be made to develop *in-situ* cleaning procedures.

Taking into account aforementioned information, an implementation of the shadow mask approach into a fabrication of site-controlled QDs in *Stranski–Krastanov* fashion looks problematic. This is mainly due a physical nature of processes involved in the QD formation *via Stranski – Krastanov* mode. QDs formed by *Stranski – Krastanov* are very sensitive to the substrate temperature as well as In and As flux changes. Typical temperature during the QD formation stage lie in the range from 490 °C to 520 °C[43],[59]. At the same moment, In and As fluxes have also certain constant values[43]. Due to the presence of the shadow mask with tiny holes underneath the substrate during the QD formation stage, the control of the real substrate temperature as well as In and As fluxes will be intricate. As a result, either a way to control the main growth parameters or an another method of the QD fabrication has to be found and implemented.

The fabrication of QDs employing DE is an interesting alternative to a well-established technology of a strain-driven QD formation in *Stranski – Krastanov* fashion, due to a splitting of groups III and V material supply

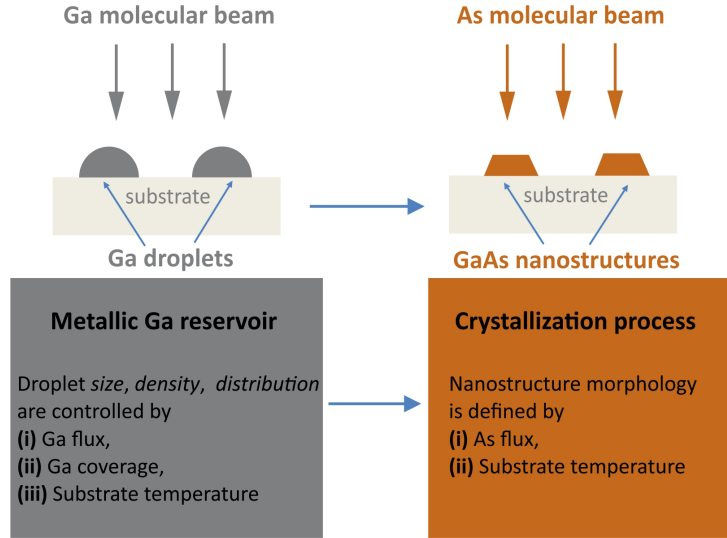


Figure 2.7: Schematics of the DE growth procedure of GaAs QNs, after[60]

during a QD formation[60]. The concept of the DE was proposed for the first time by *Koguchi* and co-workers in 1990[61] and named ‘droplet epitaxy’ by *Koguchi* and *Ishige*[62].

They presented a completely new growth protocol, which is based on a two-step procedure, as depicted in Figure 2.7:

1. In the first stage, nanometer-sized droplets are formed on the substrate surface by supplying a sufficient molecular beam of a group III element, e. g., Ga, in a group V-free environment, e. g., in As-free atmosphere.
2. In the second one, the substrate is exposed to the group V element, so that the metallic nanodroplets are crystallized to III-V QNs, e. g., GaAs QNs.

In this thesis only GaAs/ $Al_{0.3}Ga_{0.7}As$  (100) material system is described and investigated. In such a case, two fundamental steps are a liquid Ga droplet deposition on  $Al_{0.3}Ga_{0.7}As$  surface **i** and a subsequent crystallization of Ga

droplets to GaAs QNs **ii**. Consequently, these steps have to be described in detail.

The Ga droplet nucleation requires the deposition of an initial Ga coverage, which will be incorporated at the surface[64]. This process can be understood in terms of surface reconstructions. Due to the similarity of the surface symmetry of  $Al_xGa_{1-x}As$  and GaAs, the surface reconstructions of  $Al_xGa_{1-x}As$  have the same real space structure as GaAs so that the following discussion focuses on surface reconstructions of GaAs[65]. Different surface reconstructions of GaAs are presented with respect to growth conditions<sup>5</sup> in Figure 2.8.

Generally, the initial surface reconstruction under the typical DE conditions and right before the opening of Ga source is As-rich  $c(4 \times 4)$  (see Figure 2.9 **(b1)**, **(b2)**). This is usually produced by cooling down a  $(2 \times 4)$  (see Figure 2.9 **(c1)** - **(c4)**) reconstructed surface in As presence, but can also be observed under rather extreme growth conditions of a high As/Ga flux and low substrate temperatures[70]. The initial arrangement then evolves into the  $(2 \times 4)$  reconstruction after the deposition of 1 ML and finally is converted into  $(4 \times 6)$  (see Figure 2.9 **(d)**), after the supply at least Ga coverage of 1.75 ML[66].

These findings have to be compared with the reported As coverage of the different surface reconstructions:  $c(4 \times 4)$ , in its  $\alpha$ - and  $\beta$ -phases, has an As coverage of 1.28 - 1.61 ML[71], while the  $(2 \times 4)$  in its  $\beta$ - and  $\beta_2$ -phases of 0.75 ML[72] and the  $(4 \times 6)$  of 1/12 ML[60]. This information confirms the need for the establishment of  $(4 \times 6)$  reconstruction on  $Al_xGa_{1-x}As$  before the formation of Ga droplets. Thus, as long as a Ga-rich surface reconstruction is not established on the  $Al_xGa_{1-x}As$  surface, Ga atoms will

---

<sup>5</sup>substrate temperature and beam equivalent pressure (BEP) ratios of the As and Ga fluxes

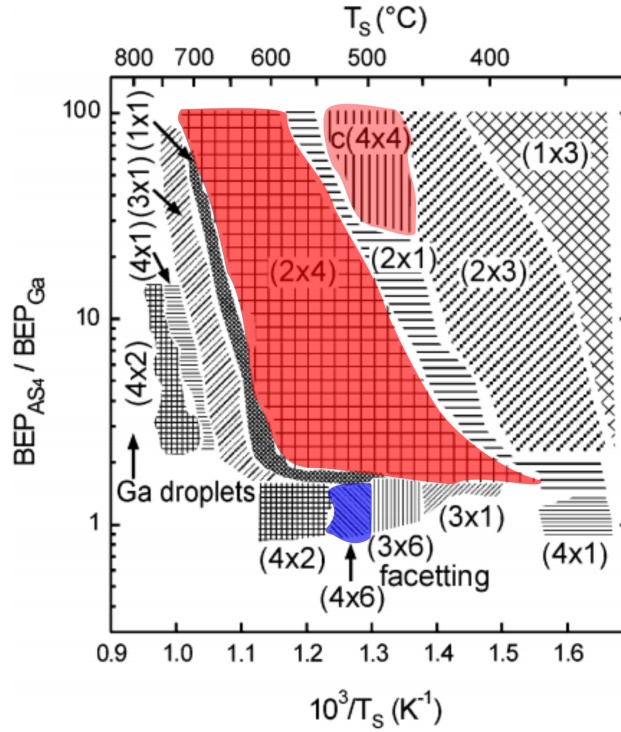


Figure 2.8: Existence range of surface reconstructions forming during the MBE of GaAs depending on growth parameters. Surface reconstructions  $(2 \times 4)$ ,  $c(4 \times 4)$  and  $(4 \times 6)$  are highlighted, reproduced after[69]

try to saturate the bonds to As. Only after this, on the top of the Ga-rich surface reconstruction  $(4 \times 6)$ , the droplet formation is possible. This has a great importance, since it permits to understand what is the minimum Ga amount that should be deposited to nucleate Ga droplets.

Once the Ga-rich surface is established, the Ga droplet formation takes place in the *Volmer – Weber* fashion if the excess of Ga exists. There are several parameters which control the Ga droplet density and size distributions: the substrate temperature and Ga flux[67]. The temperature dependence can be easily understood in terms of the temperature-dependent surface diffusion co-



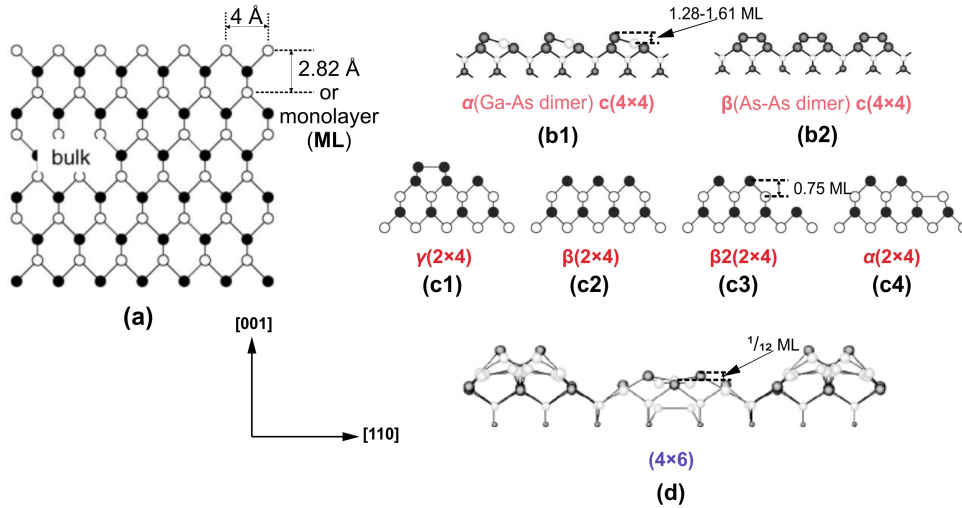


Figure 2.9: Diagram of the GaAs zinc-blende structure in the (001) direction (a) and side views of the proposed structural models of the GaAs (001)  $c(4 \times 4)$ ,  $(2 \times 4)$  and  $(4 \times 6)$  surface reconstructions (b1) - (d). Filled and empty circles represent As and Ga, respectively, adopted from[73]-[76].

efficient of atoms[15]. The general trend is a dramatic decrease of the droplet density with increase of the substrate temperature: the density of droplets follows a classical nucleation scaling law at low temperatures; however, a coarsening by Ostwald ripening has to be taken into consideration at high temperatures[68]. This means that Ga droplet deposition parameters<sup>6</sup> have to be found and optimized for the special case of a site-controlled droplet formation employing a shadow mask with different apertures. Details on the optimization process are presented in Section 5.3.

As a final step, an As irradiation of Ga droplets can be applied to convert them into GaAs QNs. During this procedure, metallic Ga contained in each droplet is crystallized in the form of a QN with a large variety of shapes depending on crystallization parameters[15], [60]. Thus, a QN morphology is

<sup>6</sup>Ga amount and its deposition rate as well as a substrate temperature

determined by the exact crystallization conditions: a substrate temperature **i** and an As flux **ii**. The crystallization step is omitted in this thesis so further information can be found in relevant studies.

As a summary, the DE technique has emerged as an alternative to the most frequently used *Stranski – Krastanov* approach and has several advantages compared to that[63]:

1. viable on different substrates, e. g., Si, Ge, GaAs and *etc.*,
2. both lattice-matched and latticed-mismatched materials are allowed for a barrier and QNs, e. g., GaAs/ $Al_xGa_{1-x}As$  or InAs/GaAs,
3. an independent control over QN density and size distributions,
4. a QN shape engineering, allowing also complex structures,
5. a low thermal budget QN fabrication,
6. QNs can be grown without wetting layer, which is present in a layer-plus-island growth.

## Chapter 3

# Growth and characterization methods of III-V semiconductor nanostructures

This chapter is dedicated to a brief description of the growth and characterization techniques used in this thesis.

The first part of the chapter starts with an explanation of the main molecular beam epitaxy principles. As follows, details on technical aspects of the MBE system used in this thesis for a sample fabrication are given. The second part offers a concise description of the *ex-situ* characterization methods. For structural analysis of the grown structures atomic force microscopy and scanning electron microscopy were mainly used.

### 3.1 Principles of Molecular Beam Epitaxy

Although the name MBE was used for the first time in 1970[31], the history of MBE was started a few years before it[77]. The early stages of the MBE

development were initially reviewed by *J. R. Arthur* and *A. Y. Cho* for the growth of GaAs and GaAs/Al<sub>x</sub>Ga<sub>1-x</sub>As material systems[78], [79]. During the following decades, it has been implemented to grow successfully a wide variety of materials[77].

MBE itself is an advanced crystal growth technique playing a remarkable role in the fabrication of novel semiconductor devices[60]. This technique is based on the mass transport in molecular or atomic beams in an UHV environment<sup>1</sup>. At this conditions, nearly no collisions can occur between the particle beam and the residual gas in the chamber. The BEP during the depositions is normally kept low enough to prevent the particle collisions in the beam itself. The molecular beams are generated by the thermal heating of materials, having an ultra-high purity, in material sources, called effusion cells. The atoms evaporated from effusion cells react with each other and the substrate surface. This results in a formation of epitaxial layers according to the mechanisms explained in Section 2.2.

Usually, the MBE system is constructed as an assembly of chambers and pumps, where chambers and pumps are interconnected by valves to permit an isolation between different parts of the system. The *growth* and *transfer chambers* are always in the UHV regime. The pumping efficiency therein is achieved by a combination of several types of pumps: a cryopump **i** and/or ion gettering and titanium sublimation pumps (IGP/TSP) **ii**. The *load lock* chamber is typically constructed so that it can be vented separately without the breaking of the vacuum in the rest part of the MBE system. The pumping in the *load lock* is maintained by the teamwork of membrane and turbo pumps.

In addition to the key components, several viewports located in different parts of the system are used for process and sample transfer observation.

---

<sup>1</sup>background chamber pressure lies below 10<sup>-9</sup> mbar

They are generally equipped with a mechanical shutter to prevent ‘fogging’ by evaporated materials.

As mentioned above, during the epitaxial growth a single or multiple beams transport atoms from the material sources to the heated and rotated or non-rotated substrate. A radiative heater with a thermocouple (TC) is used to heat the substrate and measure its temperature during preparation and growth procedures. In addition, the substrate temperature control is also performed by pyrometer (PYRO). Frequently used PYROs allow a quite precise temperature measurement in a wide temperature range[80]. In its turn, the substrate rotation is applied to obtain a largely homogeneous deposition.

Molecular fluxes are measured by a movable beam flux monitor (BFM) gauge, which measures BEPs of the in-coming fluxes with high accuracy. The effusion cell construction allows the control of the molecular flux by the setting of the cell temperature, i. e., the higher the source temperature the higher the flux of out-coming atoms and, as follows, the higher the deposition rate. The mechanical shutters, located above the material sources, block the molecular beams if necessary. In addition, the substrate shutter located below the plate holder may also be included in the chamber construction.

UHV regime allows for *in-situ* control of the epitaxial growth *via* an electron beam-based diagnostic tools: reflection high-energy electron diffraction (RHEED), low-energy electron diffraction or Auger electron spectroscopy. RHEED is the most demonstrative tool to characterize the sample surface during the epitaxial growth as well as to regulate growth parameters. The recording of the RHEED oscillations during the deposition allows the direct measurement of the deposition rates[81].

As a summary, the MBE has advantages compared to other growth techniques[60]:

1. Due to slow growth rates ( $1 \mu\text{m}/\text{hour}$ ), it provides a precise control of

the layer thickness, a composition and a dopant concentration.

2. UHV environment, maintained inside the growth system allows an *in-situ* use of the electron beam-based diagnostic tools to study growth processes.
3. MBE growth is typically performed with extremely pure elementary materials, which are enclosed inside the *growth chamber*. Thus, MBE is a comparably safe semiconductor fabrication method.

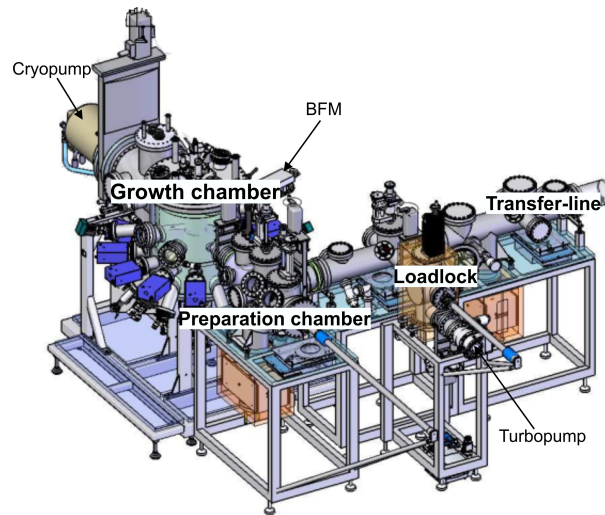


Figure 3.1: 3D-schematic of the III-V MBE system in Paderborn, after [84].

### 3.1.1 Molecular Beam Epitaxy System

3D-schematic of the solid-source III-V system, which was used in this thesis, is presented in Figure 3.1. This system is an assembly of four vacuum chambers: *growth chamber i*, *preparation chamber ii*, *transfer – line iii* and *load lock iv*. All three chambers, except the *load lock*, have a base pressure

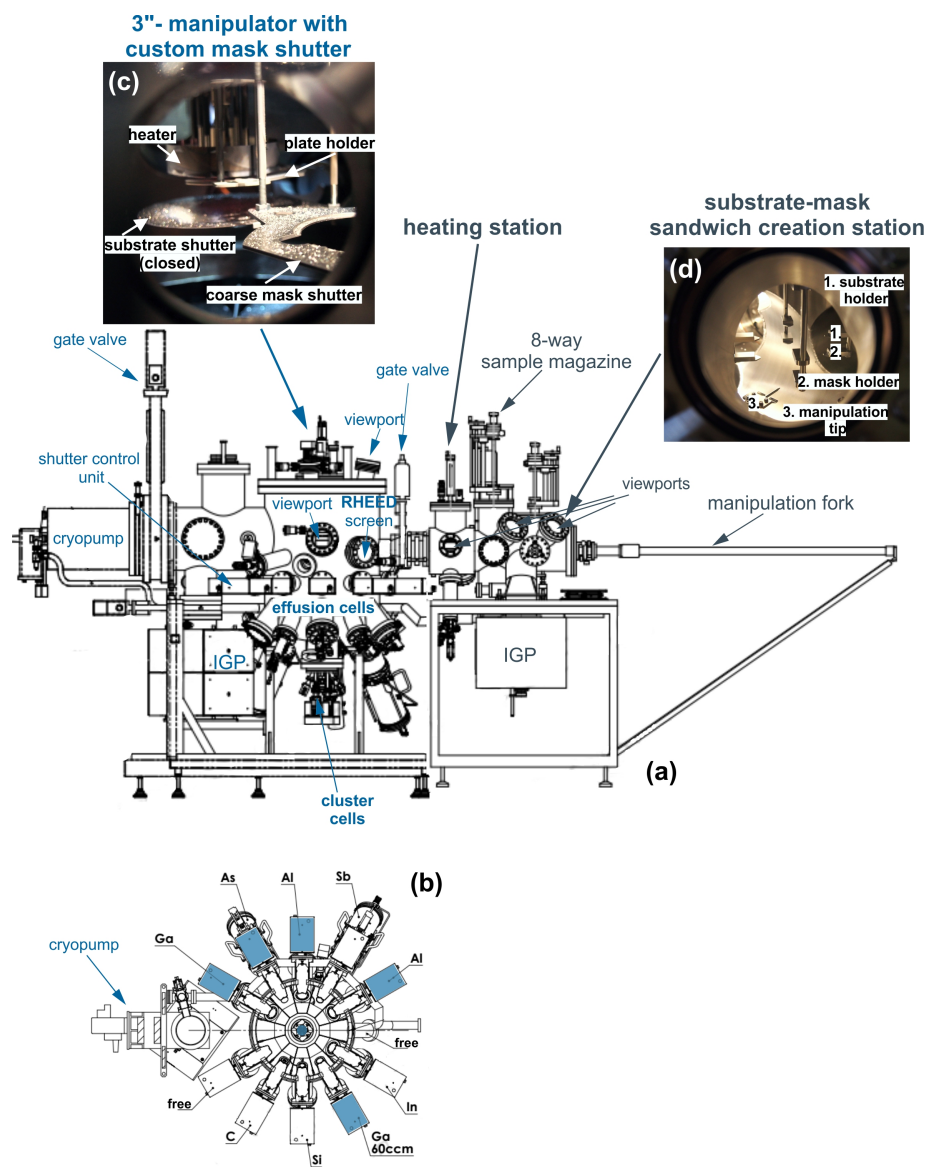


Figure 3.2: Schematic of the *growth* and *preparation chambers*, after [85], [86], [87]

below  $10^{-10}$  mbar and stay at the UHV condition for the most duration of the growth campaign. Gate valves between chambers separate different parts of the system.

The *load lock* chamber is pumped with a combination of turbo and membrane pumps and achieves the pressure of  $5 \times 10^{-8}$  mbar. Implementation of the membrane pump prevents any penetration of the pump oil inside the chamber. All pumps, which are used in the MBE system, are oil-free to prevent any possibility of the chamber contamination with organic materials. The *load lock* is used to transfer samples in and out of the MBE system without venting the other MBE chambers. This is equipped with a 6-way magazine allowing loading up to 6 wafers, substrates or masks, at once. Every time the wafers are loaded, the *load lock* is pumped and degassed for 8 hours at 120 °C. Such a procedure minimizes the contamination of the whole system.

The degassed samples are transferred to the *preparation chamber* using *transfer – line* trolley. The *transfer – line* train has 4 places so that 4 wafers can be stored simultaneously within the chamber. The vacuum in *transfer – line* is maintained with IGP/TSP.

The *preparation chamber*, as shown in Figure 3.2 (a), is equipped with an atomic hydrogen cleaning unit and a heating station (HS) used for substrate or mask cleaning. The HS heater allows a heating of the substrate up to 1000 °C[82]. In this thesis, it was mainly used to degas substrates or masks before loading them into the *growth chamber*. The maximum degassing temperature for such purpose is not exceeding 550 °C for the mask and 200 °C for the substrate, respectively. The *preparation chamber* itself has an 8-way magazine for the storage of 8 samples simultaneously. In addition, this is equipped with a substrate-mask sandwich creation station (see Figure 3.2 (d)), where the mask can be attached or removed to the substrate under



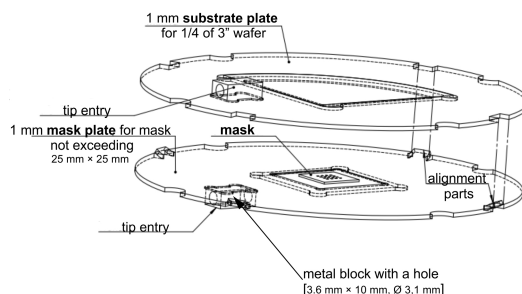


Figure 3.3: Technical drawing of mask and substrate plates, after [88].

UHV conditions. For such purpose, the substrate and mask plates were customized and their technical drawings are presented in Figure 3.3. The particular procedure of a substrate-mask sandwich creation is discussed step by step in Section 5.1.

The vacuum in the *growth chamber* is achieved and maintained by an assembly of pumps: a closed-cycle helium cryopump, liquid nitrogen-cooled IGP/TSP as well as liquid nitrogen-filled cryo-shrouds surrounding the chamber and effusion cells on the vacuum side. The substrate, mask or substrate-mask sandwich is loaded to the manipulator by a linear transfer rot with a special manipulation fork. The photo of the 3 inch manipulator is shown in Figure 3.2 (c). Besides the standard equipment: the heater, plate holder brackets and substrate shutter, manipulator has a coarse mask shutter that allows a manual loading and positioning of a coarse shadow mask. Such a coarse mask can be designed to shadow desired parts of the substrate during deposition or doping procedures. The tantalum wire heater is used to heat the substrate. It allows heating of the substrate up to 1250 °C[83]. The maximal temperature, which can be reached with the mask, is significantly lower and does not exceed 750 °C. For the temperature control during the epitaxial growth, the *type C* TC, which is located behind the manipulator heater, is used. The *growth chamber* is also equipped with a PYRO. The

PYRO is mounted on one of the *growth chamber* ports in the lower part of the chamber and points directly towards the substrate holder. PYRO can be used to measure a precise temperature of the substrate surface above 400 °C[89]. Combining PYRO and TC reading one can achieve well-controlled and highly reproducible growth conditions. The substrate temperatures below 400 °C can not be measured with the PYRO of the type used in our experiments. For all growth procedures where the deposition is performed under 400 °C, the real substrate temperature measurement becomes complicated. Thus, the real substrate temperature in such case is reads out from the TC reading.

The substrate manipulator allows a linear motion as well as a rotational motion of the wafer during epitaxial growth. The standard sample position is 0 mm. The rotation can be applied during the epitaxial growth procedure to achieve the deposition homogeneity. Due to the customized construction of the substrate and mask plates, the sample rotation was not used as well as the sample position was changed to 5 mm in all growth procedures employing shadow mask approach, respectively.

A total of 13 material sources<sup>2</sup> allow the generation of molecular beams: Al, Ga and In effusion cells with different capacities and positions in the *growth chamber*, sublimation sources of Si and C and two cracker sources for As and Sb. By adjusting the cracker heater temperature the beam of  $As_2$  or  $As_4$  as well as  $Sb_n$  or  $Sb_2$  can be generated on demand. The effusion cells used in this thesis are shown in Figure 3.2 (b) as marked in blue boxes. Every effusion source has an individual fast-acting mechanical shutter [ $<0.2$  s], which blocks molecular beams on demand. Besides, all shutters, as well as material source temperatures and valves, are remotely controlled by a computer. This allows for an automatic operation of material sources and

---

<sup>2</sup>15 cell slots are available in the system so that two are still free

the substrate shutter. Thus, the growth recipes can be written before the growth procedure[90]. The specially constructed Ga effusion cluster cell is used for nearly perpendicular deposition of Ga through the shadow mask[91]. The control of the molecular fluxes, as well as the deposition rates and a film growth process, is realized using BFM and RHEED, respectively.

After the growth procedure samples are inspected and analyzed using both: atomic force microscopy (AFM) and scanning electron microscopy (SEM) techniques depending on the aim of the research. In the following sections, the main working principles of AFM and SEM devices are discussed.

## 3.2 Atomic Force Microscopy

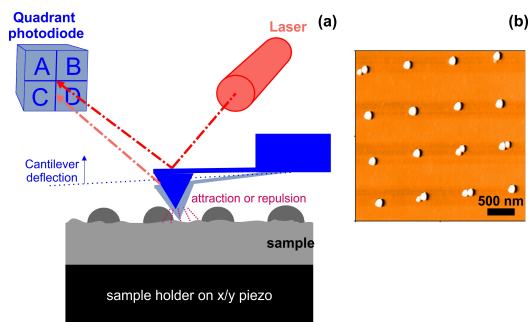


Figure 3.4: Working principle of AFM (a). AFM image of an array Ga droplets (b) deposited through the mask *M15-2* with  $0,23 \mu\text{m}$  openings.

AFM is a type of the scanning probe microscopy that is used to map the topography and to study the properties of the material on a nanoscale[92]. The schematic diagram shown in Figure 3.4 (a) represents an AFM working principle.

At the core of the AFM device is a sharp probe mounted near to the end of the flexible micro-cantilever arm. When the probe comes very close to the sample surface, attractive and repulsive forces, due to the interactions between the tip and the surface, cause a negative or positive bending of the cantilever. The bending is detected by a laser beam, which is well-focused on the backside of the cantilever. The laser beam can be

then reflected back to a 4-quadrant position-sensitive photodiode detector so that the bending of the cantilever can be measured with high accuracy. In other words, the cantilever deflects according to the atomic force variations between the tip and the surface of the sample and, thereby, the detector measures this deflection[93]. The created image reproduces a topographical illustration of the sample surface, e. g., see in Figure 3.4 (b).

The AFM device operates in two general modes: the *static mode* **i**, called a contact mode, and the *dynamic mode* **ii**: the non-contact mode and the tapping mode. In each of these cases, there are dominant interaction forces. The repulsive forces are seen in the contact mode. As an opposite, in the non-contact mode, the attractive forces are observed. In case of the tapping mode at high frequencies, both the repulsive and the attractive forces are seen[94].

The contact mode itself is the simplest AFM mode and was originally used to scan surfaces in early AFM instruments[93]. There are two variations of this mode: a constant force or a variable force[94]. Due to the material properties of the grown samples and a simplicity of the operation, the contact mode with a constant force was only used.

A *Nanosurf Mobile S AFM* was used in this thesis and its technical details are following:

1. AFM probes *PPP – CONTR* from *NANOSENSORS* with highly doped, pyramidal silicon tips [tip radius is 7 nm ], 30 nm thick aluminum reflection coating on the detector side and a low spring constant of  $0.2 \text{ N m}^{-1}$  were employed[95].
2. The measurements were performed at a constant force of 18 nN and without a tip voltage.
3. The standard image resolutions were  $256 \times 256$  or  $512 \times 512$  pixel.

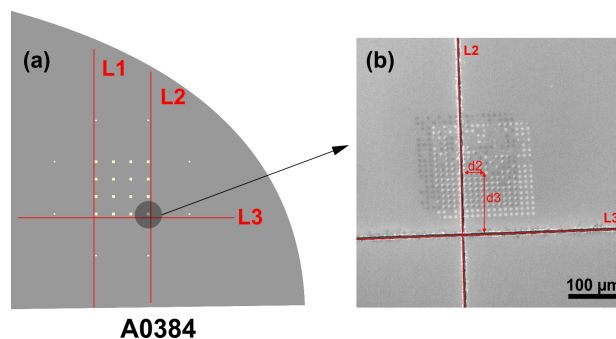


Figure 3.5: An example of the surface map of sample A0384. The scratches L1, L2 and L3 pass through alignment markers along the whole sample (a). Distances  $d_1$ ,  $d_2$  and  $d_3$  are measured by SEM (see SEM image of a single active window (b)). As a result, grown structures can be easily found and characterized by AFM knowing the distances between the active areas embedded in the mask design as well as recently measured distances  $d_1$ ,  $d_2$  and  $d_3$ , respectively.

4. The scan areas were varied from  $3 \mu m \times 3 \mu m$  up to  $9.8 \mu m \times 9.8 \mu m$ .
5. The measurement time per every scanned line was set to 1 s, so every scan took at least 4.5 min if the resolution was  $256 \times 256$ .

The map of the sample surface has to be created before the start of each measurement, where the sample was grown employing the shadow mask approach. Using the grown on the sample surface alignment markers as reference points, long straight lines along the sample surface were drawn using the *Micro Diamond Scriber MR200* from *OEG GmbH*. Distances between lines and centers of the active windows were measured using SEM to ensure accuracy of the following AFM search. As summary, an example of the map is presented in Figure 3.5.

Due to the presence of some disadvantages, such as a possibility of image artifacts and limitations of the scan parameters: a scan area can not be larger

then  $10\ \mu\text{m} \times 10\ \mu\text{m}$  and limited values of the scanning speed, the SEM was used more frequently for fast sample analysis. This, in turn, results in using AFM only for the structural analysis, e. g., for measurements of droplet sizes and heights.

### 3.3 Scanning Electron Microscopy

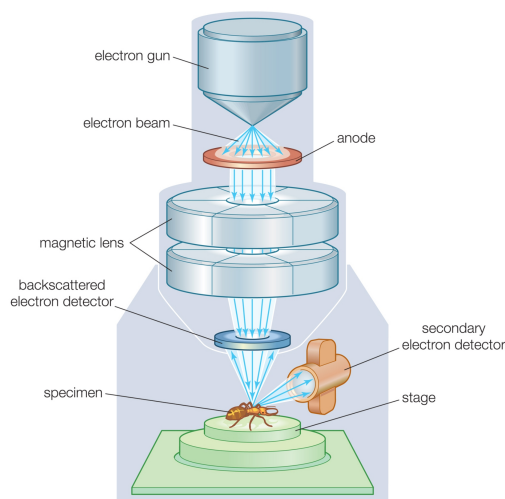


Figure 3.6: Schematic of SEM. High-energy electrons are emitted at the gun and focused by two-stage lenses on the sample, after *Encyclopaedia Britannica, Inc.* 2012

the shadow mask during its fabrication and an imaging of the grown through the shadow mask samples. The typical parameters for the patterning procedure are described in detail in Section 4.2.

SEM is one of the most frequently used instruments for an examination and an analysis of the microstructure morphology[96]. The modern SEM devices provide image resolutions typically lying in the range between 1 nm and 10 nm[97]. Since the most structures in this thesis are nanometer-sized grown on a large area [ $>10\ \mu\text{m} \times 10\ \mu\text{m}$ ], the SEM is best suited for the sample analysis.

The *RAITH150 – TWO* system is used in this work[98]. This combines both a professional EBL and an analytical SEM into a single complete system. This is used in this thesis for both purposes: a patterning of

Figure 3.6 shows a column structure of a conventional SEM. In a standard SEM system, a focused electron beam (EB) is deflected by electric fields to scan over the sample surface point-by-point<sup>3</sup>. The EB is shaped by a system of electromagnetic lenses: condenser and objective lenses. The EB is converged and collimated into a relatively parallel stream with help of the condenser lens. Thereafter, objective lenses are used to focus the EB on the sample surface and to supply further demagnification. An appropriate choice of a lens demagnification and an aperture size results in a reduction of the EB diameter, called a spot size, and enhances the image resolution<sup>4</sup>[99]. The observed image is a result of the interaction between the incident EB and the sample surface. The secondary electrons (SE), backscattered electrons (BSE) and X-ray photons are produced during hitting the sample surface with the EB. Generally, the BSEs penetrate deeper inside the sample and carry information about the material itself, whereas the SEs provide topographical information due to emerging from the first few nanometers of the surface[100].

Since one of objectives of this thesis is a visualization of grown structures, mostly SE images were collected. For that, an *Inlens* detector was used. An acceleration voltage (EHT) and a working distance (WD) were 5 kV and 10 mm, respectively. Parameters for the patterning procedure are discussed in the following Section 4.2.

---

<sup>3</sup>integrated laser interferometer controlled stage provides placement accuracies in the nm regime

<sup>4</sup>a fine EB is strongly required for the both patterning and imaging processes

## Chapter 4

# Fabrication of Si/Si<sub>3</sub>N<sub>4</sub>-mask

This chapter gives a detailed information on the fabrication procedure of robust shadow masks on a Si/Si<sub>3</sub>N<sub>4</sub>-basis. Technical aspects of a mask construction are discussed in the beginning. In the coming Section 4.2, the intricacies, as well as the mask manufacturing process tricks, are described.

The compatibility of shadow masks and the MBE system during a multi-step growth procedure is proven. The results of compatibility tests are presented in Section 4.3. The way to control the substrate temperature during the deposition through the shadow mask is found. Besides, a new approach of *in-situ* aperture size reduction is developed and described in Section 4.3.2.

### 4.1 Main description. Technical aspects

The mask design is dictated by the construction of the mask plate, often called a mask holder, in particular and the MBE system in general. The major technical aspects of a mask fabrication are discussed in this chapter.

First of all, the mask should not contaminate the wafer during epitaxial growth. The contamination deteriorates the quality of the grown structures



tremendously [23], [101]. Thus, GaAs- or *Si*-based materials have to be used for the mask fabrication. On one hand, GaAs seems to be a more evident choice for the growth of GaAs-based structures. On the other hand, *Si* is a low-cost material with maturer microfabrication technology [102]. In addition, *Si* has a low vapor pressure at the temperatures, which are characteristic for GaAs deposition, so it will not affect the growth results [103]. Hereby, temperatures are in a range of 0 and up to 1000 °C.

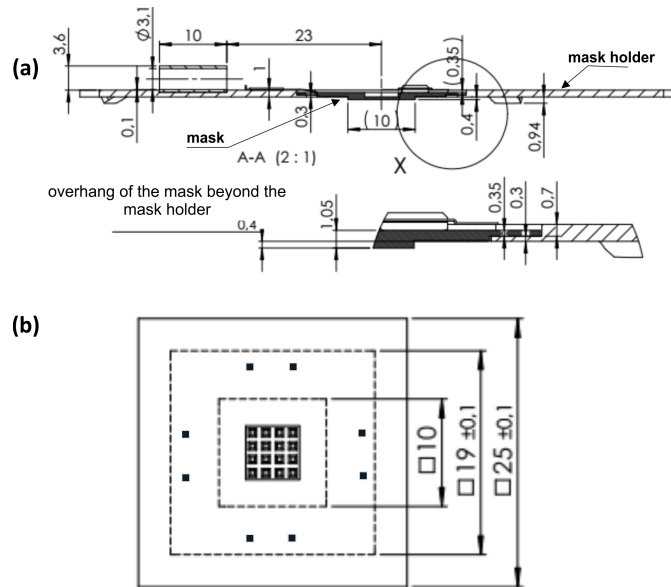


Figure 4.1: Technical drawings of the mask inside the plate (a) and mask itself (b), after [104]. The array of squares in the middle of the shadow mask (b) illustrates an active mask region, **black** squares at the edge are alignment markers. The technical drawings of the mask plate itself can be found in Sections 3.1.1 and 4.3.

Secondly, the technical construction of the mask holder defines some requirements of the mask design (see Figure 4.1). In its turn, this imposes primarily restrictions on the mask size and thickness: the mask has to be rather thick

(1 mm) with the overall mask size is not exceeding  $25\text{ mm} \times 25\text{ mm}$ . Besides, the mask itself should have two main regions: an active region in the middle **i** and a setback at the edge **ii**, which are created with certain purposes. The active region<sup>1</sup> contains the pattern defining the shape of the deposited structures. The size of the full mask including an active region (without a setback) is  $19\text{ mm} \times 19\text{ mm}$  and the setback thickness is 0.7 mm, thereby, it can be mounted into the mask holder, as shown in Figure 4.1 (a). The setback serves two main purposes. On one hand, it is used to mechanically mount the mask. On the other hand, it ensures close contact between the mask and the substrate. Additionally, alignment markers are created on the mask border (see Figure 4.1 (b)). Proper alignment markers allow a further processing of the grown structures (search, analysis and characterization).

A selective deposition will be performed in the sample center through the apertures in the active region, so the overall size of the active region should be rather small ( $5\text{ mm} \times 5\text{ mm}$ ). The thickness of the membrane, which forms the active region, must be rather thin, less than  $1\text{ }\mu\text{m}$  to obtain a good resolution for the apertures. The size of a free-standing membrane has to be limited due to stability reasons. That is why several small active windows were created. Figure 4.2 illustrates the main sketch of the mask.

Taking the aforementioned information into account, *Si* is a very suitable material for the mask fabrication. *Si*-wafer may easily be structured by optical and e-beam lithographies. Even though it is possible to fabricate the mask with desirable dimensions using bare *Si*-wafer, it is almost impossible in practice. The main problem is the aspect ratio of the structure. With the depth of the etching of a 1 mm it is nearly impossible to create an aperture of a few tens or hundreds nm in a well-controlled manner [105]. As an alternative, *Si*-wafers with thin  $SiN_x$  or  $SiO_2$  surface layers may be applied. Such

---

<sup>1</sup>will be used as a stencil for SAE

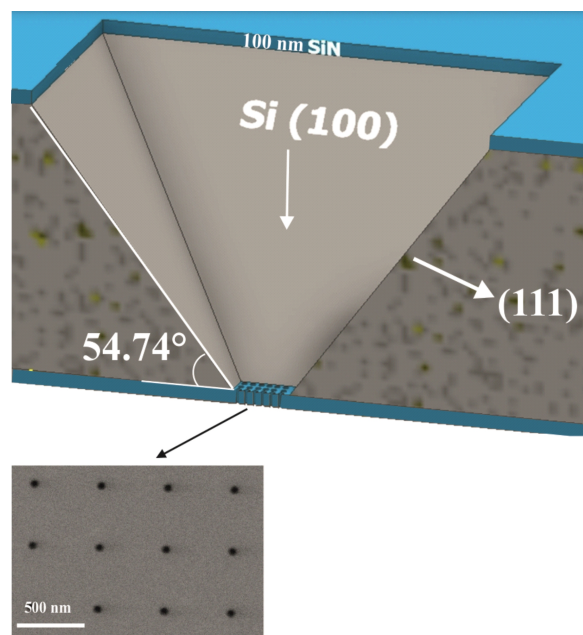


Figure 4.2: The main sketch of the mask, after [108]. The rectangular hole is etched in *Si*-wafer through the whole wafer (gray color) and a holey membrane is made on the *backside* of the wafer (royal blue color). Size of each circular opening is 100 *nm*.

structures are commercially available and may easily be implemented in the lithographic process.  $SiO_2$  is a very attractive candidate for the membrane material due to its chemical properties<sup>2</sup> [106]. The initial studies, unfortunately, have demonstrated, that a thin  $SiO_2$  membrane is not chemically stable enough to withstand 1 mm deep etch of *Si*-wafer [107]. This excludes  $SiO_2$  as a membrane material and proves, that  $SiN_x$ -based processes would have to be implemented.

On top of its chemical stability,  $SiN_x$  is mechanically robust and can withstand temperatures above 1000 °C [109]. The composition affects properties

<sup>2</sup>it may be easily structured in wet-chemical or dry etching processes

and a quality of  $SiN_x$  layers. Low-stress  $Si_3N_4$  is the most thermodynamically stable of the silicon nitrides[110]. It has a high melting point (1900 °C) and a high stability [111]. Due to a low-stress level inside the film, the holey membranes, made on its basis, should withstand an epitaxial growth, e. g., of GaAs, and post-growth cleaning procedures. As mentioned before, apertures in the membrane should be in the same order of a magnitude as a film thickness to avoid clogging of holes and force a single droplet formation within an aperture area. The desired aperture size in the holey array is around 100-200 nm. Such a thin membrane is mechanically very unstable, but it may be processed and applied when deposited on  $Si$ -wafer.

## 4.2 Mask fabrication procedure

The fabrication of the shadow mask is based on a standard  $Si$ -technology.  $Si$  is usually etched by isotropic or anisotropic etching procedures [107]. In isotropic etching, the material is removed uniformly from all directions, i. e., orientation-independent process[112]. The sides of the etch balloon create a concave shape underneath a masking material [113]. This means it has drawbacks in the fabrication of precise structures because of the underetching [114]. In comparison to the isotropic etch, the anisotropic etching removes the material uniformly in a vertical direction [115]. As a result, it is a better-controlled within vertical walls etching procedure and, as a consequence, fewer masks undercut.

Anisotropic etching of  $Si$  is usually achieved with potassium hydroxide (KOH). It is a widely available, reliable method with a good control of the etching conditions[116]. Since this technology is a wet etching process, the equipment is simple, low cost and easy to implement (a hot plate and a stir) [117].

The etching rate of KOH in a single-crystalline  $Si$  depends on the crystalline

orientation[116]. The  $\{111\}$  plane of the  $Si$  crystal has two orders of magnitude slower etch rate than the  $\{100\}$  plane, so single-crystalline structures etched in KOH are defined by the  $\{111\}$  plane[118]. Thus, etching of  $Si$  (100) through a rectangular hole in a masking material creates a pit with flat sloping  $\{111\}$ -oriented sidewalls and a flat  $\{100\}$ -oriented bottom (see Figure 4.2). The  $\{111\}$ -oriented sidewalls have an angle to the surface of the wafer of  $54.74^\circ$  [116], [117]. Such inclination to the surface excludes clogging of the hole in  $Si$ -wafer during deposition through the mask procedures, even after many growth runs it should not affect significantly.

Masks are manufactured from double-side polished 1 mm thick  $Si$  (100)-wafers covered with 100 nm of  $Si_3N_4$  on both sides. 3 inch  $Si$ -wafers are produced by *CrysTec GmbH* (see details in **Appendix A**). Wafers are diced into pieces, so that the size of each piece is  $24\text{ mm} \times 24\text{ mm}$ . Besides, each piece is covered by a thick photoresist layer to protect the materials from the dirt and damages.

$Si_3N_4$  layer on the *front side*<sup>3</sup> of  $Si$ -wafer serves as a hard mask for a wet chemical etching of  $Si$ . Since  $Si_3N_4$  has a negligibly low etching rate in KOH, it is also a good etch stop[119]. In addition, it works as a thin, stable, uniform patterned membrane for the SAE procedure on the *backside*<sup>4</sup> of the  $Si$ -wafer. The fabrication procedure consists of many different steps. The process flow is described below in detail and depicted in Figure 4.3:

1. *Preparation of the wafer*: First of all, a thick photoresist layer was removed by a subsequent rinse in acetone and isopropyl alcohol (isopropanol) for 1 min each chemical. Acetone dissolves photoresist and isopropanol removes acetone residues making the surface clean and

---

<sup>3</sup>a directed to the effusion cells side

<sup>4</sup>a touching substrate side

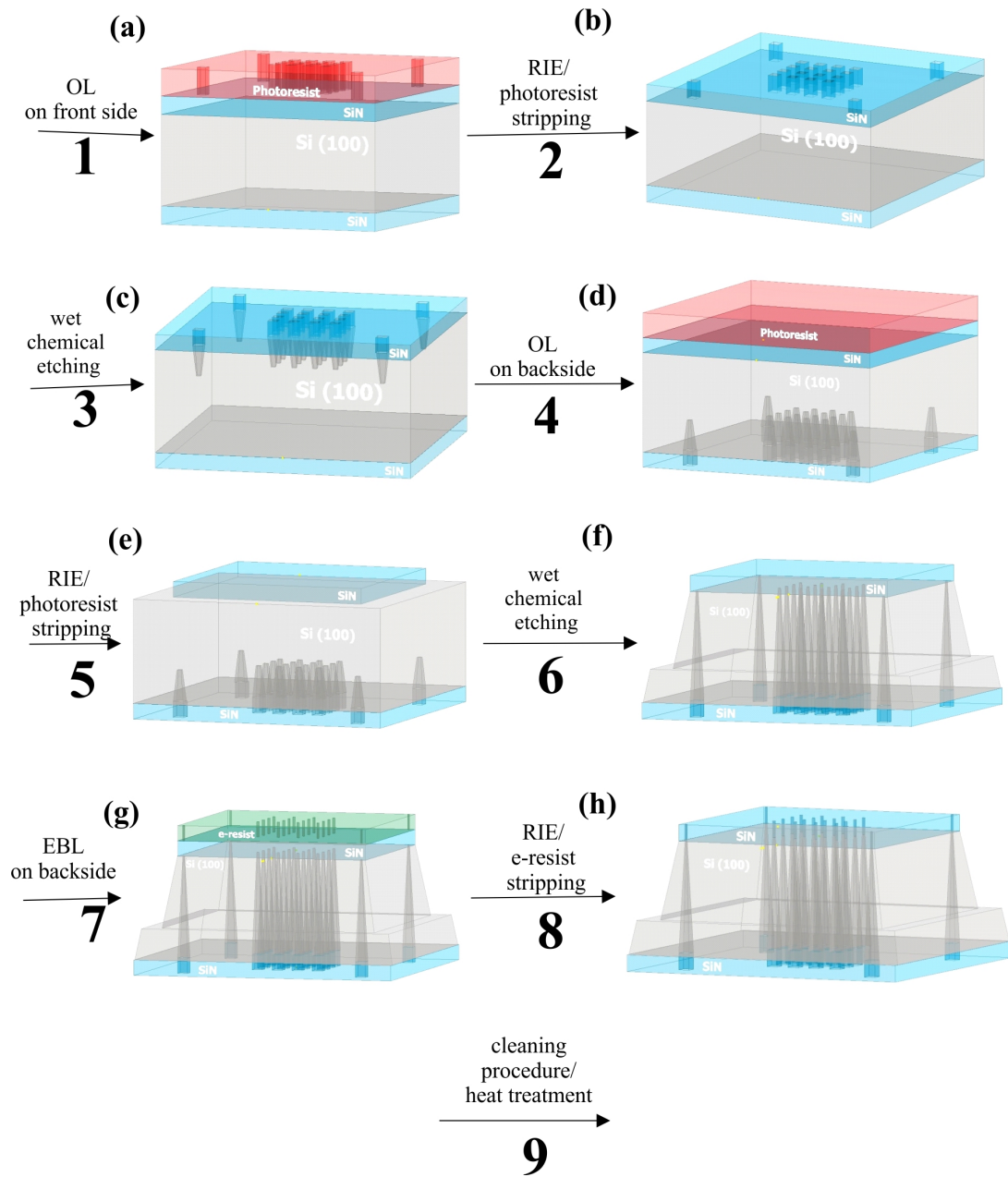


Figure 4.3: The mask fabrication process. The procedure is discussed step by step (from 1 to 9).

ready for the next step. As follows, the wafer was dried by nitrogen ( $N_2$ -gas).

2. The first step of *Optical Lithography (OL)* on its *front side* (see Figure 4.3 (a)) opens the mask fabrication process. For this, the *Si*-wafer was spin-coated [1200 rpm, 30 s] with a 1  $\mu\text{m}$  thick positive tone optical photoresist layer. Diluted in proportion (1:1) AR-P 3510 was used as a photoresist<sup>5</sup>[120]. This was followed by baking on a hot plate for 1 min at 100 °C. The direct transfer of the pattern to *Si*-wafer was realized by a contact photolithography employing an UV-light. The standard expose procedure took 70 s. After the expose, the resist was developed using the matching developer<sup>6</sup>. The development itself took 15 s. A subsequent rinse [30 s] with DI-water was applied to stop the development process. After this patterned wafers were dried by  $N_2$ -gas. As a result, 16 and 8 square openings in the center (active region) and at the edge of the sample (alignment markers) were defined on the *front side* of the wafer, respectively.
3. The  $Si_3N_4$  layer 100 nm thick was removed by *reactive ion etching (RIE)* in defined in previous step square openings employing  $CHF_3$  [16 sccm] and  $O_2$  [1 sccm] gases for approximately 25 min. The pressure in the chamber was kept 10 mTorr, radio frequency (RF) power and inductive coupled plasma (ICP) parameters were 13 W and 0, respectively. As next, the photoresist was removed after the RIE etching procedure (Figure 4.3 (b)). The mask was designed as follows: square-shaped openings in the  $Si_3N_4$  layer have sizes of  $1550 \times 1550 \mu\text{m}^2$  for the windows in the active region and  $1450 \times 1450 \mu\text{m}^2$  for the alignment markers. This will, taking a total thickness of the *Si*-wafer

---

<sup>5</sup>AR 300-12 is a diluent for AR-P 3510

<sup>6</sup>a mixture of AR 300-26 and de-ionized water (DI-water) (1:3) was used as a developer

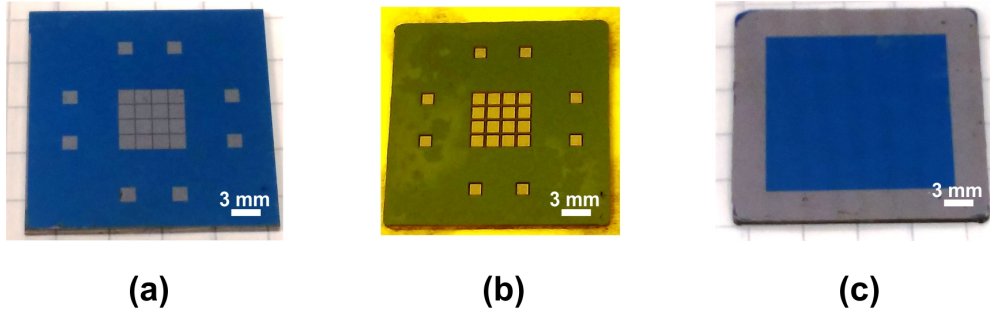


Figure 4.4: Photos of  $Si/Si_3N_4$ -mask after applying following steps: (a) OL and RIE on *front side* of  $Si$ -wafer, (b) OL, RIE and KOH on the *front side*, (c) OL and RIE on the *backside*. The shiny gray areas are areas of bare  $Si$  surface, the royal blue color corresponds to  $Si_3N_4$  layer.

and the angle of the side facets into account, result in nominally  $200 \times 200 \mu\text{m}^2$  (active region) and  $100 \times 100 \mu\text{m}^2$  (alignment markers) free-standing  $Si_3N_4$  membranes, if the etch depth exactly matches the  $Si$ -wafer thickness[108]. Figure 4.4 (a) illustrates the current mask status.

4. *The first step of Si etching*: Wet chemical anisotropic etching of  $Si$  was applied in the following step (Figure 4.3 (c)). The patterned  $Si_3N_4$  layer served here as a hard mask, so that  $Si$  was only removed in opened by previous steps areas. The  $Si$ -wafer was etched  $300 \mu\text{m}$  deep employing a 30 % aqueous KOH-solution<sup>7</sup> at  $100 \text{ }^\circ\text{C}$ . If a set of 3 or 4 patterned wafers should be simultaneously etched, an amount of the solution must be then doubled. Under these conditions, the KOH-etching of the  $300 \mu\text{m}$  typically took 150 min, resulting in an etch rate of  $2 \mu\text{m}/\text{min}$ . After the etching, the processed  $Si$ -wafer was rinsed with DI-water and carefully dried by the  $N_2$ -gas. The result of

<sup>7</sup>34.5 gramms of KOH pellets were dissolved in 100 ml of DI-wafer to achieve 30 % aqueous KOH solution. The nominal KOH concentration in pellets is 85 %



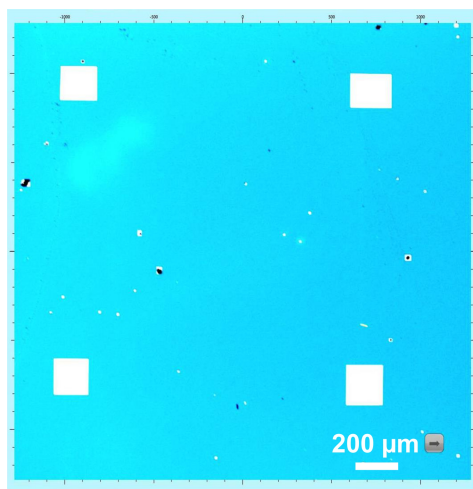


Figure 4.5: Laser microscope image of four free-standing  $Si_3N_4$  membranes within the active region. The royal blue and gold colors correspond to  $Si_3N_4$  layer and free-standing  $Si_3N_4$  membranes, respectively

this step is shown in Figure 4.4 (b). The mathematical representation of the etching a rectangular hole in  $Si$  (100) employing aqueous KOH solution is described in **Appendix B**.

5. *Setback creation*: First of all, the  $Si$ -wafer was turned upside down, so now the following steps were performed on its *backside*. The  $Si_3N_4$  layer was removed by the same combination of OL (Figure 4.3 (d)) and RIE (Figure 4.3 (e)) on a circumferential stripe at the edge. The circumferential stripe is approx. 3 mm wide. This was followed by a photoresist strip step. The result of these manipulations is shown in Figure 4.4 (c).
6. *Membranes fabrication* was followed by a second KOH etching step. Here, the etch depth was 700  $\mu m$ , the etching was performed simultaneously from both sides. The etching procedure took approx. 350 min. This resulted in free-standing  $Si_3N_4$  membranes in the windows

within the active region and for the alignment markers. At the edge of the mask, it generated a  $700\ \mu\text{m}$  setback<sup>8</sup> (see Figure 4.3 (f)). Due to the selectivity of the etch solution, an over-etching will not harm the membrane but only enlarge the free-standing area[109], [118]. By stirring and controlling the temperature of the etchant carefully, reproducible membranes with sizes from  $200 \times 200$  to  $250 \times 250\ \mu\text{m}^2$  were obtained[108]. The part of  $\text{Si}_3\text{N}_4$  membrane array can be seen in Figure 4.5.

7. *Patterning of the membranes:* As the last step, EBL and RIE were used to define patterns on the membranes within the active region (Figures 4.3 (g) and (h)). Hereby, this was realized on *backside* of the wafer. PMMA 950 k was employed as an e-resist and its thickness was approx. 150 nm at the following spin coating parameters: 1200 rpm, 30 s[121]. The fresh PMMA layer was then baked out at  $150\ ^\circ\text{C}$  on a hot plate for 80 s. The spin coating became tricky because of free-standing  $\text{Si}_3\text{N}_4$  membranes in the middle part of the sample, so a vacuum mounting point had to be slightly shifted to the side, where no free-standing membranes are. This would vary the thickness of the PMMA layer over the sample but not tremendously. The expose parameters were as follows: EHT - 20 keV, WD - 10.19 mm, an aperture -  $15\ \mu\text{m}$ , a current (I) - 66.56 pA and the expose time - 1 h 10 min. These can be slightly varied from one patterning procedure to another. As mentioned in Section 3.3, the proper adjustment and focusing of EBL system play a critical role in defining the size and shape of the EB spot. The smaller the spot size the finer the structure size is after

---

<sup>8</sup>the setback thickness **S** (see Figure 4.8) determines the position of the mask in the mask holder. At the same time, it defines the gap between the mask and the substrate, so that the larger the setback **S** the wider the mask sticks out of the mask holder and the smaller is the gap, respectively[108].

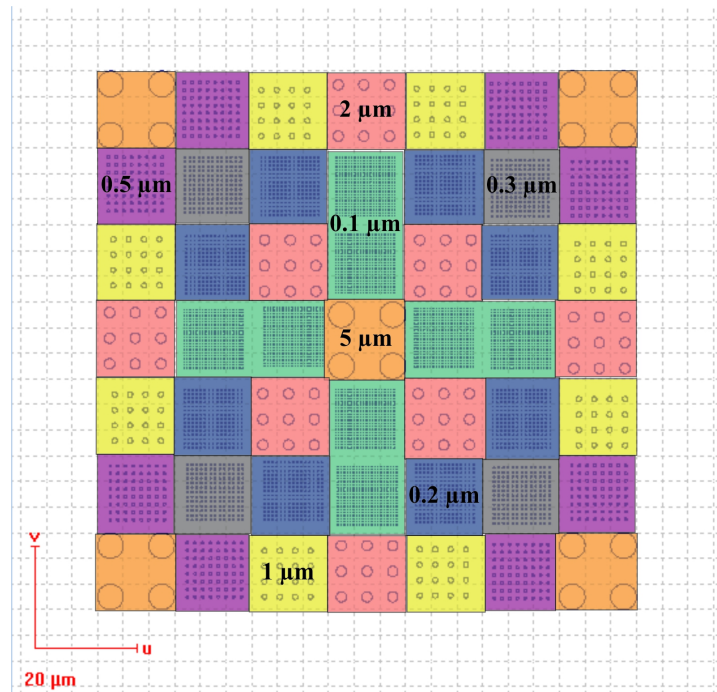


Figure 4.6: A single active window is divided into areas with different hole sizes highlighted in different colors: orange for a  $5 \mu\text{m}$  hole opening with a pitch  $10 \mu\text{m}$  ( $5 \mu\text{m}/10 \mu\text{m}$ ), pink for  $2 \mu\text{m}/5 \mu\text{m}$ , yellow for  $1 \mu\text{m}/3 \mu\text{m}$ , purple for  $0.5 \mu\text{m}/1.5 \mu\text{m}$ , gray for  $0.3 \mu\text{m}/0.9 \mu\text{m}$ , blue for  $0.2 \mu\text{m}/0.8 \mu\text{m}$  and light green for  $0.1 \mu\text{m}/0.6 \mu\text{m}$ , respectively.

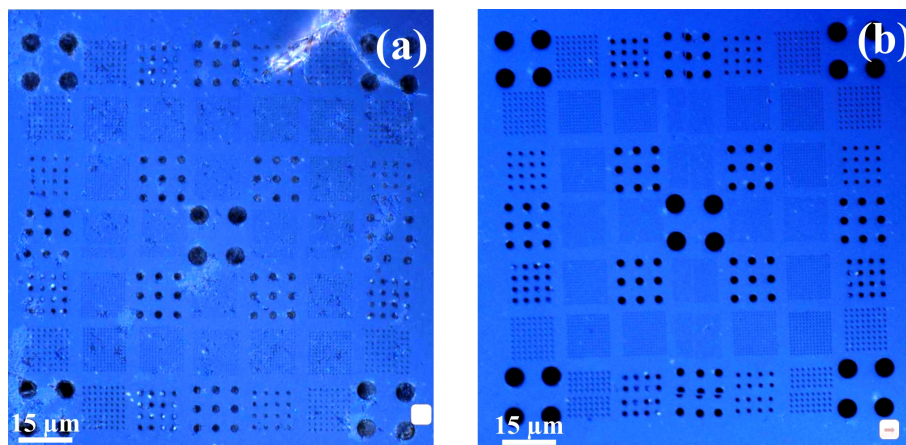


Figure 4.7: Laser microscope image of the single  $Si_3N_4$  membrane before (a) and after (b) the cleaning procedure.

the expose process. The development was performed by AR 600-70 for 30 s plus 30 s rinse with isopropanol<sup>9</sup>. The very gentle drying by  $N_2$ -gas was applied afterward. The RIE parameters were the same as for the two previous RIE steps. Apertures in  $Si_3N_4$  membranes have different diameters: from 5  $\mu m$  down to 100 nm with pitches between 10  $\mu m$  down to 600 nm. The actual single-window design is depicted in Figure 4.6. After this step processed  $Si$ -wafers were named as  $Si/Si_3N_4$ -masks.

8. *Cleaning procedure*: In a final step, masks were cleaned thoroughly to prepare them for an introduction into the MBE system. Concentrated sulfuric acid (96%) was applied for approx. 5 min to remove process residues from the mask surface. Then, masks were rinsed with DI-water and gently dried. Finally, they were heated for 24 h at 200 °C to remove volatile adsorbents and dry them thoroughly. The difference in the surface cleanliness before and after the cleaning procedure is shown

---

<sup>9</sup>it is used here as a stopper

in Figure 4.7.

The whole mask 3D-view can be seen below in Figure 4.8.

### 4.3 Compatibility with UHV system

A freshly cleaned  $Si/Si_3N_4$ -mask was mounted into the mask holder (see Figure 4.9) and introduced to the MBE system.

After a loading of the mask to the *load lock*, this chamber was pumped down to  $5 \times 10^{-8}$  mbar and baked for 8 h at 120 °C. This is a standard loading procedure for all substrates. The  $Si/Si_3N_4$ -mask showed outgassing behavior similar to GaAs or  $Si$  substrates. Thus, it can be further transferred to the next chamber of the MBE system.

Hereafter, the mask was transferred to the HS in the *preparation chamber*<sup>10</sup>, where it was annealed at 550 °C for 1 h. The temperature ramping rate was set to 10 K/min and the pressure inside the *preparation chamber* did not exceed  $4 \times 10^{-8}$  mbar during the outgassing procedure. The temperature control was performed by TC. The whole outgassing procedure took around 2 h. Higher ramping rates could induce an additional stress during heating and cooling steps into thin holey free-standing  $Si_3N_4$  membranes, causing its breaking, so higher ramping rates were not applied.

After the degassing, the mask was taken out of the MBE system and inspected by SEM. SEM images showed that all membranes within the active region have remained intact as well as aperture sizes remained unchanged after this thermal treatment.

As a next step, the same sequence of the above-described steps was repeated. It showed very similar behavior to those of bare semiconductor substrates, e.

---

<sup>10</sup>its base pressure is  $5 \times 10^{-10}$  mbar

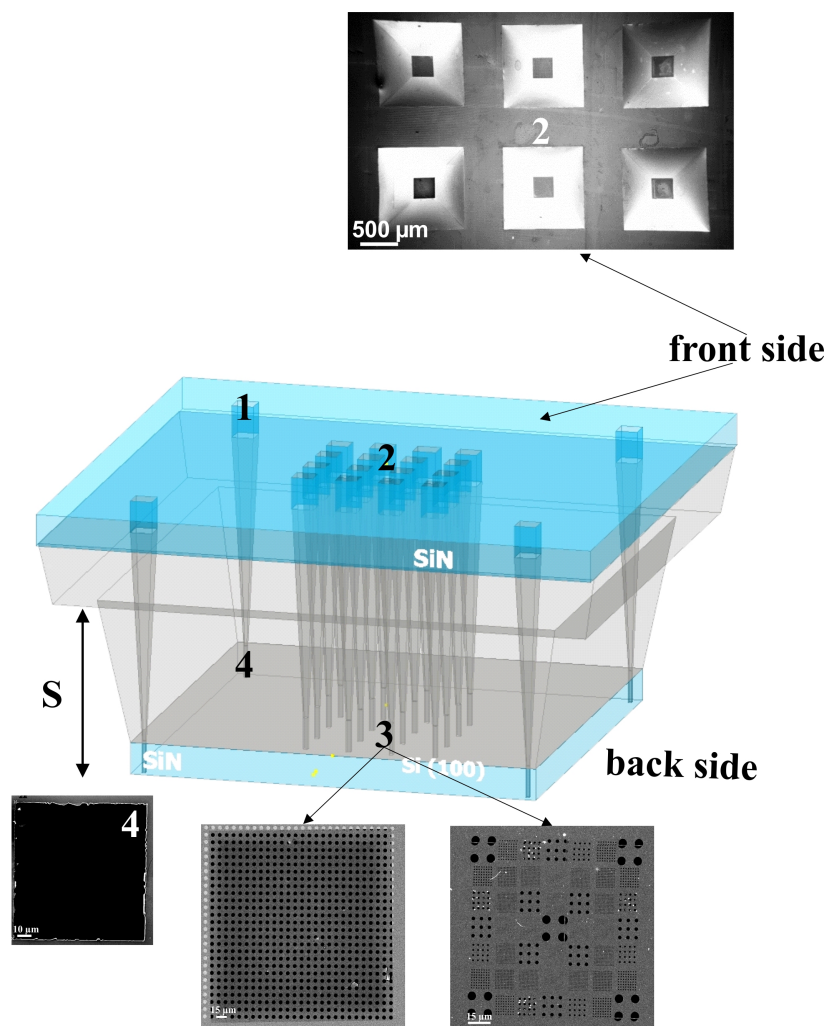


Figure 4.8: The complete mask view. 3D mask sketch is depicted in the middle. The SEM picture **2**, above the 3D mask sketch, shows the *front side* of the shadow mask with pyramidal holes. Free-standing holey  $Si_3N_4$  membranes are depicted below the sketch in SEM images **3**. SEM picture **4** shows an alignment marker.

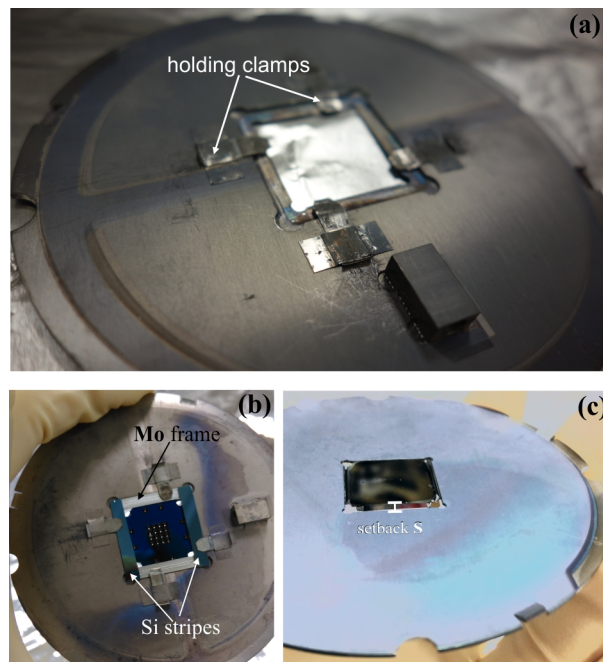


Figure 4.9: Photos of an empty mask holder (a), a holder with mask *front side* view (b) and *backside* view (c). Molybdenum (*Mo*)-frame and *Si*-stripes were used to fix the mask inside the holder and push the setback out to allow a close contact between the mask and GaAs substrate during the deposition through the shadow mask procedure.

g., *GaAs*- or *Si*- wafers. Thus, the conclusion is masks are UHV compatible and there are no reasons against transferring them to the *growth chamber*. Consequently, the mask was introduced to the *growth chamber*, where it was placed 5 mm far away from the tantalum wire heater. The essential requirement of such a distance was already discussed in Section 3.1.1. To test the compatibility of the mask use during the epitaxy procedure, the mask was annealed at 550 °C for 1 h in As atmosphere: the As cracker cell was fully opened<sup>11</sup>. The ramping rate was set to 10 K/min as in previous experiments. The temperature was controlled using both: TC and PYRO. The detailed information regarding the temperature measurement in case of deposition through the mask is given below. The outgassing procedure was controlled *via* quadrupole mass analyzer, so in case of any non-typical behavior the annealing process could be rapidly stopped. The mass spectrum was recorded during the whole outgassing procedure and can be seen in Figure 4.10. The fast check of flux ratios showed no visible differences compared to annealing spectrum of GaAs substrates read out during the deoxidation process. No traces of KOH or sulfuric acid were detected, this means that fabrication and the cleaning of the mask procedures were carried out properly and such a mask will not contaminate the *growth chamber* during its use.

As a summary, fabricated *Si/Si<sub>3</sub>N<sub>4</sub>*-masks are robust, clean and fully compatible with MBE procedure. They can be implemented into the shadow masked SAE.

---

<sup>11</sup>the mechanical As-shutter is opened and the As-valve is 50 % opened



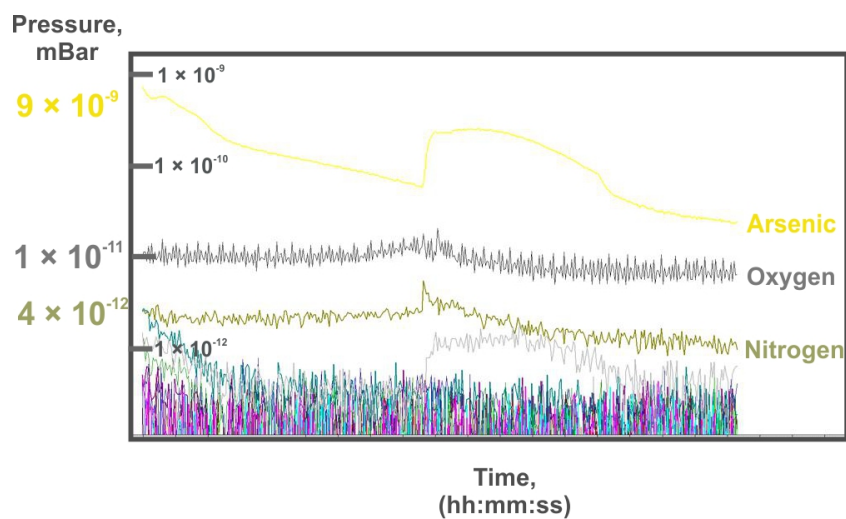


Figure 4.10: The mass spectrum read out during the  $Si/Si_3N_4$ -mask outgassing procedure. The rise in *Arsenic*, *Oxygen* and *Nitrogen* pressures over the time indicates that the outgassing procedure is operating properly: *Arsenic* is present in the chamber due to the opened As cracker cell as well as some amounts of *Nitrogen* and *Oxygen* are usually present in normal MBE usage[122].  $1 \times 10^{-12}$  mbar is used as an indicator of the noise floor.

### 4.3.1 Temperature measurement during shadow masked Selective Area Epitaxy

The common challenge is a definition of the real substrate temperature during MBE procedure. The shadow masked SAE is no an exception to the rule. In epitaxial growth, the most important effect is the change of surface mobility of the adsorbed atoms with the temperature<sup>[123]</sup>. This influences a crystal quality and a defect density of the grown layers tremendously<sup>[124]</sup>. As a result, nearly all properties of the grown structures<sup>12</sup> are strongly influenced by the substrate temperature<sup>[125]-[127]</sup>. Due to TC and PYRO were used as the main approaches for the temperature control in all described in this thesis growth campaigns, further, these will be discussed in detail.

TC is a simple, widely used component that offers a robust temperature measurement over a wide temperature range. Unfortunately, it is often not the first choice because of trade-offs between time and accuracy. In contrast, PYRO is a fast, informative method having better accuracy in the high-temperature range because of its main working principle<sup>13</sup>. It should be noticed here that the substrate must have a sufficient temperature, at least of 400 °C, to obtain a suitable black-body spectrum. Besides, heat radiation reflections from effusion cells located nearby can also put strong influences on the registered spectrum and, as a result, the calculated temperature.

In fact that both approaches have advantages and disadvantages, a proper way of the temperature measurement must be found for each special deposition case. Back to the aim of this thesis, the substrate temperature has to be discussed in terms of the characteristic for shadow masked selective area droplet epitaxy (SADE), i. e., a deposition on substrate **i** or mask **ii**, as well

---

<sup>12</sup>physical, optical and electrical, such as a surface roughness, spectral-luminescence characteristics or a carrier mobility

<sup>13</sup>it detects a black-body radiation emitted from the sample itself

as on substrate through the mask **iii**.

In general, the mask **ii** or the substrate **iii** during deposition through the mask temperature measurements by PYRO become more sophisticated than the bare substrate **i** temperature control. During the epitaxial growth on the mask, the PYRO will not only measure an average mask temperature but a heat radiation from the heater, which is measured through apertures in the mask. The same situation is valid when the substrate temperature has to be controlled during a deposition through the mask procedure, i. e., PYRO measures both: substrate and mask temperatures together. Hence, the PYRO spot has to be well-defined and focused, i. e., it should have the minimal size<sup>14</sup>.

A set of following experiments was performed to estimate a real substrate temperature during an epitaxial growth through the shadow mask:<sup>15</sup>

1. The temperature of GaAs substrate was measured as the most reliable one. During the standart bake-out procedure, desorption of the native oxide layer on top of GaAs substrate takes place[129], [130]. Applying RHEED, the deoxidation temperature can be found with high accuracy<sup>16</sup>[131], [132]. This transition happened at the substrate temperature of  $T_{PYRO}=595\pm 5^{\circ}\text{C}$ . Results of the GaAs substrate temperature ( $T_{sub}$ ) measurement compared to the TC reading are presented in Table 4.1 (*column 2*).
2. Thereafter, substrate temperature measurements in cases of deposition through masks with different sizes of openings were carried out to see

---

<sup>14</sup>1.5 mm

<sup>15</sup>a mask, a substrate or mask-substrate sandwiches were created, as described in the following Section 5.1, and heated in As atmosphere

<sup>16</sup>a transition from an amorphous to an ordered surface can be well-recognized as an abrupt change of the RHEED pattern

an influence of the mask presence on the substrate temperature measurement. For that, different mask-substrate sandwiches were created and the substrate temperature was measured through the mask at the middle part of the sandwich during its heating. Thus, the substrate temperature was measured with respect to an empty mask holder, a mask with  $12 \times 12 \text{ mm}^2$  and with  $4.2 \times 4.2 \text{ mm}^2$  openings, respectively (see *columns 3 – 5* in Table 4.1).

3. Finally, the mask temperature during its heating was controlled (see *column 6* in Table 4.1).

Results presented in Table 4.1 clearly show the influence of the mask presence on the substrate temperature measurement. Besides, due to the impossibility of use a PYRO below  $400 \text{ }^\circ\text{C}$ , the TC was used as a feedback loop. This approach gave a good reproducibility from run-to-run. In other words, the results were always the same if the same  $T_{TC}$  value was set each time. Undoubtedly, the TC reading gives not a real substrate temperature value, so that PYRO was still used for measuring temperatures above  $400 \text{ }^\circ\text{C}$ . Results of depositions obtained in high-temperature range were cross-checked with temperature-dependent changes in surface reconstructions. Finally, the main assumption was based on an extrapolation of the differences between TC and PYRO readings in the high-temperature range. It states that below  $400 \text{ }^\circ\text{C}$  the actual substrate temperature is somewhat higher (30-60 K) than  $T_{TC}$ [133]. Due to such large error, in all further growth campaigns, the  $T_{TC}$  was stated only. The given temperatures were just roughly estimated for special cases of a low-temperature deposition ( $\sim 100^\circ\text{C}$ ) and a deposition through the mask.

These results prove once more limitations of the implementation of the shadow masked SAE into QD formation *via Stranski – Krastanov* growth mode due

Table 4.1: Temperature values for different substrate-mask sandwiches.

$T_{TC}, ^\circ\text{C}$	$T_{PYRO}, ^\circ\text{C}$				
	$T_{sub}$	$T_{sub/maskholder}$	$T_{sub/mask4.2mm}$	$T_{sub/mask12mm}$	$T_{mask}$
350	-	468	432	433	493
360	439	474	438	445	498
370	-	481	442	455	503
380	442	485	448	467	508
390	450	491	451	478	513
400	460	503	456	485	515
410	475	510	463	494	520
420	484	517	471	502	523
430	494	525	477	510	530
440	501	533	481	519	536
450	510	540	485	530	543
460	521	547	491	539	551
470	530	554	498	549	558
480	537	562	506	553	565
490	541	571	510	564	573
500	553	578	517	570	581
510	560	585	524	578	588
520	568	591	531	586	596
530	573	602	537	593	605
540	586	607	544	-	612
550	591	615	550	-	619
560	601	622	557	-	626
570	606	630	561	-	633
580	617	635	569	-	640
590	621	-	574	-	646
600	-	-	582	-	651
610	-	-	590	-	656

to its temperature sensibility and prove consistency of the idea to use DE in its low-temperature regime.

### 4.3.2 *In-situ* aperture size reduction

Before the shadow mask can be used for SADE, the mask has to be covered with a fresh GaAs layer on its *backside*. This thin layer will prepare a clean surface for the following mask-substrate sandwich creation procedure, i. e., for the growth steps carried out in close contact with the substrate. Such layer serves a few purposes: it buries post-processing residues on the mask surface if they still exist **i**, it helps  $Si_3N_4$  membranes to be intact during mask-substrate sandwich creation or separation procedures **ii** and it is a developed technique to reduce *in-situ* aperture sizes **iii**.

The  $Si/Si_3N_4$ -mask was introduced to the *growth chamber* after *in-situ* outgassing procedures listed in Section 4.3. The mask was heated to  $T_{TC}=510$  °C<sup>17</sup> in As atmosphere ( $p_{As} \sim 2 \times 10^{-5}$  mbar)<sup>18</sup>. The temperature ramping rate was kept 10 K/min. 100 nm of GaAs were deposited on the *backside* of the mask employing a growth rate of 0.2 nm/s.

After the deposition, the mask was cooled down, taken out of the MBE system and inspected by laser and scanning electron microscopes. As can be seen in Figure 4.11, the holey membrane has remained intact after the GaAs deposition.

The differences in aperture diameters before and after the deposition were measured by SEM for each aperture size. The results are presented in Table 4.2. *Column* 1 shows a nominal size of the aperture, which is preassigned

---

<sup>17</sup> $T_{Pyro}=588$ °C in Table 4.1

<sup>18</sup>this corresponds to the maximum As pressure, which As cracker source allows for in Paderborn

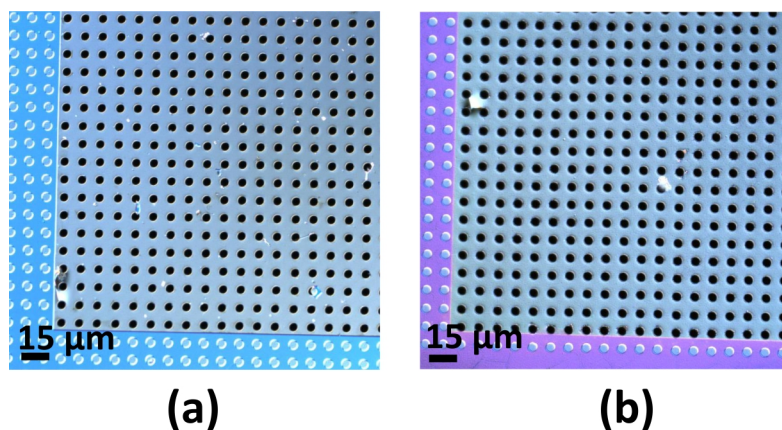


Figure 4.11: Laser microscope images of free-standing holey  $Si_3N_4$  membranes before (a) and after the deposition of GaAs 100 nm (b). The aperture size here is  $5 \mu\text{m}$ .

in the patterning file<sup>19</sup>. *Columns 2 and 3* correspond to measured values of aperture diameters before and after GaAs deposition, respectively. *Columns 4 and 5* represent the differences in aperture diameters before and after the deposition, which are expressed in quantitative and percentage forms.

As can be seen from Table 4.2, for  $5,0 \mu\text{m}$  aperture, the diameter was only slightly reduced to  $4.9 \mu\text{m}$ , which is an opposite to  $0,1 \mu\text{m}$  aperture, where the whole aperture was completely clogged (see Figure 4.12 (b)). This subsequently means different clogging rates for different aperture sizes: the larger the aperture the lower the clogging rate **i** and larger apertures need more material to be clogged **ii**.

After the SEM inspection, the shadow mask was loaded back to the MBE system and the standard degassing procedures were performed. As mentioned above, due to physical and chemical properties of a low-stress  $Si_3N_4$ , it should not be problematic to heat the mask containing  $Si_3N_4$  layers fur-

<sup>19</sup>PIONEER software-file including a pattern for EBL

Table 4.2: The aperture diameters before and after the deposition of 100 nm GaAs, as well as after the re-evaporation procedure.

$\varnothing_{nominal}, \mu\text{m}$	$\varnothing_{before}, \mu\text{m}$	$\varnothing_{after}, \mu\text{m}$	$\Delta, \text{nm}$	%	$\varnothing_{re-evap}, \mu\text{m}$
5,0	5,001	4,921	80	1,60	5,000
2,0	2,939	2,880	59	2,01	2,942
1,0	0,973	0,885	88	9,04	0,980
0,5	0,502	0,399	103	20,52	0,509
0,4	0,425	0,300	125	29,41	0,428
0,2	0,237	0,138	99	41,77	0,229
0,1	0,102	clogged	0	100,00	0,105

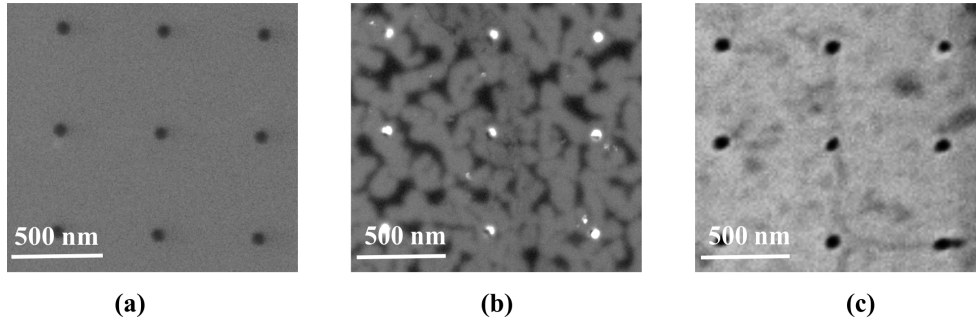


Figure 4.12: SEM images of holey mask with the smallest apertures before (a), after deposition of 100 nm GaAs (b) as well as after re-evaporation procedures (c), after [108].

ther in As absence. This should not harm the thin  $Si_3N_4$  layer, in general, and holey membranes, in particular. At the same moment, such temperature treatment will re-evaporate the deposited GaAs layer from the mask surface, thereby, *in-situ* clean the mask. The standard GaAs re-evaporation process starts already from 620 °C [134].

Therefore, the mask was annealed at  $T_{TC}=750$  °C<sup>20</sup> for 25 min in As-free en-

<sup>20</sup> $T_{PYRO}=820$ °C see in Table 4.1



vironment in the *growth chamber*. This is the maximum temperature, which was tested, corresponding to the maximum temperature substrate heater allows for. The ramping rate was the same as in previous experiments. Afterward, the mask was taken out and again inspected by SEM. After such heat treatment, all membranes have remained intact and the GaAs layer was removed completely without deteriorating the holey pattern, as seen in Figure 4.12 (c). Column 6 in Table 4.2 presents the measured aperture diameters after the re-evaporation process. The aperture diameters were not changed.

The same sequences of steps: *in – situ* mask degassing procedures, a deposition of GaAs on the *backside* of the shadow mask and its subsequent re-evaporation, were performed with different masks to confirm the reported above results. All fabricated masks showed the same behavior. Finally, the mask ability to withstand a multi-step growth procedure was proven. The mask was covered with 50 nm of GaAs and cleaned by a subsequent GaAs re-evaporation step. This cycle was repeated 10 times. After the SEM inspection, neither cracking of the membrane or a deterioration of its holey pattern was found on the shadow mask surface. This clearly shows that the shadow  $Si/Si_3N_4$ -mask can withstand a large number of deposition/re-evaporation cycles.

As a summary, fabricated  $Si/Si_3N_4$ -masks are fully compatible with the III-V MBE process and can withstand the deposition of GaAs layers as well as *in-situ* cleaning procedures. The aperture sizes can be reduced by a deposition of an additional GaAs layer with a certain thickness as well as this layer can be re-evaporated trace-less. This means, the shadow mask can be used repeatedly without any *ex-situ* cleaning steps.

## Chapter 5

# Sample growth and characterization

In the following chapter, after a brief survey of the selective area droplet epitaxy (Section 5.1), the key aspects of the deposition through the shadow mask are discussed (Section 5.2). Section 5.3 gives a complete picture of the droplet formation process.

As a consequence, the main growth parameters are optimized in terms of a site-controlled droplet formation employing shadow masked selective area epitaxy. The need for a deposition of a pre-coverage layer and its effect on a Ga out-diffusion from local deposits are discussed below in Section 5.3.1. The coverage layer and influence of its thickness on droplet sizes, heights and densities concerning aperture sizes are studied in Section 5.3.2. Finally, results of the deposition in a two-step procedure as well as directly at elevated temperatures are described, respectively.

## 5.1 Selective Area Droplet Epitaxy procedure

SADE is a modified positioning technique allowing a local formation of single QNs *via* DE employing shadow masks. The basic principle of the SADE process is schematically shown in Figure 5.1. This approach consists of the following steps:

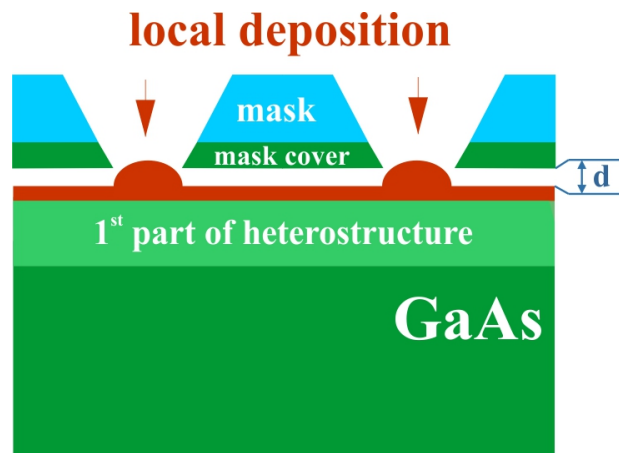


Figure 5.1: Schematics of the shadow masked SAE, after [108]. The distance between the mask and the substrate is  $d$ .

1. Growth of the first part of the semiconductor heterostructure:  $\text{Al}_{0.3}\text{Ga}_{0.7}\text{As}$  layer with a subsequent formation of a Ga-terminated surface by deposition of a certain Ga amount. This is followed by a transfer of the sample out of the *growth chamber* to the *preparation chamber*.
2. Growth of a fresh GaAs mask cover layer, as described in detail in Section 4.3.2, to prepare a clean mask surface before a mask-substrate sandwich formation. A transfer of the mask to the *preparation chamber*.
3. Formation of the mask-substrate sandwich under UHV conditions in the *preparation chamber* with its transfer to the *growth chamber*.

The whole process of the sandwich formation is illustrated in Figure 5.2.

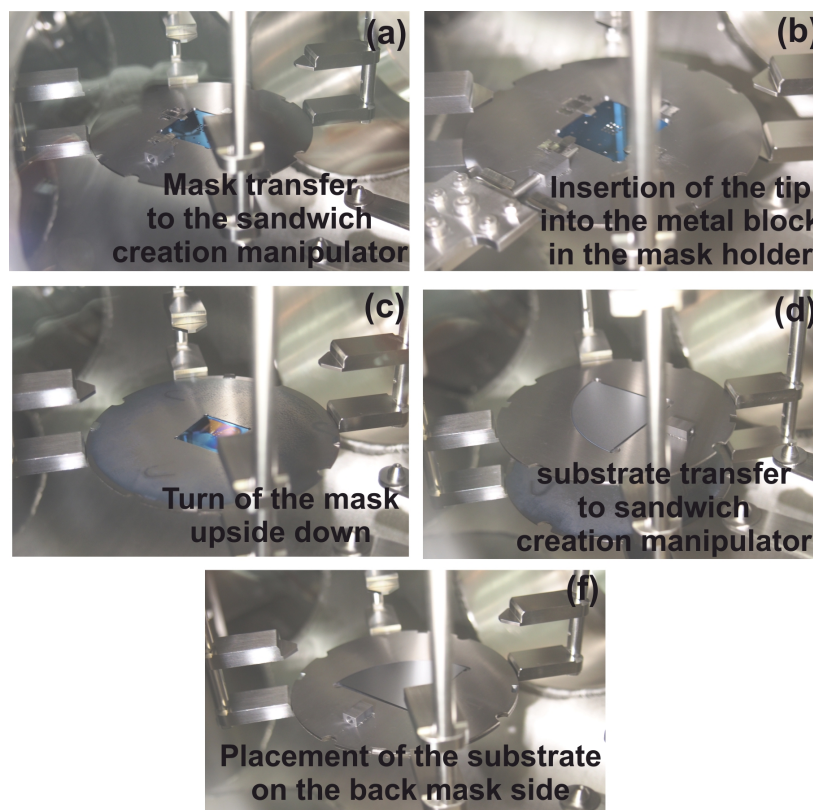


Figure 5.2: Illustration of the mask-substrate sandwich formation process. This is described step by step from (a) to (f).

4. A facultative deposition of alignment markers through opened in shadow mask areas. A deposition occurs only through the outer shadow mask part.<sup>1</sup> Usually, 50–100 nm of GaAs are deposited as alignment markers.

5. In the case of the SADE, the group-III metal, Ga is deposited locally

<sup>1</sup>an active shadow mask region is blocked by a special shutter with a placed in coarse *Mo*-mask (Figure 5.3 (a)), so that no deposition through its center is performed (Figure 5.3 (b))

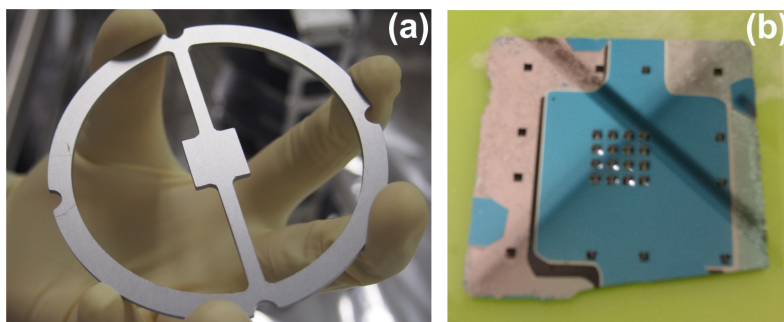


Figure 5.3: The coarse  $Mo$ -mask (a). The *front side* view of the shadow  $Si/Si_3N_4$ -mask after the deposition of alignment markers (b).

within the active  $Si/Si_3N_4$ -mask region resulting in a site-controlled droplet formation. The crystallization step, which transforms metal droplets into semiconductor QNs, can either be performed with the  $Si/Si_3N_4$ -mask in place or after a separation of the mask-substrate sandwich (see step 6). It should be noted here that the As flux, coming to the surface through the tiny holes in the shadow mask, can not be accurately estimated. Thus, for a formation of optically active QNs a crystallization step has to be performed after the sandwich separation to provide a efficient As flux. The deposition procedure is followed by a transfer of the mask-substrate sandwich back to the *preparation chamber*.

6. A separation of the mask-substrate sandwich under UHV in the *preparation chamber* with a subsequent transfer of the sample back to the *growth chamber* for the next growth step.
7. A growth of the second part of the heterostructure: an overgrowth of GaAs QNs with an  $Al_{0.3}Ga_{0.7}As$  layer.

The above-described steps of the SADE procedure were implemented into a growth process in solid-source III-V MBE system located in Paderborn using

*EpiCAD* software[90]. Due to the complication of the deposition procedure employing shadow masked SAE compared to the standard growth procedures, the formation of GaAs QNs in  $\text{Al}_{0.3}\text{Ga}_{0.7}\text{As}$  matrix was performed using a few separated growth recipes. The growth procedure then looks as follows:

1. In the first recipe, a  $\text{Al}_{0.3}\text{Ga}_{0.7}\text{As}$  layer growth and a subsequent Ga-termination of its surface are realized.
2. In the second one, alignment markers, as well as Ga droplets, are deposited locally at defined by shadow  $\text{Si}/\text{Si}_3\text{N}_4$ -mask places. Here the Ga droplet deposition can be performed either directly at elevated temperatures or as a two-step procedure, where Ga is deposited in a low-temperature regime, in the first step, and subsequently annealed, in the second one. In case of a two-step procedure, the annealing step is performed after the separation of the substrate-mask sandwich. Please also note that, the omitted in this thesis, a crystallization step can be performed directly after the local Ga deposition.
3. In the third recipe, the capping of GaAs QNs with a  $\text{Al}_{0.3}\text{Ga}_{0.7}\text{As}$  layer can be realized.

Examples of growth recipes for the test sample A0176 are presented in Figure 5.4. Here, instead of standard  $\text{Al}_{0.3}\text{Ga}_{0.7}\text{As}$  layer deposition, GaAs layer was deposited to test a Ga through the shadow mask deposition procedure. The growth protocol can be found in **Appendix C**.

	Time	Thickness	Sub °C	SUBRot %	2B_Ga1 °C	3VP_As %	15Cl_Ga °C
1	AtRunTime		555.0	0.01	980.0	30.00	1072.0
2	AtRunTime						
3							
4	0:08:24.8	0.1000 $\mu\text{m}$	555.0	0.01	980.0	30.00	1072.0
5	0:00:30.0		555.0	0.01	980.0	30.00	1072.0
6	0:12:30.0		180.0	0.01	980.0	1.00	1072.0
7	0:00:30.0		180.0	0.01	980.0	1.00	1072.0
8	0:00:01.3	0.0003 $\mu\text{m}$	180.0	0.01	980.0	1.00	1072.0
9	0:01:00.0		180.0	0.01	980.0	1.00	1072.0
10	0:00:30.0		180.0	0.01	980.0	1.00	1072.0
11							
End	AtRunTime		180.0	0.01	980.0	1.00	1072.0

	Time	Thickness	Sub °C	SUBRot %	2B_Ga1 °C	3VP_As %	15Cl_Ga °C
1	AtRunTime		260.0	0.01	980.0	30.00	1072.0
2	AtRunTime						
3							
4	0:21:02.0	0.2500 $\mu\text{m}$	260.0	0.01	980.0	30.00	1072.0
5	0:00:30 ++		260.0	0.01	980.0	30.00	1072.0
6	0:08:00.0		180.0	0.01	820.0	1.00	1072.0
7	0:00:30.0		180.0	0.01	820.0	1.00	1072.0
8	0:00:06.3	0.0013 $\mu\text{m}$	180.0	0.01	820.0	1.00	1072.0
9	0:01:00.0		180.0	0.01	800.0	1.00	1052.0
10	0:03:00.0		180.0	0.01	740.0	50.00	992.0
11	0:08:00.0		100.0	0.01	580.0	1.00	832.0
12							
End	AtRunTime		100.0	0.01	580.0	1.00	832.0

Figure 5.4: Examples of growth recipes of sample A0176. In the first recipe, 100 nm of GaAs were deposited with a subsequent Ga-termination of the surface (a). In the second recipe, 250 nm thick GaAs alignment markers were deposited through the outer part of the shadow mask. This was followed by a Ga deposition of 4.5 ML within the active mask region (b).

## 5.2 Key aspects of the deposition through a shadow mask

As mentioned in previous sections, a local Ga deposition is the first stage of a site-controlled QN formation by DE technique. A substrate temperature **i**, a Ga flux **ii** and a total Ga amount **iii**, further coverage, are the key parameters to control Ga droplet densities and sizes[67]. Thus for a special case of a single

droplet formation employing shadow  $Si/Si_3N_4$ -mask<sup>2</sup>, deposition parameters have to be chosen to reach a low droplet density regime. This can be achieved using low substrate temperatures, e. g., below  $T_{TC}=400$  °C, as well as low Ga deposition rates, e. g.,  $0.03 \frac{ML}{s}$ , respectively[67], [135]. Also, the Ga coverage itself has to be discussed concerning opened in the shadow mask areas (sq.  $\mu m$ ) through which Ga is deposited.

According to the standard DE procedure, the first Ga ML is consumed only for the surface termination and the following coverage, typically 2.75 ML, contributes to the Ga droplet formation[136]. This works practically for surface QDs, where Ga deposition performed on the whole substrate surface. Presumably, for the SADE is valid that the larger Ga amounts should be deposited to get Ga droplets having the same heights and diameters as for surface ones. The results of a coverage estimation with respect to aperture sizes are presented below in Table 5.1. The estimation is performed using the following relation:

$$S_{total} = \underbrace{\pi r^2}_{S_{circle}} \cdot N \quad (1)$$

where  $r$  and  $N$  are a radius of a single aperture and number of apertures for every single active window, respectively. Thus, taking the size of the single active window into account, each active window area is  $S_{membrane}=40000 \mu m^2$ . The main assumption here is the total Ga amount will pass completely through  $S_{membrane}$ .

Opened areas ( $S_{area}$ ) (Column 3 in Table 5.1) are calculated considering aperture sizes. The total number of apertures  $N$  is counted on the assumption of the maximum number of apertures having the same size in an array

---

<sup>2</sup>this means a single droplet occupancy within the area limited by the smallest aperture diameter, i. e., 100-200 nm



Table 5.1: An estimated Ga coverage *vs* an aperture size with respect to  $S_{membrane}$

$r, \mu\text{m}$	$N$	$S_{area}, \mu\text{m}^2$	%
2,5	200	3925,3	9,81
1,0	784	2462,0	6,16
0,5	2500	1962,5	4,91
0,25	10000	1962,5	4,91
0,15	27556	1947,0	4,87
0,1	40000	1256,0	3,14
0,05	81225	637,6	1,59

occupying a single active window. The PIONEER-file is used for such a calculation.

Results of a coverage estimation (*Columns* 4 and 5 in Table 5.1) clearly show that the smaller the aperture size the larger the amount of material should be deposited, e. g., if the same coverage thickness is deposited through 5  $\mu\text{m}$  and 100 nm apertures, droplets will be only formed in a 5  $\mu\text{m}$  aperture area. Thus, an appropriate Ga amount has to be found in further studies to allow a single droplet occupancy per the smallest aperture area.

Besides, as any other substrate patterning technique, the deposition employing shadow masks has limitations: the minimal structure dimensions and loss of the resolution. The major limiting effect here is the presence of the mask-substrate gap during the Ga deposition stage. This induces a broadening of the deposited Ga over larger than the aperture size area. Theoretically, the process of Ga deposition through the shadow mask can be discussed concerning geometrical parameters of the MBE system itself.

If Ga atom diffusion can be neglected<sup>3</sup>, the extension of the deposit in case of

<sup>3</sup>in case of epitaxy this means, the Ga deposition is performed at low substrate tem-

a perpendicular deposition is given by geometrical parameters: the diameter of the aperture  $\mathbf{X}$ , a size of the source  $\mathbf{L}$ , a source-substrate distance  $\mathbf{D}$  and a gap between the shadow mask and the substrate  $\mathbf{d}$ [56]. Thus, the diameter of the deposit  $\mathbf{h}$  is then given by the following relation [56]:

$$h = X + L \frac{d}{D} \quad (2)$$

The second summand in Equation (2) describes the penumbra region. The size of this region strongly depends on  $\mathbf{d}$  (see Figures 5.1 and 5.5). The schematic representation of the deposition that occurred through the opening in the shadow mask is presented in Figure 5.5.

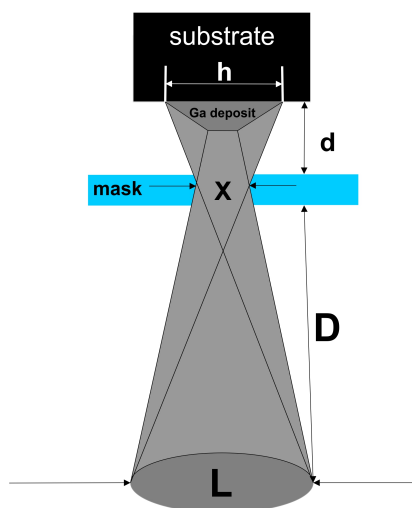


Figure 5.5: The influence of the system geometry on the lateral resolution, after [56]. The best pattern transfer can be achieved only for an incoming Ga flux along the mask normal and with no gap present between the mask and the substrate.

To see practically how the mask-substrate gap influences the lateral resolution of the SADE procedure, the following sequence of experiments was performed, so that Ga atom diffusion is suppressed

carried out using  $Ga_{cluster}$  source for nearly perpendicular deposition[91]. As mentioned in Sections 4.1 and 4.2, the gap  $\mathbf{d}$  can be controlled by a set of a setback thickness  $\mathbf{S}$  (see Figure 4.8). As a result, for Ga test depositions, three shadow  $Si/Si_3N_4$ -masks were fabricated. These have different setback thicknesses  $\mathbf{S}$ : the mask  $M2-1$  has a gap of  $\mathbf{d}=40 \mu\text{m}$  and masks  $M4-2$  and  $M15-2$  are constructed to be in a close contact with the substrate during the deposition through the shadow mask stage, i. e.,  $\mathbf{d}=0 \mu\text{m}$ . Other mask parameters kept identical. Masks  $M2-1$  and  $M4-2$  have active windows with arrays of holes having two aperture sizes:  $5 \mu\text{m}$  and  $100 \text{ nm}$ , respectively. The mask  $M15-2$  has a special design, where different apertures:  $5 \mu\text{m}$ ,  $2 \mu\text{m}$ ,  $1 \mu\text{m}$ ,  $0.6 \mu\text{m}$ ,  $0.34 \mu\text{m}$ ,  $0.23 \mu\text{m}$  and  $0.14 \mu\text{m}$ , were created, as depicted in Figure 4.6.

For each deposition campaign, the growth procedure had the following steps:

1. The mask was introduced into the *growth chamber* and  $100 \text{ nm}$  of GaAs were deposited on its *backside*, as described in Section 4.3.2.
2. Then, the mask was transferred to the *preparation chamber*, where it was placed to the sandwich creation station.
3. At the same time, a GaAs (100) wafer<sup>4</sup> was introduced to the *growth chamber*. After the deoxidation process,  $100 \text{ nm}$  of GaAs were deposited as a buffer layer at standard GaAs growth conditions. Then, the substrate temperature was reduced to  $250 \text{ }^\circ\text{C}$  and  $1 \text{ ML}$  of Ga was deposited in As absence to create a Ga-terminated surface.
4. After this, the substrate was transferred back to the *preparation chamber*, where the mask-substrate sandwich was formed, as described above in Section 5.1 (see Figure 5.2).

---

<sup>4</sup>a quarter of semi-insulating 3 inch GaAs (100) wafer (see details in **Appendix A**)

5. The sandwich was introduced to the *growth chamber* and 4.5 ML of Ga were deposited through the mask at  $T_{sub}$ <sup>5</sup> in As absence. Ga deposition rate was always kept  $0.03 \frac{ML}{s}$ . After 1 min of an interruption, the mask-substrate sandwich was transferred back to the *preparation chamber* and separated under UHV.
6. The substrate was finally taken out from the MBE system and inspected with SEM.

As mentioned above, diffusion of Ga atoms on the substrate surface has to be suppressed during the Ga droplet formation stage. This will be discussed below with respect to the substrate temperature  $T_{sub}$ . The general trend, which should be considered here, is an anisotropy of a Ga diffusion across the GaAs (100) surface[137]. The anisotropic surface diffusion is responsible for the shape and an orientation of oval defects, as well as for the rippled surface structure, observed on  $Al_xGa_{1-x}As$ [138], [139]. Due to the surface anisotropy, Ga atoms diffuse more likely along the [1-10] direction than along the [110] direction[139]. This will definitely influence on results of the deposition through the shadow mask. Thus, it is obligatory to find an appropriate  $T_{sub}$  at which Ga atom diffusion is suppressed and Ga is deposited forming droplets.

For that, 4.5 ML of Ga were deposited through the mask  $M2-1$  at different  $T_{sub}$ : 250, 175 and 100 °C. Results of depositions are presented in Figure 5.6. SEM images clearly show the change of the deposited pattern from rows (A0261) to separated disks (A0267) with a decrease of  $T_{sub}$ . In other words, the higher the substrate temperature the higher the Ga diffusion rate[139]. It seems that at  $T_{sub}=100$  °C the Ga diffusion is fully suppressed. As a result, this substrate temperature was used in a two-step deposition

---

<sup>5</sup>different substrate temperatures were applied further to optimize deposition parameters allowing a single droplet formation

procedures, except those, where the deposition was performed directly at elevated temperatures. It should be noted that the local deposit and aperture sizes are found to be different, so that a broadening of the deposit took place, as can be predicted by relation 2 (see Figure 5.6 A0267).

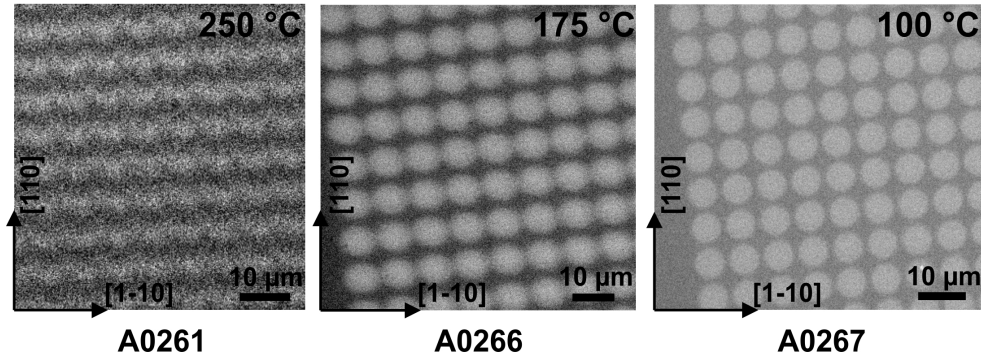


Figure 5.6: Results of 4.5 ML Ga deposition at different  $T_{sub}$  through the 5  $\mu\text{m}$  apertures employing mask  $M2 - 1$ . Growth protocols can be found in **Appendix C**.

Next, Ga deposition was performed through the mask  $M4 - 2$ . Results of the deposition can be seen in Figure 5.7 (b). Besides, SEM images show that deposits differ strongly for depositions through shadow masks  $M2 - 1$  and  $M4 - 2$ . For  $M2 - 1$  with 40  $\mu\text{m}$  gap, local deposits exhibit a diameter of 7.5  $\mu\text{m}$ . This means the diameter was greatly enhanced compared to the 5  $\mu\text{m}$  aperture. Taking relation (2) and inserting values corresponding to the geometry of the MBE system<sup>6</sup>, the calculated diameter of the local deposit matches the experimental observation. For the 100 nm hole, this means the enlargement of the deposited area from 100 nm to 2.5  $\mu\text{m}$ , i. e., Ga sprays over the larger area and, as a result, no single droplet formation occurs.

In the case of the deposition through the mask  $M4 - 2$  with close contact

<sup>6</sup> $L=22$  mm,  $D=364$  mm[91],[141],

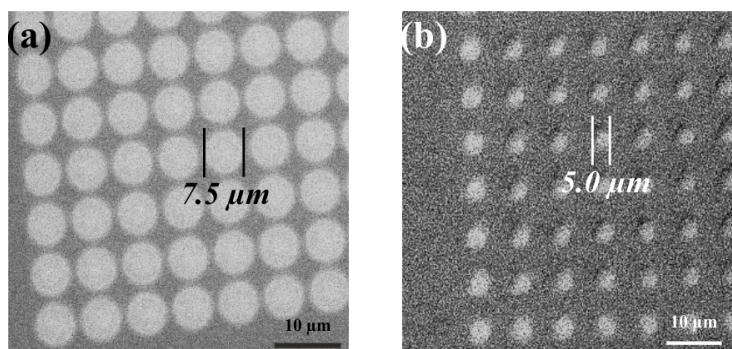


Figure 5.7: Comparison between results of 4.5 ML Ga deposition through the  $5\ \mu\text{m}$  apertures with  $40\ \mu\text{m}$  mask-substrate gap (a) and in close contact (b), after [108].

to the substrate, Ga local deposits reproduce the exact size of the aperture, as it was expected. Thus, close contact is a necessary condition, which provides the best lateral resolution for structures deposited through the shadow  $\text{Si}/\text{Si}_3\text{N}_4$ -mask.

Undoubtedly, close contact might harm the substrate, the mask or even both of them together. Results of Ga test depositions show that shadow masks are robust enough not to be damaged by close contact during mask-substrate sandwich creation or separation, as well as deposition, procedures [108]. Thus, the risk of the mask damage during the deposition, performed in close contact, is for  $\text{Si}_3\text{N}_4/\text{GaAs}$  material system not very high. The substrate surface itself does not suffer severe damage although rarely some scratches were observed at its outer areas, caused by a contact the GaAs wafer with the substrate holder [108].

Employing mask  $M15 - 2$ , a deposition of sub- $\mu\text{m}$  structures was realized. The growth procedure was identical to the aforementioned ones, except just the detail that 50 nm of GaAs were deposited as a mask cover layer on its

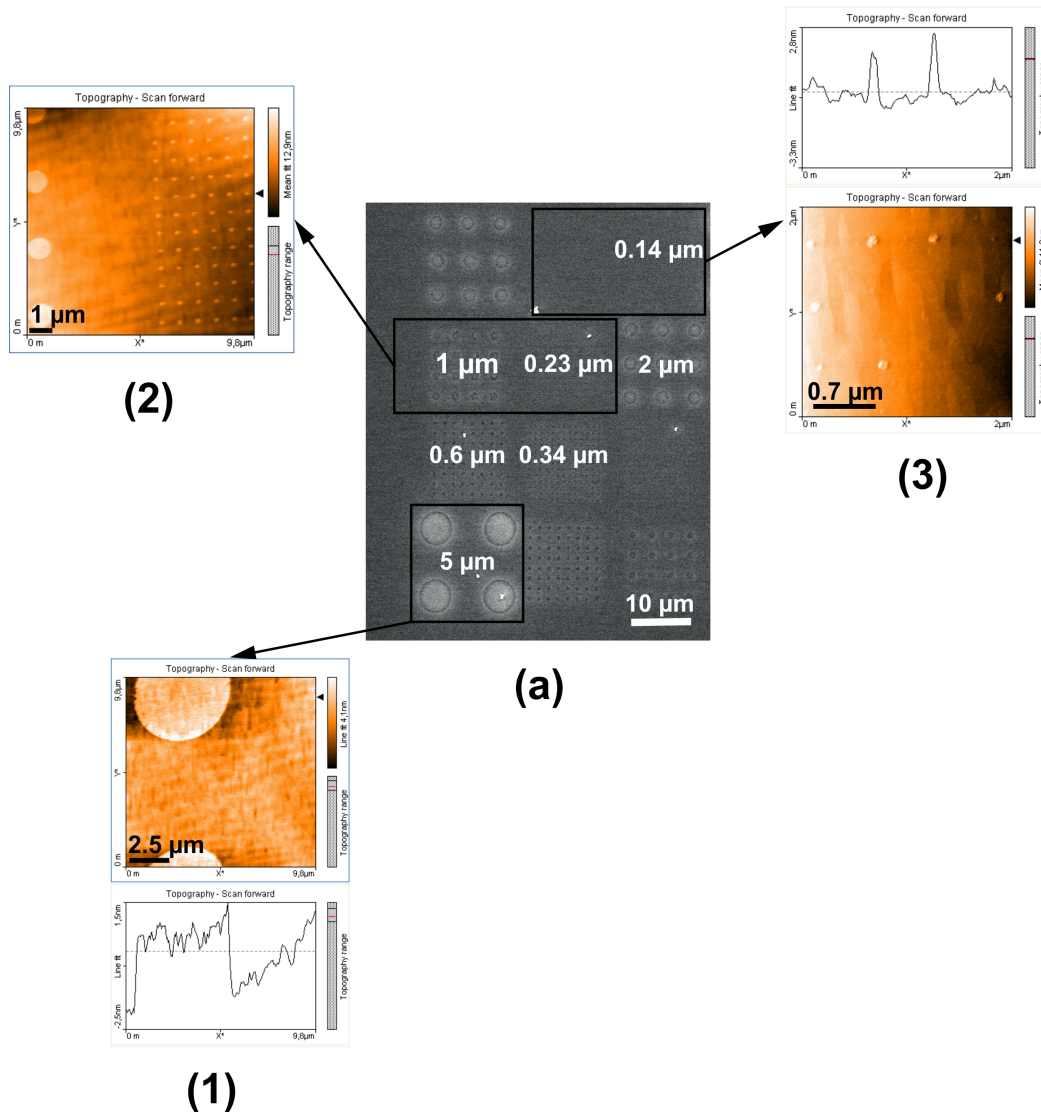


Figure 5.8: Results of 4.5 ML Ga deposition through different aperture sizes from 5  $\mu\text{m}$  down to 100 nm and pitches from 10  $\mu\text{m}$  to 600 nm.

*backside* to avoid clogging of the smallest apertures<sup>7</sup>. Figure 5.8 represents SEM (a) and AFM images (1) - (3) of arrays, where Ga local deposits have

<sup>7</sup>see details regarding to clogging in Section 4.3.2

different sizes. As can be seen in AFM picture **(3)**, a region of  $0,14 \mu\text{m}$ , Ga deposits are present not at every place in the array and the height of a single deposit is just 1-2 nm. These results confirm an aforementioned statement that through the smaller apertures much more Ga should be deposited to obtain the same droplet sizes and heights as for larger ones.

In a final test, 10 ML of Ga were deposited through the mask *M4 – 2* to obtain a single structure formation within the smallest aperture area, i. e., 100 nm. All other growth parameters were identical to those described in the previous experiment. The result of this deposition is presented in Figure 5.9.

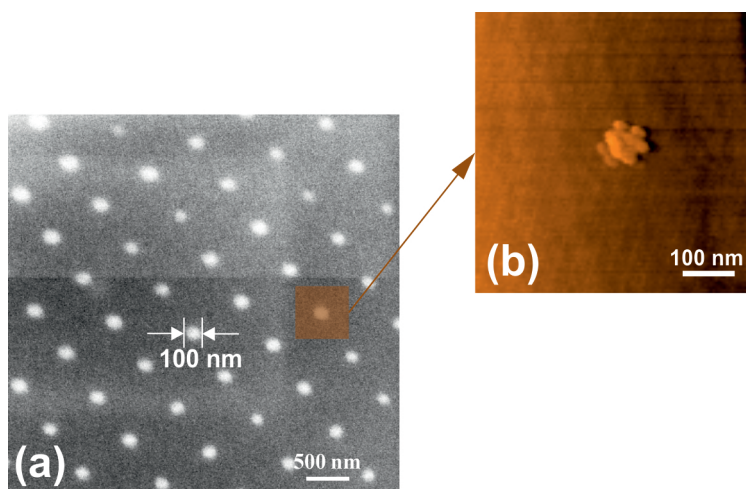


Figure 5.9: SEM image of an array of Ga deposits **(a)**, after [108]. AFM picture of a single local deposit **(b)**.

An average diameter of the Ga local deposits corresponds to an average diameter of the apertures. Local deposits are quite uniform and every single deposit, a cluster, consists of a few tiny Ga droplets (see Figure 5.9 **(b)**). Size variations of Ga deposits are  $\pm 5 \%$ , which can be attributed to the fluctuations in aperture diameters across the mask[108].



As a summary, SADE approach showed a possibility of a structure fabrication with approximately 100 nm lateral resolution. To obtain a site-controlled GaAs QNs, especially QDs, from the local Ga deposits, the deposition parameters have to be further optimized in order to form proper droplets as well as a subsequent crystallization procedure has to be applied. The optimization of deposition parameters is a purpose of the following Section 5.3.

### 5.3 Optimization of a site-controlled droplet formation through the shadow mask

Optimization of deposition parameters for a site-controlled droplet formation employing the smallest mask apertures is a very challenging task. It starts with an understanding of a physical nature of the droplet formation itself and continues with an experimental selection of deposition parameters. As previously described in Section 2.3.2, droplets start to form only if a Ga-rich surface is established. Therefore, the minimum amount of Ga (a pre-coverage layer thickness) that should be deposited to form a Ga-rich surface has to be found accurately. This has a great importance since it permits to understand what is a required Ga amount (a coverage) that should be supplied to form site-controlled Ga nanodroplets within the active area having the smallest aperture sizes.

For the following optimization procedures, the shadow mask *M15 – 2* and quarters of semi-insulating 3 inch GaAs (100) wafers were used. Mask parameters were already discussed in the previous Section 5.2.

All optimization samples were grown as follows:

1. 100 nm thick  $\text{Al}_{0.3}\text{Ga}_{0.7}\text{As}$  layer at  $T_{sub}=590$  °C and under constant As pressure of  $p_{As}=1.95 \times 10^{-5}$  mbar was deposited.

2. Then, the As flux was stopped by closing both: the As-valve and the mechanical shutter of As cracker cell.  $T_{sub}$  was reduced down to 350 ° C, where at this temperature a pre-coverage layer was deposited at  $F=0.7 \frac{ML}{s}$  to create a Ga-terminated surface. In order to investigate how a pre-coverage layer thickness influences on a Ga out-diffusion from local Ga deposits, different pre-coverage layer thicknesses (1.0-1.3 ML) were deposited.
3. After the formation of the Ga-terminated surface, the substrate was cooled down to 100 °C and then transferred to the *preparation chamber*.
4. This was followed by mask-substrate sandwich creation in the *preparation chamber*<sup>8</sup>.
5. After a transfer of the mask-substrate sandwich back to the *growth chamber*, different Ga coverages were deposited at 100 °C through the mask in As absence<sup>9</sup>. The Ga deposition rate was kept constant  $0.35 \frac{ML}{s}$ . In addition, a cryopump was switched-off for a very short time (<5 min), so it stayed cold and the pressure inside the *growth chamber* was not compromised[133]. Vibrations, caused by the cryopump, influence deposition results: a smearing of the deposited Ga takes place. As follows, no single droplets can be formed within the smallest aperture areas. The comparison between results of 4.5 ML Ga deposition through the 5  $\mu\text{m}$  and 2  $\mu\text{m}$  openings with a switched-on **(a)** and a switched-off cryopump **(b)** are presented in Figure 5.10.
6. After a droplet formation, a 60 s break was applied to achieve an equilibrium, followed by a mask-substrate sandwich transfer to the *preparation chamber*, where it was separated under UHV.

---

<sup>8</sup>50 nm of GaAs were deposited on the *backside* of the mask M15 – 2 before the sandwich creation

<sup>9</sup> $p_{mbe}=3.0 \times 10^{-9} \text{ mbar}$

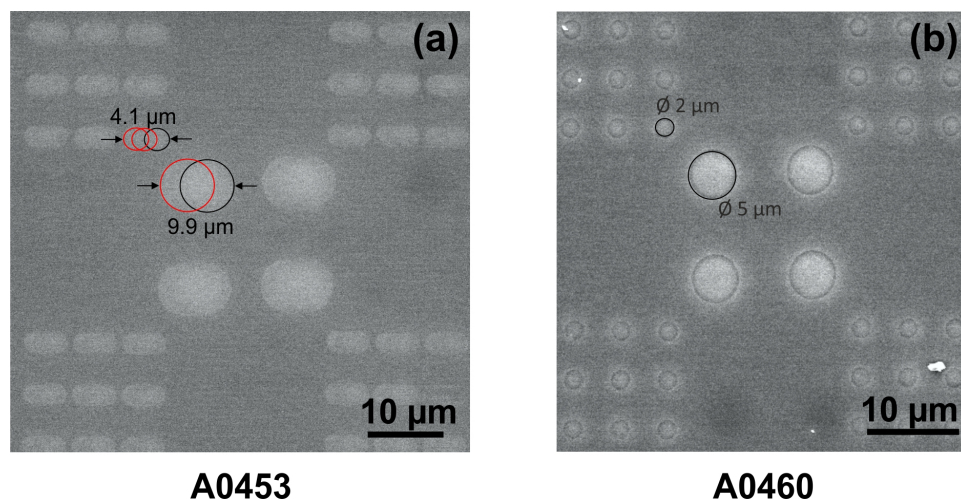


Figure 5.10: Results of 4.5 ML Ga deposition through 5  $\mu\text{m}$  and 2  $\mu\text{m}$  openings. The deposition was performed with a switched-on (a) and a switched-off cryopump (b).

7. Afterward, the substrate was transferred back to the *growth chamber*, where an annealing step at  $T_{anneal}$  in As absence was applied for 5 min to improve a rearrangement of Ga atoms on the surface. This leads to a coarsening by *Ostwald* ripening [142]. Besides, in some experiments, Ga was deposited directly at elevated substrate temperatures omitting a subsequent annealing step.
8. Finally, the mask-substrate sandwich was cooled down to 300 °C and taken out of the MBE system for structural analysis *via* SEM and AFM in a contact mode.

All growth protocols can be found in **Appendix C**.

### 5.3.1 Pre-coverage layer thickness and its effect on droplet formation

In set of experiments below, 40 ML of Ga were deposited locally employing shadow mask *M15-2* after the deposition of a pre-coverage layer with varied from 0 ML to 1.3 thickness, respectively. This was performed to study how the pre-coverage layer affects the droplet formation as well as to find the minimum Ga amount needed for the surface saturation. After the droplet formation, an annealing step was applied at  $T_{anneal}=400$  °C.

In Figure 5.11 (a), as well as in Figure 5.11 (b), bright circular structures of different diameters ordered in regular patterns can be seen. These are the results of the local Ga deposition through the shadow mask *M15-2*. The complete pattern of local Ga deposits on the substrate reproduces the holey pattern in the *Si/Si<sub>3</sub>N<sub>4</sub>*-mask.

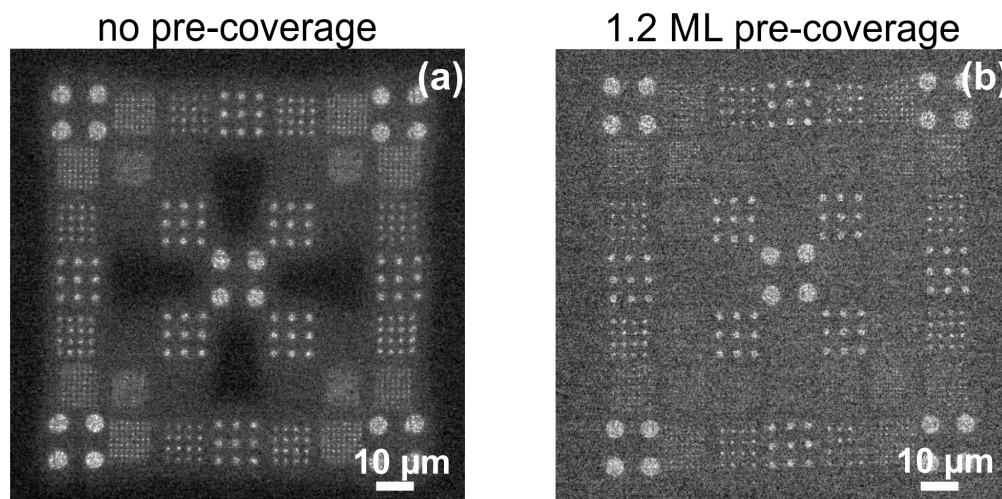


Figure 5.11: SEM images of local Ga deposits reproducing the mask pattern for every single window in the active membrane region, after [133]. Without deposition of a pre-coverage layer, a strong out-diffusion can be seen (a).

Under a close look, slightly bright regions around and also between the circular bright regions are visible in Figure 5.11 (a). These are regions of out-diffused Ga within the aperture areas<sup>10</sup>. Such regions are absent if 1.2 ML of Ga were deposited as pre-coverage before the deposition of the total Ga amount<sup>11</sup> (see Figure 5.11 (b)). Hence, for 1.2 ML pre-coverage layer thickness, the out-diffusion seems to be strongly suppressed. Finally, this points to the reaction of Ga with the As on the surface as a driving force for the strong out-diffusion whereas on a Ga-rich surface this driving force is missing[133]. The obtained value is correlated to those listed in Section 2.3.2 so that 1.2 ML of Ga should be initially deposited to establish a Ga-rich surface. How the pre-coverage layer thickness influences the droplet formation within the different aperture areas is discussed below.

First of all, droplet heights and diameters were measured by AFM in a contact mode. Results of AFM measurements with respect to different aperture sizes and pre-coverage layer thicknesses are presented in Table 5.2. These were used further to estimate the droplet volume and to calculate Ga fraction in droplets.

As an example, Figure 5.12 represents results of the deposition through 0.34  $\mu\text{m}$  apertures. AFM measurements show an increase of the droplet height and diameter with an increase of the pre-coverage layer thickness. Besides, droplets formed after the surface saturation have a more homogeneous distribution of diameters and heights compared to ones formed on non-saturated surfaces. As a general tendency regarding droplet diameters and heights, a decrease in both characteristics in a range of approximately 40 % with a decreasing of an aperture size can be stated[133].

For calculation of Ga fraction<sup>12</sup>, the droplet volume  $V_{droplet}$  was estimated

---

<sup>10</sup> Ga out-diffuses from the local Ga deposits

<sup>11</sup>40 ML

<sup>12</sup>a fraction of Ga, which is deposited through the aperture, actually present in droplets

Table 5.2: Diameters and heights of Ga droplets with respect to aperture sizes and pre-coverage layer thicknesses.

		<i>Droplets</i>				
<i>Pre – coverage</i>		0 ML	1.0 ML	1.1 ML	1.2 ML	1.3 ML
<i>Diameter of droplets, nm</i>	5,0 $\mu\text{m}$	60-120	60-120	130	140	160
	2,0 $\mu\text{m}$	80-130	60-110	125	135	160
	1,0 $\mu\text{m}$	90-140	85-110	120	130	150
	0,6 $\mu\text{m}$	90-150	75-90	115	125	140
	0,34 $\mu\text{m}$	120	80-105	110	120	130
	0,23 $\mu\text{m}$	0	90	100	120	120
	0,14 $\mu\text{m}$	0	0	0	100	110
<i>Height of Ga droplets, nm</i>	5,0 $\mu\text{m}$	30	25	28	29	30
	2,0 $\mu\text{m}$	28	20	26	28	29
	1,0 $\mu\text{m}$	26	17	23	26	28
	0,6 $\mu\text{m}$	23	15	22	25	26
	0,34 $\mu\text{m}$	20	14	21	23	24
	0,23 $\mu\text{m}$	0	12	17	19	21
	0,14 $\mu\text{m}$	0	0	0	15	18

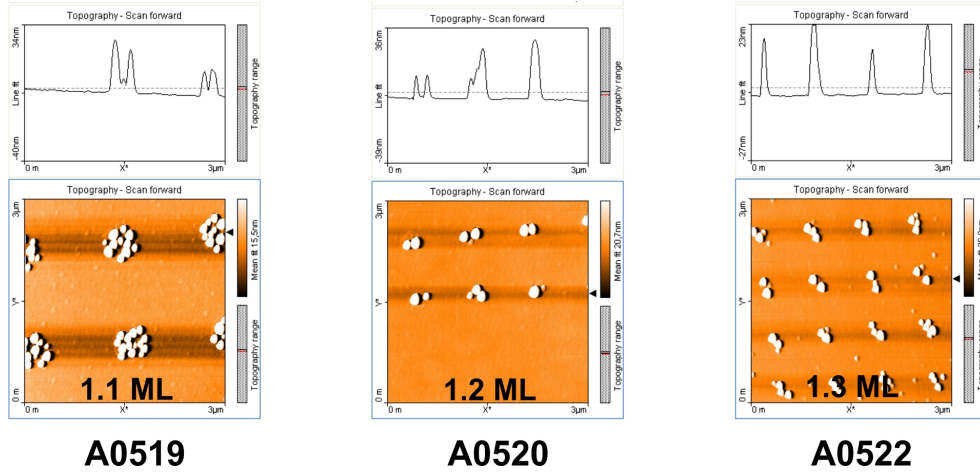


Figure 5.12: AFM images of Ga deposits obtained through  $0.34 \mu\text{m}$  opening. The scan area was  $3 \times 3 \mu\text{m}^2$ . The pre-coverage layer thickness was varied from sample A0519 to sample A0522.

from average droplet diameters  $d_{\text{droplet}}$  and heights  $h_{\text{droplet}}$  (see Table 5.2) assuming a semi-spherical cap shape of the droplet by the following relation:

$$V_{\text{droplet}} = \frac{\pi}{6} h_{\text{droplet}} \left( \frac{3}{4} d_{\text{droplet}}^2 + h_{\text{droplet}}^2 \right) \quad (3)$$

In Table 5.3, the number of Ga droplets per aperture (*Row 1*), as well as the fraction of deposited Ga found in the droplets (*Row 2*), are summarized with respect to different pre-coverage layer thicknesses and aperture sizes, respectively. The larger the aperture size the larger the Ga amount passes through the aperture and, as a result, the bigger the number of Ga droplets formed per the aperture area, so that  $5 \mu\text{m}$  and  $2 \mu\text{m}$  apertures are out of this calculation. Ga fractions lie in a range from 10 to 40 %, except for the pre-coverage layer thickness of 1.3 ML. Although these values have a quite large error bar, it looks obvious that a significant fraction of Ga does not contribute to the droplet formation. The general trend here is that the less the pre-coverage layer thickness or the smaller the aperture size in the

Table 5.3: Structural properties of Ga droplets. The fraction of Ga in the droplets was calculated considering the average droplet volume. For each data set at least 20 droplets were evaluated, after [133].

		<i>Droplets</i>				
<i>Pre – coverage</i>		0 ML	1.0 ML	1.1 ML	1.2 ML	1.3 ML
<i>Number of droplets per aperture</i>	1,0 $\mu\text{m}$	18.3	18.8	35.1	32.2	52.2
	0,6 $\mu\text{m}$	7.3	8.5	10.8	6.8	14.5
	0,34 $\mu\text{m}$	1.1	1.9	2.8	2.9	5.1
	0,23 $\mu\text{m}$	0.0	1.2	1.54	1.1	2.5
	0,14 $\mu\text{m}$	0.0	0.0	0.0	1.0	1.8
<i>Fraction of Ga in droplets, %</i>	0,6 $\mu\text{m}$	49	15	37	36	81
	0,34 $\mu\text{m}$	10	8	32	32	64

shadow mask, the less Ga is found in the droplets. All results are consistent with the out-diffusion of Ga from the aperture area, which is suppressed by a Ga-termination of the surface. Without deposition of the pre-coverage layer, the out-diffusion is the strongest, and with an increase of pre-coverage layer thickness, it tends to reduce until too much free Ga is on the surface, so that the droplets are formed everywhere on the surface. For deposition conditions described above, 1.2 ML is the optimum value, but even for this pre-coverage thickness, it seems impossible to suppress the Ga out-diffusion process completely as the reduced fraction of Ga in the droplets indicates. The reason can be a not perfect Ga-termination of the surface due to small amounts of As absorbed during the substrate handling and transfer from the *growth chamber* to the *preparation chamber* and back.

Without deposition of the pre-coverage layer (see *Column 0 ML* in Table 5.3), no droplets for the two smallest aperture sizes were observed and the total numbers of Ga droplets for larger apertures were not very high. In cases



of 1.0 ML and 1.1 ML pre-coverages (*Columns 1.0 ML* and *1.1 ML* in Table 5.3), the droplets were formed in 0.23  $\mu\text{m}$  aperture area, but still, no droplets found to be within 0.14  $\mu\text{m}$  aperture areas. Further increase of pre-coverage layer thickness gave the formation of droplets within the 0.14  $\mu\text{m}$  aperture areas. Thus, the total number of Ga droplets formed per aperture area increases with an increase of the pre-coverage layer thickness. For 1.3 ML, the number of droplets was further increased and droplets were also formed between the apertures. In other words, under these conditions after the surface saturation, excess of Ga leads to the droplet formation everywhere.

The result of local Ga deposition through the smallest apertures at optimum parameters<sup>13</sup> is presented in Figure 5.13. The single droplet has diameter [height] of 100 nm [15 nm]. As can be seen in Figure 5.13, some droplets in the array are missing. This happened more likely due to full or partial clogging of the apertures in *Si/Si<sub>3</sub>N<sub>4</sub>*-mask.

### 5.3.2 Coverage layer thickness

In the following section, results of a local Ga deposition employing shadow mask *M15-2* with different aperture sizes as a function of the coverage layer thickness are discussed. For that, prior the deposition of the coverage layer, 1.2 ML of Ga were deposited as described above. The Ga coverage was varied from 2.75 to 40 ML. Results of Ga depositions are presented in Figure 5.14 and in Table 5.4.

Without applying an annealing step, a rather homogeneous deposit in the whole aperture area with only rudiments of the droplet formation is observed (see *the first Column* of SEM images in Figure 5.14). After the annealing step, Ga droplets are formed, but the exact result depends on the aperture

---

<sup>13</sup> $T_{sub}=100$  °C, 1.2 ML as a pre-coverage layer, 40 ML coverage and annealing at  $T_{anneal}=400$  °C for 5 min

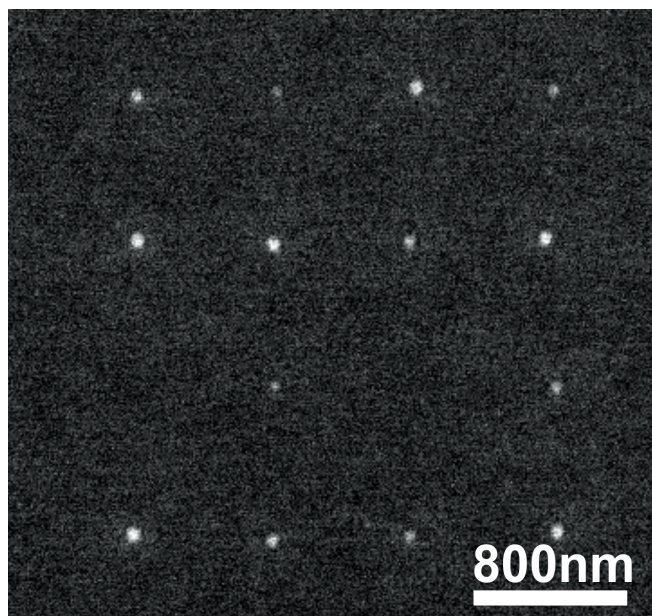


Figure 5.13: Array of Ga droplets deposited through  $0.14 \mu\text{m}$  openings. The deposition was performed at optimum conditions.

diameter and the Ga coverage. The larger the Ga coverage layer thickness the larger the amount of Ga deposited through the smallest apertures, i. e.,  $0.14 \mu\text{m}$  and  $0.23 \mu\text{m}$ .

Table 5.4 presents results of a structural analysis of local Ga deposits for every aperture size concerning the Ga coverage layer thickness. The general tendency for each aperture size is a decrease of the coverage thickness entails a decrease of an average number of droplets per aperture area. As a single example, the number of droplets was slightly reduced for the depositions of 40 and 37.5 ML through  $0.6 \mu\text{m}$  aperture (7 droplets per aperture compared to 8). For  $0.14 \mu\text{m}$ , the formation of a single droplet per aperture was observed only if 40 ML of Ga were deposited, but no droplets at all were found for other coverages. This observation can be mainly attributed to the above-discussed out-diffusion of Ga atoms from local Ga deposits. For the

Table 5.4: The diameter, height and number of Ga droplets deposited per each aperture size with respect to a deposited Ga coverage layer thickness.

		<i>Droplets</i>			
<i>Coverage</i>		40 ML	37.5 ML	35 ML	2.75 ML
<i>Number of droplets</i>	5,0 $\mu\text{m}$	780.8	760.2	740.8	110.3
	2,0 $\mu\text{m}$	115.5	100.3	95.6	0.0
	1,0 $\mu\text{m}$	32.2	28.5	26.2	0.0
	0,6 $\mu\text{m}$	6.8	6.5	5.5	0.0
	0,34 $\mu\text{m}$	2.9	2.3	1.4	0.0
	0,23 $\mu\text{m}$	1.1	0.8	0.7	0.0
	0,14 $\mu\text{m}$	1.0	0.0	0.0	0.0
<i>Diameter of droplets, nm</i>	5,0 $\mu\text{m}$	140	90-135	130	60
	2,0 $\mu\text{m}$	135	95-130	130	0
	1,0 $\mu\text{m}$	130	95-120	125	0
	0,6 $\mu\text{m}$	125	95-115	120	0
	0,34 $\mu\text{m}$	120	95-110	120	0
	0,23 $\mu\text{m}$	120	100	100	0
	0,14 $\mu\text{m}$	100	0	0	0
<i>Height of Ga droplets, nm</i>	5,0 $\mu\text{m}$	29	28	26	7
	2,0 $\mu\text{m}$	28	26	25	0
	1,0 $\mu\text{m}$	26	25	23	0
	0,6 $\mu\text{m}$	25	24	22	0
	0,34 $\mu\text{m}$	23	20	18	0
	0,23 $\mu\text{m}$	19	15	12	0
	0,14 $\mu\text{m}$	15	0	0	0

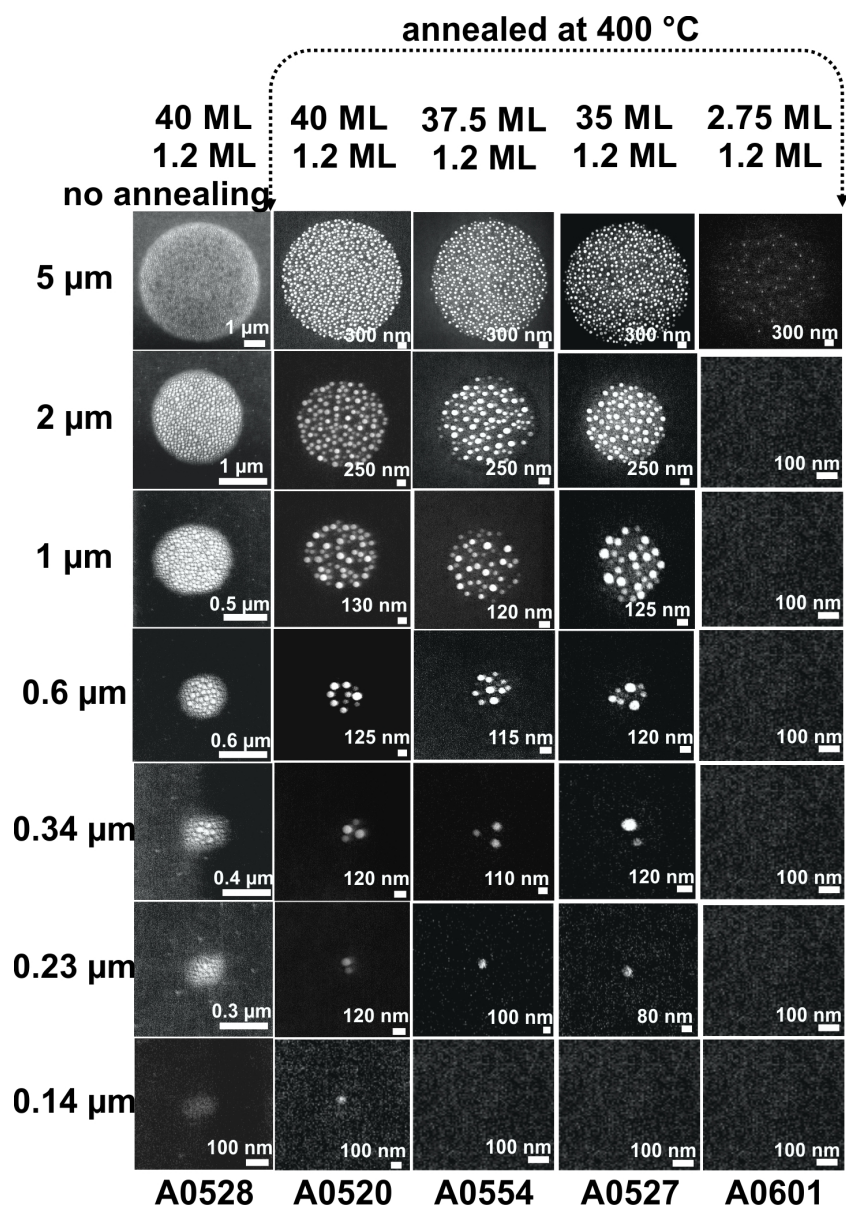


Figure 5.14: Results of local Ga deposition through apertures having different sizes. The coverage thickness was varied from 2.75 ML to 40 ML.

smallest aperture sizes, a larger Ga amount will be lost from the total Ga coverage deposited through the aperture area for the same migration length

of Ga. Thus, no droplet were found in the smallest aperture areas whereas the number of droplets was only reduced for the larger ones.

As a summary, results of the structural analysis of local Ga deposits presented in Table 5.4 show an increase of heights and diameters of Ga droplets with respect to an increase of the aperture diameter and the coverage layer thickness. This tendency is valid for all aperture diameters. Within the aperture sizes of 0,14  $\mu\text{m}$  and 0,23  $\mu\text{m}$ , Ga droplets were only formed if 40 ML of Ga were deposited through the shadow mask at deposition conditions described above. Due to a temperature-dependent Ga diffusion process, the further optimization of deposition parameters will be discussed in terms of  $T_{sub}$ . This may offer a new way to reduce a Ga coverage in case of a deposition performed through the smallest apertures.

### 5.3.3 Two-step deposition procedure *vs* direct deposition at elevated temperatures

In DE procedure, the size and the density of Ga deposits, nanoclusters, are strongly dependent on the substrate temperature[67]. The Ga nanocluster density *vs*  $T_{sub}$  follows a scaling law when these are deposited under 200 °C. This scaling law is broken when deposition is performed at over then 200 °C[15]. Under this temperature, nanoclusters begin to coalesce, which drastically reduce their number. This process is governed by the *Ostwald* ripening. It is supposed that Ga atoms detach more readily from smaller Ga deposits and condense rather to larger ones[142]. For the local Ga deposition through the shadow  $Si/Si_3N_4$ -mask, this means that the number of droplets formed within the aperture area will be decreased whereas average diameters [heights] will be increased. In the case of the small aperture sizes, this means a formation of a single droplet instead of a few small ones. How the substrate temperature affect the droplet formation is discussed below.

As already mentioned, there are two approaches to form Ga droplets within the aperture area: a two-step procedure **i** or a direct deposition at elevated temperature **ii**. The two-step procedure was applied in the previous experiments and it can be generally described as follows:

1. The Ga is deposited through the apertures in the shadow mask at  $T_{sub}=100$  °C. At such temperature, Ga atoms are ‘frozen’ onto the surface and local Ga deposits repeat the exact mask pattern (see *the first column* of SEM images in Figure 5.14). The size of a single rudiment within the local deposit area lies in the range from 15-80 nm as well as a height is around 5 nm.
2. After applying the heat treatment (annealing), Ga rearranges on the surface within the local deposit area and proper droplets are formed. The key parameter here is the annealing temperature  $T_{anneal}$ <sup>14</sup>. An increase of  $T_{anneal}$  leads to an increase of the Ga migration length. In its turn, this leads to the rearrangement of Ga on the surface within the local deposit area. This is consistent with results that for lower annealing temperatures, a droplet formation is observed for lower Ga coverages, so the out-diffusion seems to be reduced (see Figure 5.15)[133].

As can be seen in Figure 5.16, a decrease in the droplet number, as well as an increase of the droplet size, are observed with increase of  $T_{anneal}$ , respectively.  $T_{anneal}$  of 400 °C seems to be the upper limit for a site-controlled droplet formation because at 430 °C the droplets spread over the area that is significantly larger than the aperture area[133].

In contrast to a two-step deposition procedure, Figure 5.17 presents results of a direct deposition through 1  $\mu$ m apertures at different substrate temperatures (200 – 400 °C). The annealing step is omitted.

---

<sup>14</sup>very probably also the annealing time, but this was fixed to 5 min for all experiments

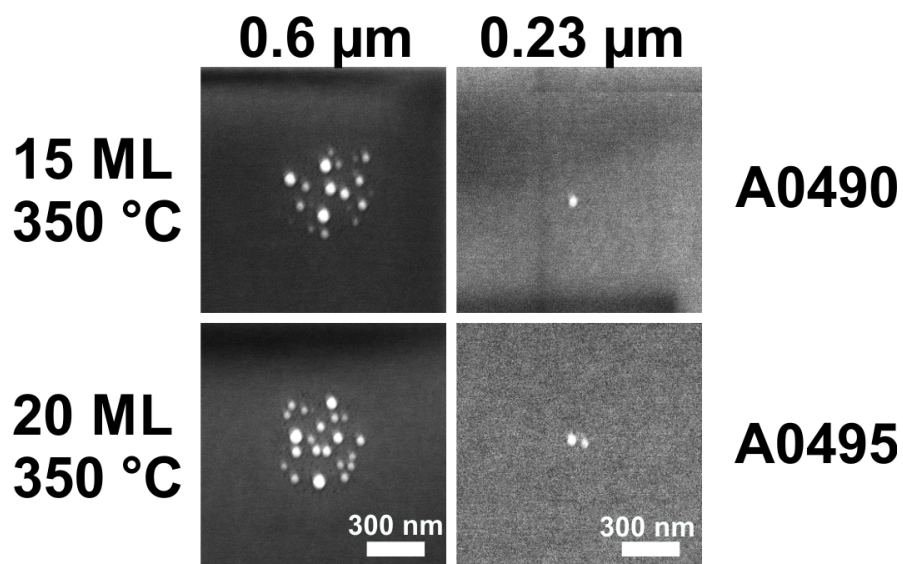


Figure 5.15: SEM images showing results of Ga deposition in a two-step procedure for two different Ga amounts, after [133]. These results can be compared to results of the depositions through the same aperture sizes but annealed at  $T_{anneal}=400$  °C.

Results of a direct deposition at elevated temperatures are quite similar to obtained during a two-step deposition procedure: the higher the  $T_{sub}$  the lower number of droplets and the stronger the Ga out-diffusion. Consequently, a comparison of results of a direct and a two-step deposition procedures through an array of  $0,23 \mu\text{m}$  apertures is presented in Figure 5.18. The sizes [heights] of Ga droplets in the arrays are different: 120 nm [19 nm] for a two-step procedure compared to 70 nm [7 nm] for a direct deposition. Besides, in case of a direct deposition, the number of droplets per aperture area was increased. It looks as a required  $T_{sub}$  for obtaining a certain droplet density is slightly lower for a direct deposition at elevated temperature then for a two-step deposition procedure. The reasons can be either different real substrate temperature values in cases of a direct deposition (presence of the shadow

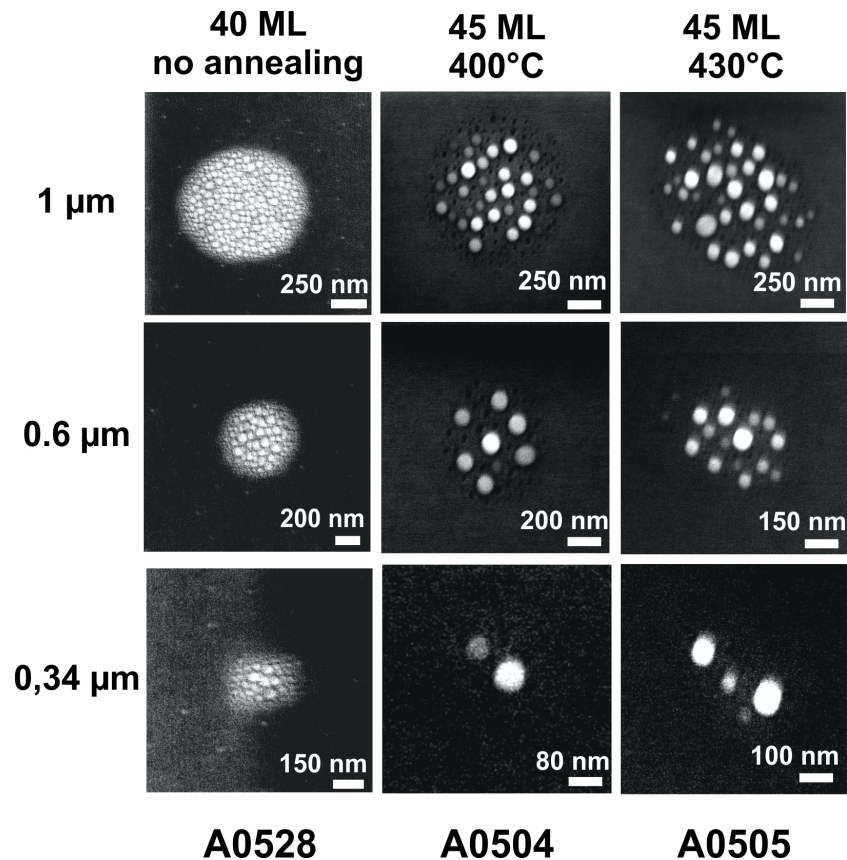


Figure 5.16: SEM images of Ga deposits annealed at different  $T_{anneal}$ .

mask during the deposition stage) and a two-step procedure (an annealing of a bare substrate) or simply the difference in process cycles. Besides this, a direct deposition at elevated temperatures gives a lower positioning precision (see Figure 5.18 (b)) compared to a two-step deposition procedure (see Figure 5.18 (a)).

Thereafter, a two-step deposition procedure shows a better control of the droplet formation as well as a quite high positioning precision (see Figure 5.18 (a)). There are three main deposition parameters determining the number of droplets per the smallest apertures, 0,14  $\mu\text{m}$  and 0,23  $\mu\text{m}$ , in a two-step



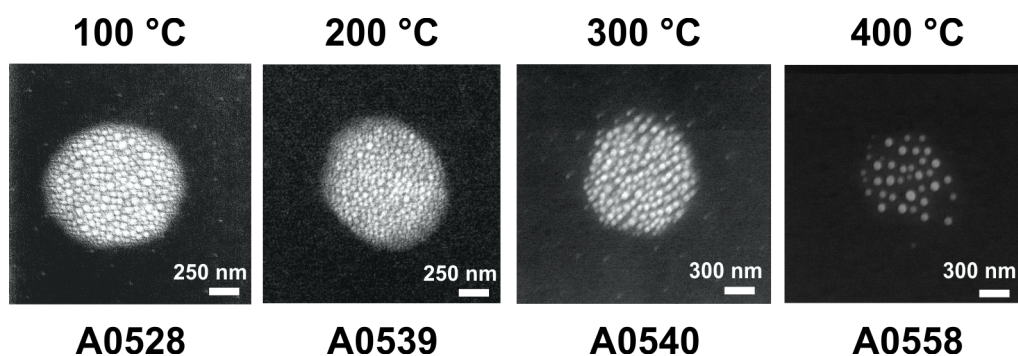


Figure 5.17: SEM images of Ga deposits deposited at different temperatures. The aperture size is  $1 \mu\text{m}$ .

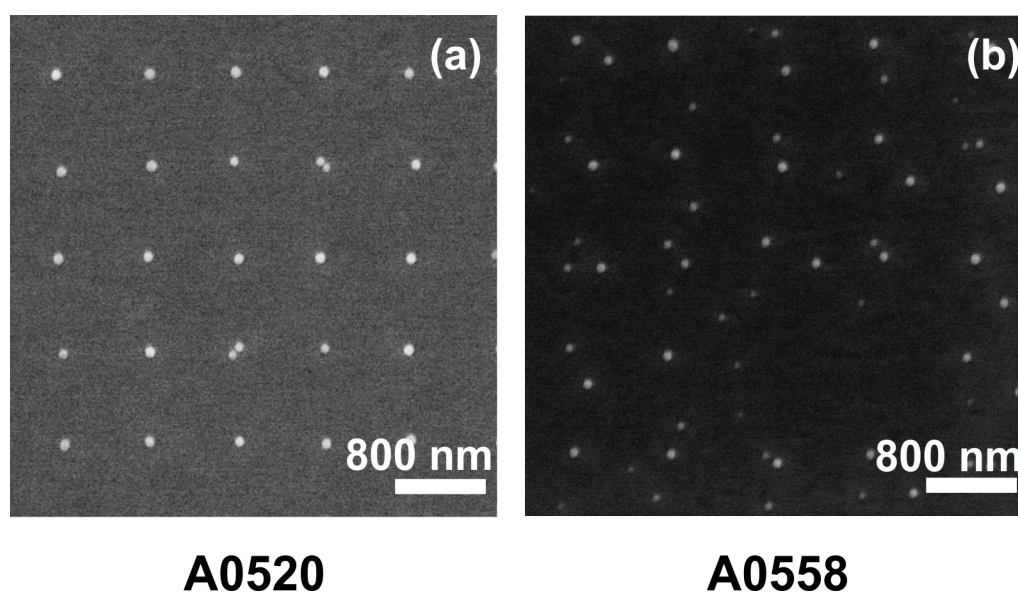


Figure 5.18: Arrays of Ga droplets deposited at  $T_{sub}=100 \text{ }^\circ\text{C}$  with a subsequent annealing at  $T_{anneal}=400 \text{ }^\circ\text{C}$  (a) and deposited directly at  $T_{sub}=400 \text{ }^\circ\text{C}$  (b). The aperture size in the shadow mask is  $0,23 \mu\text{m}$ . Pre-coverage and coverage layer thicknesses are 1.2 ML and 40 ML, respectively.

deposition approach: pre-coverage and coverage layer thicknesses as well as an annealing temperature  $T_{anneal}$ . By choosing the right combination of these

parameters, a single droplet per individual aperture can be obtained. The optimum conditions for a site-controlled droplet formation within the  $0,23 \mu\text{m}$  aperture were found as follows: a pre-coverage layer thickness - 1 ML, a coverage layer thickness - 40 ML, the deposition and annealing temperatures -  $T_{sub}=100 \text{ }^\circ\text{C}$  and  $T_{anneal}=400 \text{ }^\circ\text{C}$ , respectively. The array of site-controlled Ga droplets is presented in Figure 5.19.

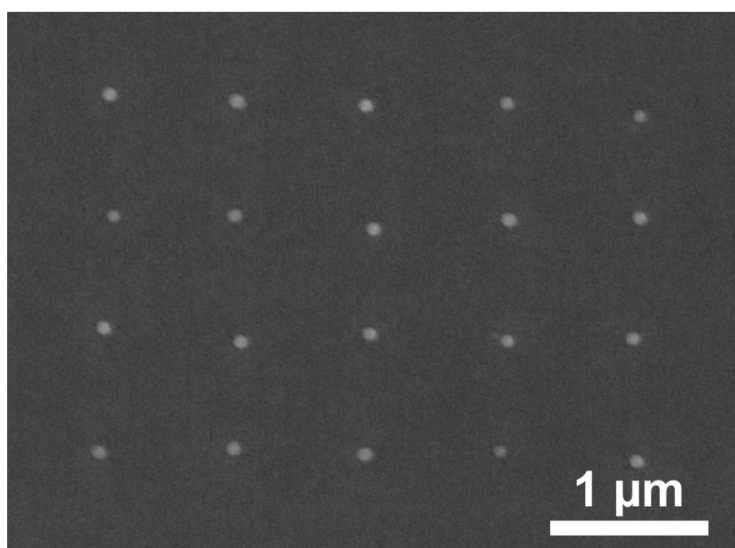


Figure 5.19: Array of Ga droplets obtained by a deposition through  $0,23 \mu\text{m}$  apertures, after [133].

Under employed process conditions, a probability to create a single droplet per aperture is found to be larger than 90 % and an average droplet diameter [height] is 90 nm [12 nm]. By comparing the droplet pattern to the image of the corresponding mask region, the positioning precision was estimated to  $\pm 50 \text{ nm}$  (see Figure 5.20).

Figure 5.20 shows that Ga droplets are formed indeed completely within the aperture area but with a homogeneous spatial distribution and not preferably in the center of the aperture area[133]. As a result, a positioning resolution

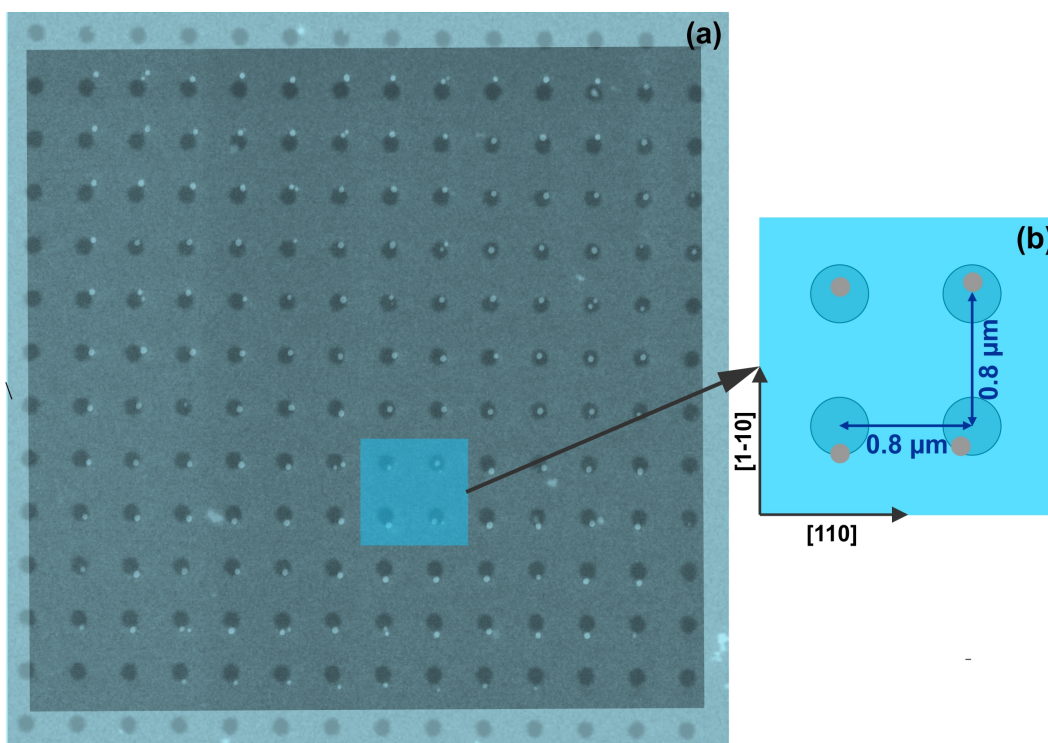


Figure 5.20: Array of Ga droplets deposited through  $0,23 \mu\text{m}$ . SEM images of droplet and hole arrays were combined into one picture (a). The array of droplets repeats the mask pattern. The spatial dimensions are depicted in (b).

is given by the aperture size, i. e.,  $0,23 \mu\text{m}$ . Hence, the conclusion is for a higher positioning precision the smaller aperture sizes have to be employed.

As a next step, such array of Ga nanodroplets can be transformed into an array of GaAs QNs applying a crystallization step in As atmosphere. This could be a good start in a follow-up study.

Finally, the proposed SADE approach opened a new path to the fabrication of site-controlled QNs and their potential integration into optoelectronic devices.

## Summary and outlook

The purpose of this thesis was a fabrication of nanostructures on predefined areas employing shadow mask-assisted MBE technique. In order to achieve this goal, the whole work was divided into two main parts.

In the first part, the special shadow mask design was created. All mask dimensions were selected in order to fit it into a customized mask plate. The special mask construction allows a freedom to choose sizes of apertures as well as to control the gap between the mask and the substrate during the deposition. The mask fabrication technology was discussed in detail and implemented resulting in a successful mask production on  $Si/Si_3N_4$ -basis. A large number of masks were produced with different mask parameters. Their compatibility with UHV was proven and showed full compatibility with the MBE procedure. Based on this, the mask *ex-situ* and *in-situ* cleaning steps were developed to avoid a contamination of the MBE system, as well as the substrate, during the mask use. Also, it was found that aperture sizes can be slightly reduced *in-situ* by a deposition of a certain GaAs layer thickness on the *backside* of the mask.

In the second part, a shadow masked SAE approach was applied to form site-controlled Ga nanodroplets on GaAs (100) *via* the DE method. First of all, key aspects of the deposition through the shadow mask were discussed. It was found that the mask-substrate gap, as well as a working cryopump,

have the main influence on the lateral resolution in case if the perpendicular deposition source was used. Thereby, all depositions through the mask were performed with the mask *M15-2*, having no gap with the substrate, and with a switched-off cryopump. Secondly, a low deposition rate of Ga ( $0.03 \frac{ML}{s}$ ) was used to provide a low-density regime, which is important for a site-controlled nanostructure growth. Thirdly, several depositions with Ga were performed through the mask to understand processes of the Ga nanodroplet formation itself. As a result, it was obtained that the smaller the aperture size in the mask the larger the Ga amount should be deposited. The pre-coverage layer thickness was found to have a strong influence on the Ga out-diffusion process, i.e., Ga nanodroplets start to form only if the surface is a Ga-terminated. A substrate temperature, a Ga coverage, as well as post-deposition annealing parameters, affect deposition results. Thus, the optimum deposition parameters were selected experimentally for the case of a single per aperture droplet occupancy.

This work can be continued as a study of the crystallization process, where positioned Ga nanodroplets can be transformed in As atmosphere into GaAs QNs. It would be also interesting to investigate optical and electrical properties of such structures.

In conclusion, this thesis reveals a new interesting approach of a site-controlled QN fabrication.

# Bibliography

- [1] A. Latyshev, A. Dvurechenskii and A. Aseev, *Advances in Semiconductor Nanostructures. Growth, Characterization, Properties and Applications*, Elsevier, 552 (2016).
- [2] S. Suresh, *Semiconductor Nanomaterials, Methods and Applications: A Review*, Nanoscience and Nanotechnology, 3, 3 (2013).
- [3] D. Kim, *III-V Nanostructures for Photovoltaics Applications*, University College London, conference proceedings, December (2018).
- [4] B. Maye, S. Wirths, H. Schmid, S. Mauthe, C. Convertino, Y. Baumgartner, L. Czornomaz, M. Sousa, H. Riel and K. E. Moselund, *Monolithic integration of III-V nanostructures for electronic and photonic applications*, Proceedings in Low-Dimensional Materials and Devices, 10349 (2017).
- [5] H. Mäntynen, N. Anttu, Z. Sun and H. Lipsanen, *Single-photon sources with quantum dots in III-V nanowires*, Nanophotonics, 8, 5 (2019).
- [6] T. X. Wang, L. Xu, Y. Jiang and Z. Yin, *III-V compounds as single photon emitters*, Journal of Semiconductors, 40, 7 (2019).
- [7] T. Kuech, *Handbook of Crystal Growth: Thin Films and Epitaxy*, Elsevier, 1345 (2015).

- [8] W. C. Ballamy and A. Y. Cho, *Planar isolated GaAs devices produced by molecular beam epitaxy*, IEEE Transactions on Electron Devices, 23, 4 (1976).
- [9] G. H. Döhler, G. Hasnain, and J. N. Miller, *In-situ grown-in selective contacts to n-i-p-i doping superlattice crystals using molecular beam epitaxial growth through a shadow mask*, Appl. Phys. Lett., 49, 704 (1986).
- [10] S. C. Lee, L. R. Dawson, K. J. Malloy, and S. R. J. Brueck, *Molecular-beam epitaxial growth of one-dimensional rows of InAs quantum dots on nanoscale-patterned GaAs*, Appl. Phys. Lett., 79, 2630 (2001),
- [11] W. T. Tsang and A. Y. Cho, *Growth of GaAs-Ga<sub>1-x</sub>Al<sub>x</sub>As over preferentially etched channels by molecular beam epitaxy: A technique for two-dimensional thin-film definition*, Appl. Phys. Lett., 30, 293 (1977).
- [12] A. Lorke, J. H. English, A. C. Gossard and P. M. Petroff, *Tapered GaAs quantum wells and selectively contactable two-dimensional electron gases grown by shadow masked molecular-beam epitaxy*, Journal of Applied Physics 77, 3578 (1995).
- [13] P. Bhattacharya, S. Ghosh and A. Stiff-Roberts, *Quantum dot optoelectronic devices*, Annual Review of Materials Research, 34 (2004).
- [14] J. H. Lee, Zh. M. Wang, E. S. Kim, N. Y. Kim, S. H. Park and G. J. Salamo, *Various Quantum- and Nano-Structures by III-V Droplet Epitaxy on GaAs Substrates*, Nanoscale Research Letters, 5, 308 (2009).
- [15] J. Wu and Z. M. Wang, *Droplet epitaxy for advanced optoelectronic materials and devices*, Journal of Physics D: Applied Physics, 47, 17 (2014)

- [16] M. Grundmann, *The Physics of Semiconductors. An Introduction Including Devices and Nanophysics*, Springer (2006).
- [17] T.J. Seebeck, *Magnetische Polarisation der Metalle und Erze durch Temperaturdifferenz*, Abhandl. Deut. Akad. Wiss. Berlin, 265–373 (1822).
- [18] W.B. Shockley, *Circuit Element Utilizing Semiconductor Material*, US patent 2,569,347 (1948).
- [19] J. Königsberger and J. Weiss, *Über die thermoelektrischen Effekte (Thermokräfte, Thomsonwärme) und die Wärmeleitung in einigen Elementen und Verbindungen und über die experimentelle Prüfung der Elektronentheorien*, Ann. Phys. 35, 1 (1911).
- [20] J. Orton, *The story of semiconductors*, Oxford university press, 510 (2004).
- [21] S. M. Sze and K. K. Ng, *Physics of semiconductor devices*, John Wiley Sons (1996).
- [22] J. Singh, *Optoelectronics: An introduction to materials and devices*, McGraw-Hill College (1996).
- [23] S. Kasap and P. Capper, *Springer Handbook of Electronic and Photonic Materials*, Springer (2017).
- [24] "Atomic weights of the elements 2013", Pure App Chem 88, 265-291, (2016)  
<https://www.periodni.com/images.html>
- [25] N. Bruce Hannay and U. Colombo, *Electronic Structure of Semiconductors*, Plenum Press, 1-40 (1973).



- [26] U. W. Pohl, *Epitaxy of Semiconductors: Introduction to Physical Principles*, Springer (2013).
- [27] L. Vegard, *Die Konstitution der Mischkristalle und die Raumfüllung der Atome*, Zeitschrift für Physik, 5, 17–26 (1921)
- [28] I. Vurgaftman, J. R. Meyer and L. R. Ram-Mohan, *Band parameters for III-V compound semiconductors and their alloys*, Journal of Applied Physics, 89 (2001).
- [29] P. Y. Yu and M. Cardona, *Fundamentals of semiconductors: physics and materials properties*, Springer (2010).
- [30] M. A. Herman, W. Richter, and H. Sitter, *Epitaxy: physical principles and technical implementation*, Springer (2004).
- [31] M. Herman and H. Sitter, *Molecular Beam Epitaxy: Fundamentals and Current Status*, Springer-Verlag (1989).
- [32] J. Venables, G. D. T. Splitter and M. Hanbrücken, *Nucleation and growth of thin films*, Reports on Progress in Physics, 47 (1984).
- [33] J. Palisaitis, *Epitaxial growth of thin films*, Physics of Advanced Materials, Winter School (2008).
- [34] H. Brune, *Epitaxial Growth of Thin Films*, Surface and Interface Science, 4 (2013)
- [35] F. Frank and J. H. van der Merwe, *One-dimensional dislocations. I. Static theory*, Proceedings of the Royal Society of London A: Mathematical, Physical and Engineering Sciences, 198 (1949).
- [36] J. Palisaitis and R. Vasiliauskas, *Epitaxial growth of thin films* Physics of Advanced Materials, (2008)

- [37] M. Volmer and A. Weber, *Keimbildung in übersättigten Gebilden*, Zeitschrift für physikalische Chemie, 119 (1926).
- [38] I. N. Stranski and L. Krastanow, *Zur Theorie der orientierten Ausscheidung von Ionenkristallen aufeinander*, Monatshefte für Chemie und verwandte Teile anderer Wissenschaften, 71 (1937).
- [39] D. Bimberg, *Semiconductor Nanostructures*, Springer (2008).
- [40] V. Klimov, *Nanocrystal quantum dots*, Taylor and Francis Group, LLC, 453 (2010).
- [41] P. Harrison, *Quantum wells, wires and dots*, Wiley Interscience (2005).
- [42] L. Jacak, P. Hawrylak, and A. Wójs, *Quantum dots*, Springer (1998).
- [43] D. Bimberg, M. Grundmann, N. N. Ledentsov, *Quantum dot heterostructures*, John Wiley and Sons (1999).
- [44] O. G. Schmidt, *Lateral Alignment of Epitaxial Quantum Dots*, Springer (2007)
- [45] M. Sugawara, *Self-assembled InGaAs/GaAs Quantum Dots*, Semiconductors and Semimetals, 60 (1999).
- [46] P. Michler, A. Kiraz, C. Becher, W.V. Schoenfeld, P.M. Petroff, L. Zhang, E. Hu and A. Imamoglu, *A Quantum Dot Single-Photon Turnstile Device*, Science, 290, 2282 (2000).
- [47] Z. Yuan, B.E. Kardynal, R.M. Stevenson, A.J. Shields, C.J. Lobo, K. Cooper, N.S. Beattie, D.A. Ritchie and M. Pepper, *Electrically Driven Single-Photon Source*, Science, 295, 102 (2002)

- [48] Y. Nakamura, O.G. Schmidt, N.Y. Jin-Phillipp, S. Kiravittaya, C. Mueller, K. Eberl, H. Graebeldinger and H. Schweizer, *Vertical alignment of laterally ordered InAs and InGaAs quantum dot arrays on patterned (001) GaAs substrates*, J. Cryst. Growth, 242, 339 (2002).
- [49] H. Lee, J.A. Johnson, M.Y. He, J.S. Speck and P.M. Petroff, *Strain-engineered self-assembled semiconductor quantum dot lattices*, Appl. Phys. Lett., 78, 105 (2001).
- [50] S. Kohmoto, H. Nakamura, T. Ishikawa, and K. Asakawa, *Site-controlled self-organization of individual InAs quantum dots by scanning tunneling probe-assisted nanolithography*, Appl. Phys. Lett., 75, 3488 (1999).
- [51] S. Kohmoto, H. Nakamura, S. Nishikawa and K. Asakawa, *Three-dimensional site control of self-organized InAs quantum dots by in situ scanning tunneling probe-assisted nanolithography and molecular beam epitaxy*, J. Vac. Sci. Technol., B 20, 762 (2002).
- [52] H. Koyanagi, S. Hosaka and R. Imura, *Field evaporation of gold atoms onto a silicon dioxide film by using an atomic force microscope*, Appl. Phys. Lett., 67, 2609 (1995).
- [53] G. Kaminsky, *Noncontaminating Si-based shadow masks for MBE*, Journal of Vacuum Science Technology B: Microelectronics Processing and Phenomena, 3, 741 (1985).
- [54] A. Lambrecht, R. Kurbel and M. Agne, *Shadow mask MBE for the fabrication of lead chalcogenide buried heterostructure lasers*, Materials Science and Engineering: B, 21, 2–3 (1993).
- [55] S. Ohkouchi, Y. Nakamura, N. Ikeda, Y. Sugimoto and K. Asakawa, *In-situ mask designed for selective growth of InAs quantum dots in*

*narrow regions developed for molecular beam epitaxy system*, Review of Scientific Instruments, 78, 073908 (2007).

- [56] J. Köhler, M. Albrecht, C.R. Musil and E. Bucher, *Direct growth of nanostructures by deposition through an  $Si_3N_4$  shadow mask* Phys. E., 4 (1999).
- [57] T. Schallenberg, C. Schumacher, S. Gundel and W. Faschinger, *Shadow mask technology*, Thin Solid Films, 412, 24-29 (2002).
- [58] G.J. Burger, E.J.T. Smulder, J.W. Berenschot, T.S.J. Lammerink, J.H.J. Fluitman and S. Imai, *High Resolution Shadow Mask Patterning In Deep Holes And Its Application To An Electrical Wafer Feed-through*, Proceedings of the International Solid-State Sensors and Actuators Conference - Transducers '95 (1995).
- [59] H. Zhang, Y. Chen, G.Zhou, C. Tang and Z. Wang, *Wetting layer evolution and its temperature dependence during self assembly of InAs/GaAs quantum dots*, Nanoscale Res Lett., 7(1), 600 (2012).
- [60] M. Henini, *Molecular Beam Epitaxy: From Research to Mass Production*, Elsevier Inc., 788 (2018).
- [61] T. Chikyow and N. Koguchi, *MBE growth method for pyramid-shaped GaAs micro crystals on ZnSe(001) surface using Ga droplets*, Jpn. J. Appl. Phys., 29, L2093 (1990).
- [62] N. Koguchi and K. Ishige, *Growth of GaAs epitaxial microcrystals on an S-terminated GaAs substrate by successive irradiation of Ga and As molecular beams*, Jpn. J. Appl. Phys., 32, 2052 (1993).
- [63] J. Stangl, V. Holy and G. Bauer, *Structural properties of self-organized semiconductor nanostructures*, Rev. Mod. Phys. Sep., 76(3) (2004)

- [64] K. Yamada, N. Inoue, J. Osaka and K. Wada, *In-situ observation of molecular beam epitaxy of GaAs and AlGaAs under deficient As<sub>4</sub> flux by scanning reflection electron microscopy*, Appl. Phys. Lett., 55 (1989).
- [65] S. Adachi, *Properties of Aluminum Gallium Arsenide*, INSPEC (1993).
- [66] C. Deparis and J. Massies, *Surface stoichiometry variation associated with GaAs (001) reconstruction transition*, J. Cryst. Growth., 108, 157 (1991).
- [67] C. Heyn, A. Stemmann, A. Schramm, H. Welsch, W. Hansen and A. Nemcsics, *Regimes of GaAs quantum dot self-assembly by droplet epitaxy*, Phys. Rev. B, 76, 7 (2007).
- [68] C. Somaschini, S. Bietti, A. Trampert, U.Jahn, C. Hauswald, H. Riechert, S. Sanguinetti and L. Geelhaar, *Control over the Number Density and Diameter of GaAs Nanowires on Si (111) Mediated by Droplet Epitaxy*, Nano Lett., 13, 8 (2013).
- [69] L. Däweritz and R. Hey, *Reconstruction and defect structure of vicinal GaAs (001) and Al<sub>x</sub>Ga<sub>1-x</sub>As surfaces during MBE growth*, Surf. Sci., 236, 15 (1990).
- [70] J.F. Whitaker, *Optoelectronic applications of LTMBE III-V materials*, Mater. Sci. Eng. B, 61 (1993).
- [71] C. Sasaoka, Y. Kato and A. Usui, *Temperature programmed desorption study of GaAs(100)-c(4×4) and As<sub>4</sub> exposed (2×4) surfaces*, Surf. Sci., 265 (1992).
- [72] D.J. Chadi, *Atomic structure of GaAs (100)-(2×1) and (2×4) reconstructed surfaces*, J. Vac. Sci. Technol. A, 5, 834 (1987).

- [73] V. P. LaBella, M. R. Krause, Z. Ding and P. M. Thibado, *Arsenic-rich GaAs (001) surface structure*, Surface Science Reports, 60, 1-53 (2005).
- [74] A. Ohtake and N. Koguchi, *Two types of structures for the GaAs (001)-c(4×4) surface*, Appl. Phys. Lett., 83, 5193 (2003).
- [75] V.P. LaBella, H. Yang, D.W. Bullock, P.M. Thibado, P. Kratzer and M. Scheffler, *Atomic Structure of the GaAs (001)(2×4) Surface Resolved Using Scanning Tunneling Microscopy and First-Principles Theory*, Phys. Rev. Lett., 83, 2989 (1999).
- [76] A. Ohtake, P. Kocan, K. Seino and W. G Schmidt, *Ga-Rich Limit of Surface Reconstructions on GaAs (001): Atomic Structure of the (4 × 6) Phase*, Physical Review Letters, 93, 266101 (2005).
- [77] H. Asahi and Y. Horikoshi, *Molecular Beam Epitaxy: Materials and Applications for Electronics and Optoelectronics*, Wiley Series in Materials for Electronic Optoelectronic Applications, 512 (2019).
- [78] J. R. Arthur and J. J. LePore, *GaAs, GaP, and GaAs<sub>x</sub>P<sub>1-x</sub> Epitaxial Films Grown by Molecular Beam Deposition*, Journal of Vacuum Science and Technology, 6 (1969).
- [79] A. Cho, *Morphology of epitaxial growth of GaAs by a molecular beam method: The observation of surface structures*, Journal of Applied Physics, 41 (1970).
- [80] S. E. Aleksandrov, G. A. Gavrilov, A. A. Kapralov, G. Yu. Sotnikova, D. F. Chernykh, A. N. Alekseev, A. L. Dudin, I. V. Kogan and A. P. Shkurko, *Pyrometer unit for GaAs substrate temperature control in an MBE system*, Technical Physics, 49, 1 (2004).

- [81] W. Braun, *Applied RHEED. Reflection High-Energy Electron Diffraction During Crystal Growth*, Springer Tracts in Modern Physics, 154 (1999).
- [82] MBE-Komponenten GmbH, *3"-Wafer Heater DN150CF with Ta heater, linear motion only*, operating instructions (2014).
- [83] MBE-Komponenten GmbH, *3"-Manipulator with Tantalum wire heater (Ta) and custom mask shutter*, operating instructions (2014).
- [84] MBE-Komponenten GmbH, *UHV-System komplett Reuter PB*, UHV-System komplett, Reuter PB Freigabezeichnung (2014).
- [85] MBE-Komponenten GmbH, *Prep and Buffer-Kammer Reuter-PB*, Preparations- Buffer-Kammer Reuter-PB System, Freigabezeichnung (2014).
- [86] MBE-Komponenten GmbH, *MBE-Kammer Reuter Übersicht-01*, MBE-System Reuter PB Übersicht Freigabezeichnung (2014).
- [87] MBE-Komponenten GmbH, *Verdampfer-Positionen Materialien*, Einbaupositionen der Effusionszellen Materialzuordnungen, System Reuter PB (2014).
- [88] MBE-Komponenten GmbH, *Maskenhalter mit Waferadapter Funktionssweise*, 8330-WH3-MSK-ZB10 (2014).
- [89] LumaSense Technologies GmbH, *IMPAC Pyrometer IS 50-LO plus, IGA 50-LO plus*, Betriebsanleitung, Part No 3 857 047 - DE, Revision A (2014).
- [90] EpiMax, *The EpiSoft Control System: An Introductory Guide to EpiCAD*, EpiSoft Control System: Introductory Guide, EpiMax (2004).

- [91] MBE-Komponenten GmbH, *QCS100-3x10-22+2-22-KS-2105244 Quad Cluster Source with three 10-22 PBN crucible heater and one 2-22 PBN crucible heater Thermocouple Type C with integrated Cooling Shroud and Shutter*, operating instructions, QCS100-3x10-22+2-22-KS-2105244.doc (2014).
- [92] S. N. Magonov and M. -H. Whangbo, *Surface Analysis with STM and AFM. Experimental and Theoretical Aspects of Image Analysis*, VCH Verlagsgesellschaft mbH, 323 (1996).
- [93] W. R. Bowen and N. Hilal, *Atomic Force Microscopy in Process Engineering. Introduction to AFM for Improved Processes and Products*, Elsevier Ltd, 283 (2009).
- [94] R. A. Wilson and H. A. Bullen, *Basic Theory Atomic Force Microscopy*, Department of Chemistry, Northern Kentucky University, Highland Heights (2006)
- [95] A. Trapp, *Molecular beam epitaxy of quantum dots on misoriented GaAs(111)B by droplet epitaxy*, PhD thesis, Paderborn (2019)
- [96] W. Zhou and Z. L. Wang, *Scanning Microscopy for Nanotechnology. Techniques and Applications*, Springer, New York 522 (2006).
- [97] R. F. Egerton, *Physical Principles of Electron Microscopy. An Introduction to TEM, SEM, and AEM*, Springer, 202 (2005).
- [98] Raith GmbH, *Software Reference Manual Raith EO*, Raith GmbH (2011).
- [99] A. Ul-Hamid, *A Beginners' Guide to Scanning Electron Microscopy*, Springer International Publishing (2018).



- [100] W. Zhou, *Nanoimprint Lithography: An Enabling Process for Nanofabrication*, Springer-Verlag Berlin Heidelberg, 256 (2013).
- [101] G. Dhanaraj, K. Byrappa, V. Prasad and M. Dudley, *Springer Handbook of Crystal Growth*, Springer, 1816 (2010).
- [102] S. Franssila, *Introduction to Microfabrication*, John Wiley Sons, Ltd (2010).
- [103] S. Basu, *Crystalline Silicon - Properties and Uses*, InTechOpen (2011).
- [104] MBE-Komponenten GmbH, *Ta Maskenadapter für  $25 \times 25$  mm Maske Gegenstück zu Waferträger  $\frac{1}{4} \times 3$ "*, 8330-WH3-MSK-ZB01(2014).
- [105] Ma. J. Archer and F. S. Ligler, *Fabrication and Characterization of Silicon Micro-Funnels and Tapered Micro-Channels for Stochastic Sensing Applications*, *Sensors*, 8 (2008).
- [106] C. R. Helms and B. E. Deal, *The Physics and Chemistry of  $\text{SiO}_2$  and the  $\text{Si-SiO}_2$* , Springer-Verlag US, Interface 2 (1993).
- [107] K. A. Reinhardt and R. F. Reidy, *Handbook of Cleaning in Semiconductor Manufacturing: Fundamental and Applications*, Scrivener Publishing LLC, (2010).
- [108] V. Zolatanosha and D. Reuter, *Robust  $\text{Si}_3\text{N}_4$  masks for 100 nm selective area epitaxy of GaAs-based nanostructures*, *Microelectronic Engineering*, 180 (2017).
- [109] E. J. Hierra and J. A. Salazar, *Silicon Nitride: Synthesis, Properties and Applications*, *Chemical Engineering Methods and Technology: Materials Science and Technologies*, Nova Science Publishers (2012).

- [110] B. Zheng, C. Zhou, Q. Wang, Y. Chen and W. Xue, *Deposition of Low Stress Silicon Nitride Thin Film and Its Application in Surface Micromachining Device Structures*, Advances in Materials Science and Engineering (2013)
- [111] A. E. Kaloyeros, F. A. Jove, J. Goff and B. Arkles, *Review—Silicon Nitride and Silicon Nitride-Rich Thin Film Technologies: Trends in Deposition Techniques and Related Applications*, ECS Journal of Solid State Science and Technology, 6, 10 (2010).
- [112] M. Köhler, *Etching in Microsystem Technology*, Wiley-VCH (1999).
- [113] M. J. Madou, *Fundamentals of Microfabrication*, Taylor Francis, 589 (1997).
- [114] A. Prakash, J. G. Jency and M. C. Mathew, *A Review of various Wet Etching Techniques used in Micro Fabrication for Real Estate Consumption*, International Journal of Computer Applications, 0975–8887 (2013).
- [115] D. House and D. Li, *Anisotropic Etching*, Encyclopedia of Microfluidics and Nanofluidics, Springer (2008).
- [116] O. Powell and H. B. Harrison, *Anisotropic etching of {100} and {110} planes in (100) silicon*, Journal of Micromechanics and Microengineering, 11, 3 (2001).
- [117] *Anisotropic Silicon Etch Using KOH*, INRF application note, Process name: KOH01.
- [118] P. A. Alvi, V. S. Meel, K. Sarita, J. Akhtar, K. M. LAal, A. Azam and S. A. H. Naqvi, *A study on anisotropic etching of (100) Silicon in aqueous KOH solution*, Int. J. Chem. Sci., 6, 3 (2008).

- [119] K. R. Williams, K. Gupta and M. Wasilik, *Etch Rates for Micromachining Processing—Part II*, Journal of Microelectromechanical systems, 12, 6 (2003).
- [120] All resist, *Positive Photoresists AR-P 3500 / 3500 T*, product information (2014).
- [121] All resist, *Positive PMMA E-Beam Resists AR-P 630 – 670 series*, product information (2014).
- [122] J. W. Orton and T. Foxon, *Molecular Beam Epitaxy: A Short History*, Oxford University Press (2015).
- [123] M. Tanaka, T. Suzuki and T. Nishinaga, *Surface diffusion of Al and Ga atoms on GaAs (001) and (111) B vicinal surfaces in molecular beam epitaxy*, Journal of Crystal Growth, 111 (1991).
- [124] N. Chand, *MBE growth of high-quality GaAs*, Journal of Crystal Growth, 97, 2 (1989).
- [125] M. J. Manfra, *Molecular Beam Epitaxy of Ultra-High Quality Al-GaAs/GaAs Heterostructures: Enabling Physics in Low-Dimensional Electronic Systems*, Purdue University, West Lafayette IN 47907 (2013).
- [126] M. Shinohara, T. Ito, K. Wada and Y. Imamura, *Electrical Properties of Oval Defects in GaAs Grown by MBE*, Japanese Journal of Applied Physics, 23, 2, 6 (1984).
- [127] J. Tommila, C. Strelow, A. Schramm, T. V. Hakkarainen, M. Dumitrescu, T. Kipp and M. Guina, *The influence of temperature on the photoluminescence properties of single InAs quantum dots grown on patterned GaAs*, Nanoscale Res Lett., 7, 1, 313 (2012).

- [128] L. Chu, M. Arzberger, G. Böhm, and G. Abstreiter, *Influence of growth conditions on the photoluminescence of self-assembled InAs/GaAs quantum dots*, Journal of Applied Physics 85, 2355 (1999).
- [129] A. F. Pun, X. Wang, S. M. Durbin and J. P. Zheng, *Reduction of thermal oxide desorption etching on gallium arsenide*, Thin Solid Films, 515, 10 (2007).
- [130] O. A. Ageev, M. S. Solodovnik, S. V. Balakirev, I. A. Mikhaylin, M. M. Eremenko, *Effect of GaAs native oxide upon the surface morphology during GaAs MBE growth*, Journal of Physics: Conference Series, 741 (2016).
- [131] Y. Asaoka, T. Kanebishi, N. Sano and T. Kaneko, *In-situ control of the desorption process of GaAs surface native oxide by direct Ga beam irradiation*, International Conference on Molecular Beam Epitaxy (2002).
- [132] Y. Asaoka, *Desorption process of GaAs surface native oxide controlled by direct Ga-beam irradiation*, Journal of Crystal Growth, 251, 1 (2003).
- [133] V. Zolatanosha and D. Reuter, *Site-controlled droplet epitaxy of GaAs quantum dots by deposition through shadow masks*, Journal of Vacuum Science Technology B 36, (2018).
- [134] Ch. Heyn and D. E. Jesson, *Congruent evaporation temperature of molecular beam epitaxy grown GaAs (001) determined by local droplet etching*, Appl. Phys. Lett., 107 (2015.)
- [135] S.-K. Ha, J. D. Song, J. Y. Lim, S. Bounouar, F. Donatini, L. S. Dang, J. P. Poizat, J. S. Kim, W. J. Choi, I. K. Han and J. I. Lee, *Growth*

- and characterization of low density droplet GaAs quantum dots for single photon sources*, Proceedings, Quantum Sensing and Nanophotonic Devices VIII, 7945 (2011).
- [136] Ch. Heyn, A. Stemann, A. Schramm, H. Welsch, and W. Hansen, *Faceting during GaAs quantum dot self-assembly by droplet epitaxy*, Appl. Phys. Lett. 90, 203105 (2007).
- [137] A. Kley, P. Ruggerone and M. Scheffler, *Novel Diffusion Mechanism on the GaAs (001) Surface: The Role of Adatom-Dimer Interaction*, Physical Review Letters, 79, 26 (1997).
- [138] A. Szerling, K. Kosiel, A. Wójcik-Jedlińska and M. Pluska, *Properties and origin of oval defects in epitaxial structures grown by molecular beam epitaxy*, Optica Applicata, 35, 4 (2005).
- [139] K. Ohta, T. Kojima and T. Nakagawa, *Anisotropic surface migration of Ga atoms on GaAs (001)*, Journal of Crystal Growth, 95, 1–4 (1989).
- [140] MBE-Komponenten GmbH, *MBE-Kammer Reuter Schnitte-01*, MBE-System Reuter PB Schnittansichten Freigabezeichnung, (2014).
- [141] MBE-Komponenten GmbH, *MBE-Kammer Reuter Schnitte-01*, MBE-System Reuter PB Schnittansichten Freigabezeichnung (2014).
- [142] W. Ostwald, *Über die vermeintliche isometric des roten und gelben quecksilberxyds und die oberflächenspannung fester körper*, Zeitschrift für Physikalische Chemie, Stoechiom. Verwandtschaftsl. 34, 495 (1900).

# Appendix A: Wafer datasheets



## CrysTec

KRISTALLTECHNOLOGIE

CrysTec GmbH • Köpenicker Str. 325 • D - 12555 Berlin

**Universität Paderborn**  
**Department Physik,**  
**AG Optoelektronische Materialien und Bauelemente**  
 Wartburger Str. 100  
 33098 Paderborn

Mrs. Viktoryia Zolatanosha

Email: vikzolat@mail.uni-paderborn.de

**Pos. 01 Silicon (Cz) with nitride**

orientation:	<b>(1 0 0)</b>
tolerance:	< 0,5°
diameter:	100 mm
thickness:	<b>1000 µm</b>
tolerance:	+/- 50 µm
Flat:	Semi Standard
type and dope:	p – type, Boron
resistivity:	> 1 Ohmcm
surface:	<b>double side polished</b>
<b>thermal oxide thickness</b>	<b>10 nm</b>
<b>nitride thickness</b>	<b>100 nm</b>

**Pos. 04: Dicing of Silicon (Pos. 01 - 03) with diameter 100 mm into formats with a size of 24 mm x 24 mm (yield: max. 6 pieces)**

The wafers are fixed at wafer foil for dicing. The surface is covered with an optical lacquer. Lacquer can easily be removed by using acetone or ethanol without leaving residues.

Figure 5.21: Datasheet of *Si*-wafers supplied for the mask fabrication by *CrysTec GmbH*



WAFER TECHNOLOGY LTD.

## Certificate of Conformance: Single Crystal Materials

Customer	UNIVERSITY OF PADERBORN	Ingot/lot no.	WV 23757/Un	
Customer specification	QT102542	Quantity	30 Slices	
Customer order number	EC/10302070000/13/15/7	Total weight	462.4g	
WT order number	WT/ 19459			
	<b>Specified</b>		<b>Supplied</b>	
Material/Growth method	GaAs , VGF		GaAs , VGF	
Dopant	Undoped		Undoped	
Orientation	(100) ± 0.1°		(100) ± 0.09°	
Diameter/dimensions (mm)	76.2 ± 0.4		76.0	
Flat Option (EJ/SEMI)	EJ		EJ	
Major Flat Length(mm)	22 ± 2 on (0-1-1)		21.7 on (0-1-1)	
Minor Flat Length(mm)	11 ± 1 on (0-11)		11.7 on (0-11)	
Surface Finish/Form	One Side Polished		One Side Polished	
Thickness (microns)	625 ± 25		632 - 645	
Bow (microns)	Not Specified		Not Specified	
Warp (microns)	Not Specified		Not Specified	
TTV (microns)	Not Specified		Not Specified	
	<b>Specified</b>		<b>Seed End</b>	<b>Tail End</b>
Resistivity (Ωcm)	>=1E7		2.17E+08	1.00E+08
Hall mobility (cm <sup>2</sup> V <sup>-1</sup> s <sup>-1</sup> )	>=5000		6130	5220
Carrier concentration (cm <sup>-3</sup> )	semi insulating		4.70E+06	1.20E+07
Average EPD (cm <sup>-2</sup> )	<=5000		452	644
Additional Information				
We hereby certify that the above material has been fully tested and is within quoted specification				
Signed by:	Production	<u>B.J. Water</u>		
	Quality Assurance	<u>RMcCubra</u>		
	Date	<u>10/3/15</u>		
PC F 0003 Issue 2				
Independently Approved by BSi to ISO 9001				
Manufactured under a Quality Assurance System				
Certificate Number: FM26963				

34 Maryland Road, Tongwell, Milton Keynes, Bucks MK15 8HJ, England, U.K  
 Tel: +44 (0)1908 210444 Fax: +44 (0)1908 210443  
 www.wafertech.co.uk

Figure 5.22: Datasheet of GaAs (100) wafers supplied for the sample production by *Wafer Technology Ltd.*

## Appendix B: Mathematical representation of Si (100) etching

As mentioned above in Section 4.2, the anisotropic etching is controlled by crystal planes. Etching rate of *Si*-wafer in a (100) direction is significantly faster than in a (111) direction[113]-[116]. Therefore, the shape of the structure is initially determined by fast etching crystal planes, e. g., in case of a square opening in the hard mask, the resulting profile is a square groove. Schematic representation of the etched profile for the square opening in *Si*-wafer (100) is presented in Figures 5.23 (a) and (b).

Due to a good control of etching parameters during KOH etching of *Si* (100), final profiles of etched in *Si*-wafer structures can be predicted with high accuracy concerning an initial hard mask design. In other words, the size of the opening in *Si*-wafer  $W_2$  can be calculated using the following relation (4) if the size of an initial hard mask opening  $W_1$  and a total depth of etching ( $d$ ) are known respectively:

$$W_2 = W_1 - 2 \times \frac{d}{\tan 54.74^\circ} \quad (4)$$



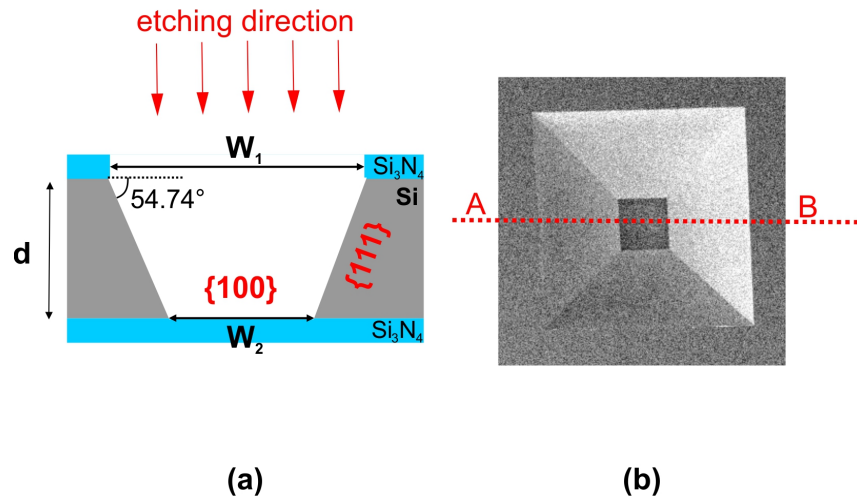


Figure 5.23: Schematic representation of the etched profile of a square-shaped opening in the mask geometry in  $Si$  (100): a sketch of a cross-section of the square groove etched in  $Si$  (100) (a) and a SEM image of the square groove itself (b), respectively.

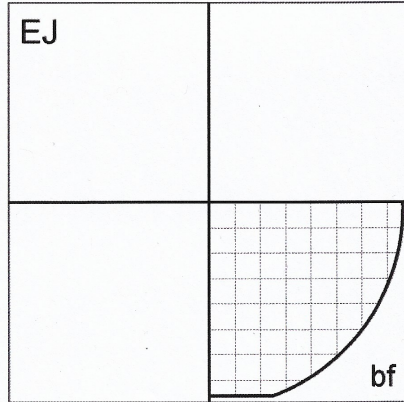
Thus, if a depth of the etching is  $950 \mu\text{m}$ <sup>15</sup> and a size of a single active window has to be  $200 \times 200 \mu\text{m}^2$ , the initial opening in hard mask is calculated to be  $W_1 = 200 + 2 \times \frac{950}{1.41} = 1550 [\mu\text{m}]$ .

<sup>15</sup>a total  $Si$  thickness in case of the etching through the whole wafer and with a taking into account tolerance

## **Appendix C: List of Samples. MBE growth recipes.**

The growth recipes corresponding to samples used to acquire results presented in this thesis are given in the following pages. Growth protocols are generated semi-automatically. They contain important information regarding to a sample growth, such as substrate temperatures, growth pressures, deposition rates, layer sequences and layer thicknesses. Changes in the substrate and cell temperatures, as well as growth pauses between the growth steps, are omitted. Important parameters for the SADE process such as a mask number, pre-coverage and coverage thicknesses were manually added to the ‘Comment’ box if it was necessary.

Note: Due to a specificity of the growth procedure employing shadow masks, samples have been grown in two or three stages depending on growth purposes. Accordingly, two growth-protocols correspond to each sample grown by SADE.

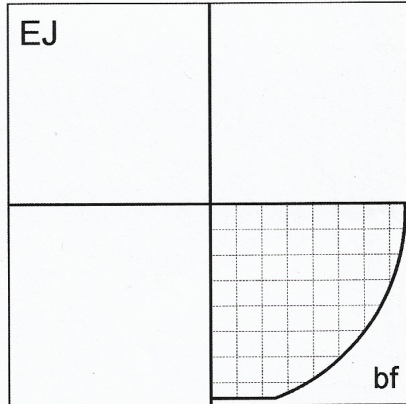


Sample: **A0176\_1**  
 Material: GaAs  
 Orientation: (100)  
 Wafer: WV/23757/Un/19  
 Rotation: 0  
 Pressure (mBar):  $4.6 \times 10^{-8}$   
 Date: 03.11.2015  
 File: a0176\_1.asl

		300K	77K	4.2K	1K
dark	$\mu$ [cm <sup>2</sup> / Vs]				
	n [cm <sup>-2</sup> ]				
illum	$\mu$ [cm <sup>2</sup> / Vs]				
	n [cm <sup>-2</sup> ]				

Layer	Loop	T [°C]	Dur. [s]	Thickn. [nm]	growth rate
GaAs		555.0	504.8	100	GaAs 0.198 nm/s
GaAs		180.0	1.3	0.3	GaAs 0.231 nm/s
					Comment T(pyro)=590°C As=30%  Ga terminated layer: Ts=180°C As=0% Pmbe=4.19E-9
					(Grown by V. Zolatanosha)



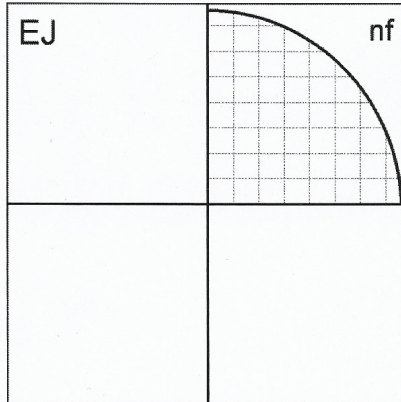
Sample: **A0176\_2**  
 Material: GaAs  
 Orientation: (100)  
 Wafer: WV/23757/Un/19  
 Rotation: 0  
 Pressure (mBar):  $2.66 \times 10^{-8}$   
 Date: 03.11.2015  
 File: A0176\_2.asl

		300K	77K	4.2K	1K
dark	$\mu$ [ $\text{cm}^2 / \text{Vs}$ ]				
	$n$ [ $\text{cm}^{-2}$ ]				
illum	$\mu$ [ $\text{cm}^2 / \text{Vs}$ ]				
	$n$ [ $\text{cm}^{-2}$ ]				

Layer	Loop	T [°C]	Dur. [s]	Thickn. [nm]	growth rate
GaAs		260.0	1262.0	250	GaAs 0.198 nm/s
GaAs		180.0	6.3	1.3	GaAs 0.206 nm/s
					<i>Comment</i> Ttc=260°C As=30%  Ga deposition: Ts=180°C As=0% Pmbe=4.9E-9  Crystallization (after 3 min): As=50% Pmbe=1.59E-8  (Grown by V. Zolatanosha)

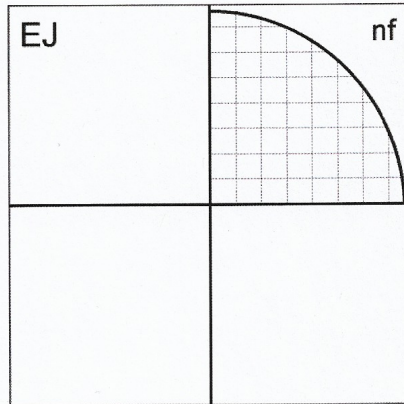




**Sample: A0261\_2**  
 Material: GaAs  
 Orientation: (100)  
 Wafer: WV/23856/Un/19  
 Rotation: 0  
 Pressure (mBar): 1.65 x 10<sup>-9</sup>  
 Date: 13.04.2016  
 File: a0261\_2.asl

		300K	77K	4.2K	1K
dark	$\mu$ [cm <sup>2</sup> / Vs]				
	n [cm <sup>-2</sup> ]				
illum	$\mu$ [cm <sup>2</sup> / Vs]				
	n [cm <sup>-2</sup> ]				

Layer	Loop	T [°C]	Dur. [s]	Thickn. [nm]	growth rate
GaAs		250.0	131.5	1.3	GaAs 0.01 nm/s
					Comment
					(Grown by V. Zolatanosha)



**Sample:** A0266\_1  
**Material:** GaAs  
**Orientation:** (100)  
**Wafer:** WV/23856/Un/17  
**Rotation:** 0  
**Pressure (mBar):**  $3.55 \times 10^{-8}$   
**Date:** 19.04.2016  
**File:** a0266\_1.asl

		300K	77K	4.2K	1K
dark	$\mu$ [cm <sup>2</sup> / Vs]				
	n [cm <sup>-2</sup> ]				
illum	$\mu$ [cm <sup>2</sup> / Vs]				
	n [cm <sup>-2</sup> ]				

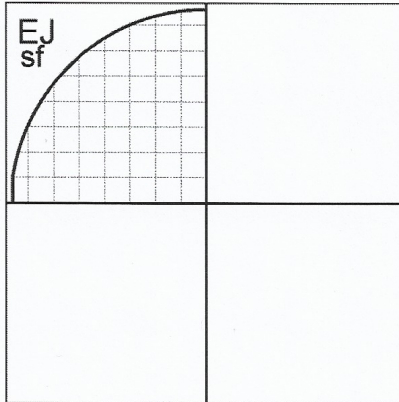
Layer	Loop	T [°C]	Dur. [s]	Thickn. [nm]	growth rate
GaAs		550.0	506.8	100	GaAs 0.197 nm/s
GaAs		250.0	16.7	0.3	GaAs 0.018 nm/s
					<i>Comment</i> Tpyro=595°C As=40%
(Grown by V. Zolatanosha)					









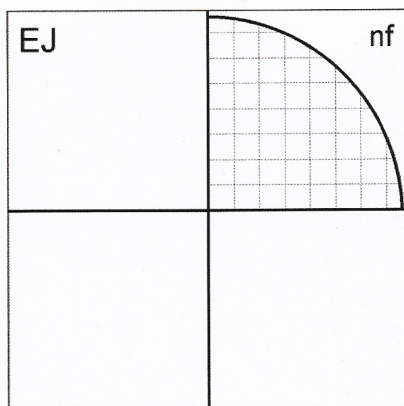


**Sample:** A0303\_1  
**Material:** GaAs  
**Orientation:** (100)  
**Wafer:** WV/23856/Un/30  
**Rotation:** 0  
**Pressure (mBar):**  $4.52 \times 10^{-8}$   
**Date:** 28.07.2016  
**File:** a0303\_1.asi

		300K	77K	4.2K	1K
dark	$\mu$ [ $\text{cm}^2 / \text{Vs}$ ]				
	$n$ [ $\text{cm}^{-2}$ ]				
illum	$\mu$ [ $\text{cm}^2 / \text{Vs}$ ]				
	$n$ [ $\text{cm}^{-2}$ ]				

Layer	Loop	T [ $^{\circ}\text{C}$ ]	Dur. [s]	Thickn. [nm]	growth rate
GaAs		595.0	505.4	100	GaAs 0.198 nm/s
GaAs		250.0	34.6	0.3	GaAs 0.009 nm/s
					Comment
					mask M4_2
					(Grown by V. Zolatanosha)

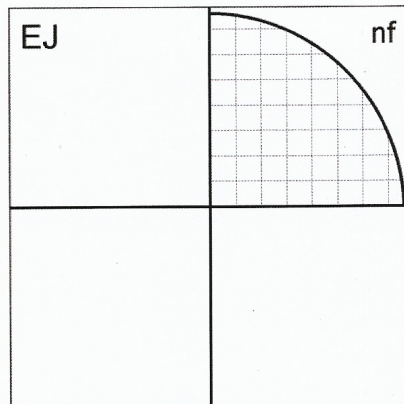




Sample: **A0308\_1**  
 Material: GaAs  
 Orientation: (100)  
 Wafer: WV/23856/Un/33  
 Rotation: 0  
 Pressure (mBar):  $5.09 \times 10^{-8}$   
 Date: 08.08.2016  
 File: a0308\_1.asl

		300K	77K	4.2K	1K
dark	$\mu$ [cm <sup>2</sup> / Vs]				
	n [cm <sup>-2</sup> ]				
illum	$\mu$ [cm <sup>2</sup> / Vs]				
	n [cm <sup>-2</sup> ]				

Layer	Loop	T [°C]	Dur. [s]	Thickn. [nm]	growth rate
GaAs		590.0	505.4	100	GaAs 0.198 nm/s
GaAs		250.0	52.9	0.3	GaAs 0.006 nm/s
					Comment mask M4_2 Tpyro=595°C
					(Grown by V. Zolatanosha)

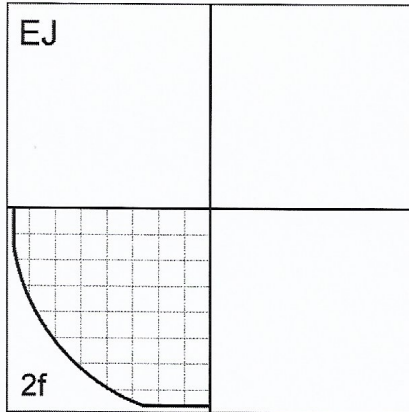


**Sample:** **A0308\_2**  
**Material:** GaAs  
**Orientation:** (100)  
**Wafer:** WV/23856/Un/33  
**Rotation:** 0  
**Pressure (mBar):**  $6.75 \times 10^{-10}$   
**Date:** 08.08.2016  
**File:** a0308\_2.asl

		300K	77K	4.2K	1K
dark	$\mu$ [cm <sup>2</sup> / Vs]				
	n [cm <sup>-2</sup> ]				
illum	$\mu$ [cm <sup>2</sup> / Vs]				
	n [cm <sup>-2</sup> ]				

Layer	Loop	T [°C]	Dur. [s]	Thickn. [nm]	growth rate
GaAs		100.0	493.9	2.8	GaAs 0.006 nm/s
					<b>Comment</b> mask M4_2 F=10 ML
					(Grown by V. Zolatanosha)



**Sample:** A0453\_1  
**Material:** GaAs  
**Orientation:** (100)  
**Wafer:** WV23966/Un/25  
**Rotation:** 0  
**Pressure (mBar):**  $3.54 \times 10^{-8}$   
**Date:** 21.04.2017  
**File:** a0453\_1.asl

**300K                      77K                      4.2K                      1K**

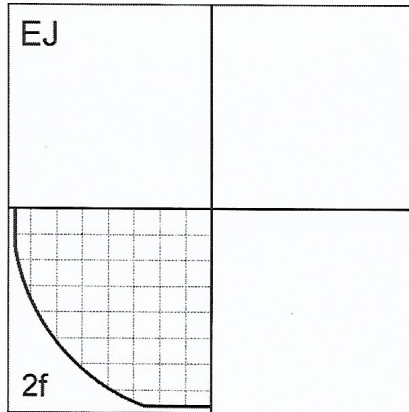
		300K	77K	4.2K	1K
dark	$\mu$ [cm <sup>2</sup> / Vs]				
	n [cm <sup>-2</sup> ]				
illum	$\mu$ [cm <sup>2</sup> / Vs]				
	n [cm <sup>-2</sup> ]				

Layer	Loop	T [°C]	Dur. [s]	Thickn. [nm]	growth rate
GaAs		590.0	519.3	100	GaAs 0.193 nm/s
Ga		350.0	15.3	0.28	GaAs 0.018 nm/s
					<b>Comment</b> mask M15_2 T <sub>pyro</sub> =595°C As=25%=2.02E-5 mbar 1ML at T15Cl_Ga=900°C (Grown by V. Zolatanosha)









Sample: **a0460\_2**  
 Material: GaAs  
 Orientation: (100)  
 Wafer: WV/23966/Un/26  
 Rotation: 0  
 Pressure (mBar):  $1.11 \times 10^{-9}$   
 Date: 27.04.2017  
 File: a0460\_2.asl

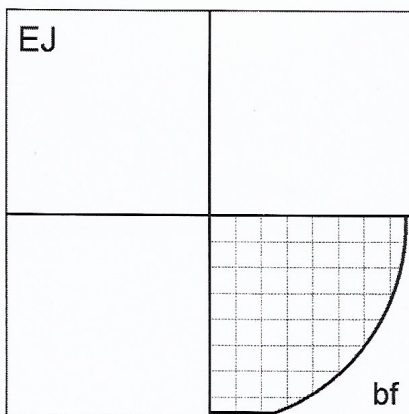
		300K	77K	4.2K	1K
dark	$\mu$ [cm <sup>2</sup> / Vs]				
	n [cm <sup>-2</sup> ]				
illum	$\mu$ [cm <sup>2</sup> / Vs]				
	n [cm <sup>-2</sup> ]				

Layer	Loop	T [°C]	Dur. [s]	Thickn. [nm]	growth rate
Ga		100.0	14.9	1.3	GaAs 0.087 nm/s
					<i>Comment</i> mask M15_2  25 min for stabilisation at opened 18Cl_Si (1200°C) switched off Cryo pump  (Grown by V. Zolatanosha)







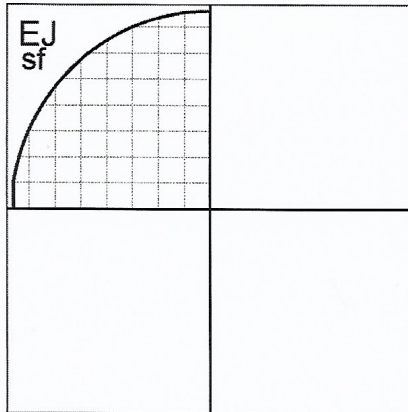


**Sample: A0499\_2**  
**Material: GaAs**  
**Orientation: (100)**  
**Wafer: WV/23966/Un/36**  
**Rotation: 0**  
**Pressure (mBar):  $1.21 \times 10^{-9}$**   
**Date: 01.06.2017**  
**File: a0499\_2.asl**

**300K                      77K                      4.2K                      1K**

dark	$\mu$ [cm <sup>2</sup> / Vs]				
	$n$ [cm <sup>-2</sup> ]				
illum	$\mu$ [cm <sup>2</sup> / Vs]				
	$n$ [cm <sup>-2</sup> ]				

Layer	Loop	T [°C]	Dur. [s]	Thickn. [nm]	growth rate
Ga		100.0	105.6	11.2	GaAs 0.106 nm/s
					<i>Comment</i> mask M15_2  @ deposition 40 ML; cryo pump off  @ annealing Tsub=400°C for 5 min  (Grown by V. Zolatanosha)



**Sample: A0504\_1**  
**Material: GaAs**  
**Orientation: (100)**  
**Wafer: WV/23966/Un/37**  
**Rotation: 0**  
**Pressure (mBar):  $3.87 \times 10^{-8}$**   
**Date: 08.06.2017**  
**File: a0504\_1.asl**

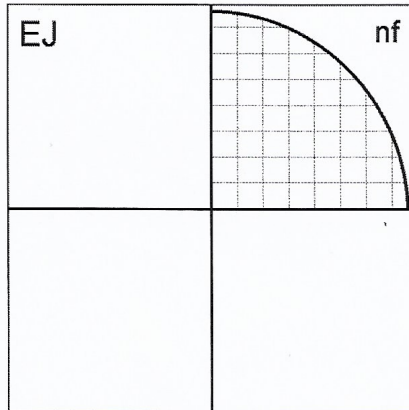
		300K	77K	4.2K	1K
dark	$\mu$ [cm <sup>2</sup> / Vs]				
	n [cm <sup>-2</sup> ]				
illum	$\mu$ [cm <sup>2</sup> / Vs]				
	n [cm <sup>-2</sup> ]				

Layer	Loop	T [°C]	Dur. [s]	Thickn. [nm]	growth rate
GaAs		605.0	256.4	50	GaAs 0.192 nm/s
Ga <sub>70.6</sub> Al <sub>29.4</sub> As		605.0	361.9	100	AlAs 0.081 nm/s
GaAs		605.0	2.6	0.5	GaAs 0.02 nm/s
Ga		350.0	14.3	0.28	
					Comment mask M15_2  Tpyro=590°C As=40%=2.00E-5
					(Grown by V. Zolatanosha)







Sample: **A0505\_1**  
 Material: GaAs  
 Orientation: (100)  
 Wafer: WV/23966/Un/39  
 Rotation: 0  
 Pressure (mBar):  $3.43 \times 10^{-8}$   
 Date: 08.06.2017  
 File: a0505\_1.asl

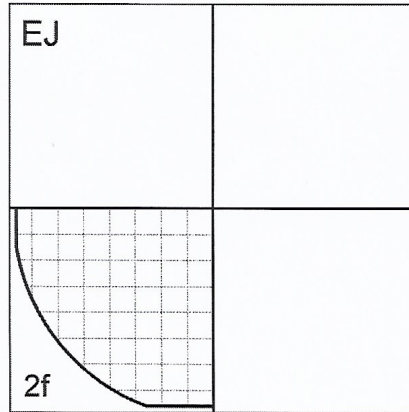
		300K	77K	4.2K	1K
dark	$\mu$ [cm <sup>2</sup> / Vs]				
	n [cm <sup>-2</sup> ]				
illum	$\mu$ [cm <sup>2</sup> / Vs]				
	n [cm <sup>-2</sup> ]				

Layer	Loop	T [°C]	Dur. [s]	Thickn. [nm]	growth rate
GaAs		610.0	256.4	50	GaAs 0.192 nm/s
Ga <sub>70.6</sub> Al <sub>26.4</sub> As		610.0	361.9	100	AlAs 0.081 nm/s
GaAs		610.0	2.6	0.5	GaAs 0.02 nm/s
Ga		350.0	14.3	0.28	
					Comment mask M15_2 Tpyro=557°C(587°C) As=40%=2.0E-5 mbar
					(Grown by V. Zolatanosha)







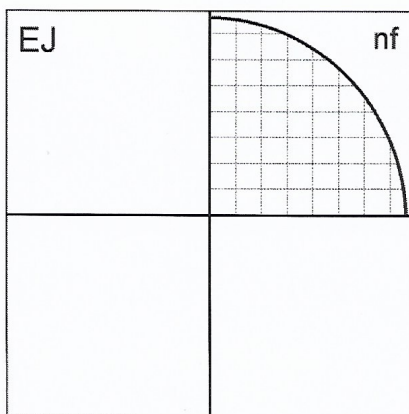
**Sample:** A0519\_2  
**Material:** GaAs  
**Orientation:** (100)  
**Wafer:** WV/23966/Un/42  
**Rotation:** 0  
**Pressure (mBar):**  $1.09 \times 10^{-9}$   
**Date:** 06.07.2017  
**File:** a0519\_2.asl

		300K	77K	4.2K	1K
dark	$\mu$ [cm <sup>2</sup> / Vs]				
	n [cm <sup>-2</sup> ]				
illum	$\mu$ [cm <sup>2</sup> / Vs]				
	n [cm <sup>-2</sup> ]				

Layer	Loop	T [°C]	Dur. [s]	Thickn. [nm]	growth rate
Ga		100.0	112.7	11.2	GaAs 0.099 nm/s
					Comment mask M15_2  @ Ga deposition cryo pump_off 40 ML of Ga  @ annealing Tsub=400°C for 5 min  (Grown by V. Zolatanosha)



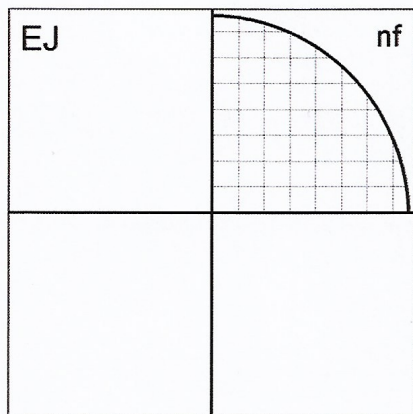


**Sample:** A0520\_2  
**Material:** GaAs  
**Orientation:** (100)  
**Wafer:** WV/23966/Un/41  
**Rotation:** 0  
**Pressure (mBar):**  $9.55 \times 10^{-10}$   
**Date:** 06.07.2017  
**File:** a0520\_2.asl

		300K	77K	4.2K	1K
dark	$\mu$ [cm <sup>2</sup> / Vs]				
	n [cm <sup>-2</sup> ]				
illum	$\mu$ [cm <sup>2</sup> / Vs]				
	n [cm <sup>-2</sup> ]				

Layer	Loop	T [°C]	Dur. [s]	Thickn. [nm]	growth rate
Ga		100.0	112.7	11.2	GaAs 0.099 nm/s
					Comment mask M15_2 @ Ga deposition cryo pump_off 40ML of Ga @ annealing Tsub=400°C for 5 min (Grown by V. Zolatanosha)





Sample: **A0522\_2**  
 Material: GaAs  
 Orientation: (100)  
 Wafer: WV/23966/Un/43  
 Rotation: 0  
 Pressure (mBar):  $8.91 \times 10^{-10}$   
 Date: 11.07.2017  
 File: a0522\_2.asl

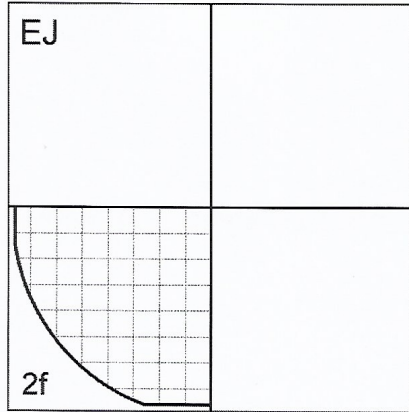
300K                      77K                      4.2K                      1K

dark	$\mu$ [cm <sup>2</sup> / Vs]				
	n [cm <sup>-2</sup> ]				
illum	$\mu$ [cm <sup>2</sup> / Vs]				
	n [cm <sup>-2</sup> ]				

Layer	Loop	T [°C]	Dur. [s]	Thickn. [nm]	growth rate
Ga		100.0	112.7	11.2	GaAs 0.099 nm/s
					Comment mask M15_2  @ Ga deposition 40 ML without cryo pump  @ annealing 400 °C for 5 min  (Grown by V. Zolatanosha)



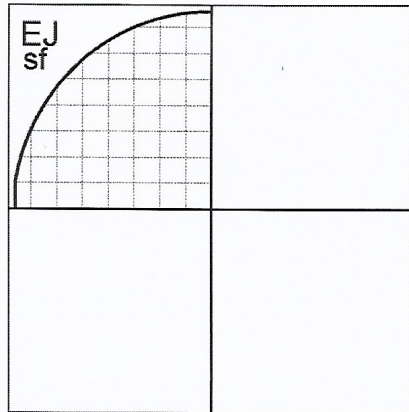




Sample: **A0527\_2**  
 Material: GaAs  
 Orientation: (100)  
 Wafer: WV/23966/Un/45  
 Rotation: 0  
 Pressure (mBar):  $9.34 \times 10^{-10}$   
 Date: 24.07.2017  
 File: a0527\_2.asl

		300K	77K	4.2K	1K
dark	$\mu$ [cm <sup>2</sup> / Vs]				
	$n$ [cm <sup>-2</sup> ]				
illum	$\mu$ [cm <sup>2</sup> / Vs]				
	$n$ [cm <sup>-2</sup> ]				

Layer	Loop	T [°C]	Dur. [s]	Thickn. [nm]	growth rate
Ga		100.0	98.6	9.8	GaAs 0.099 nm/s
					<i>Comment</i> mask M15_2  @ Ga deposition cryo pump_off 35ML  @ annealing 400°C for 5 min  (Grown by V. Zolatanosha)



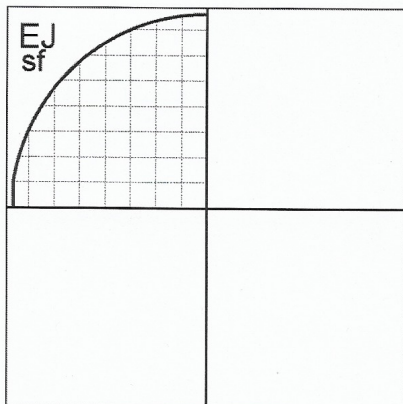
Sample: **A0528\_1**  
 Material: GaAs  
 Orientation: (100)  
 Wafer: WV/23966/Un/45  
 Rotation: 0  
 Pressure (mBar):  $2.70 \times 10^{-8}$   
 Date: 24.07.2017  
 File: a0528\_1.asl

**300K                      77K                      4.2K                      1K**

dark	$\mu$ [cm <sup>2</sup> / Vs]				
	n [cm <sup>-2</sup> ]				
illum	$\mu$ [cm <sup>2</sup> / Vs]				
	n [cm <sup>-2</sup> ]				

Layer	Loop	T [°C]	Dur. [s]	Thickn. [nm]	growth rate
GaAs		620.0	273.5	50	GaAs 0.185 nm/s
Ga <sub>88.5</sub> Al <sub>11.5</sub> As		620.0	374.5	100	AlAs 0.084 nm/s
GaAs		620.0	2.7	0.5	GaAs 0.02 nm/s
Ga		350.0	14.3	0.28	
					Comment mask M15_2  Tpyro=560°C(590°C) As=50%=1.96E-5  1.0 ML of Ga  (Grown by V. Zolatanosha)



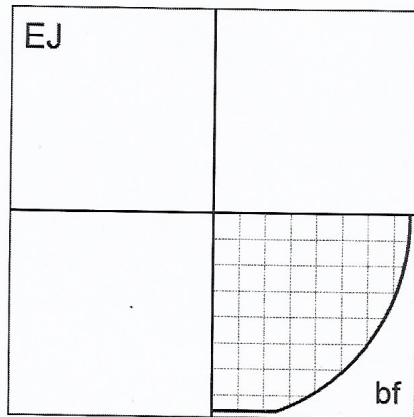


**Sample: A0539\_1**  
**Material: GaAs**  
**Orientation: (100)**  
**Wafer: WV/23966/Un/46**  
**Rotation: 0**  
**Pressure (mBar): 3.15 x 10<sup>-8</sup>**  
**Date: 01.08.2017**  
**File: a0539\_1.asl**

		300K	77K	4.2K	1K
dark	$\mu$ [cm <sup>2</sup> / Vs]				
	n [cm <sup>-2</sup> ]				
illum	$\mu$ [cm <sup>2</sup> / Vs]				
	n [cm <sup>-2</sup> ]				

Layer	Loop	T [°C]	Dur. [s]	Thickn. [nm]	growth rate
GaAs		620.0	279.3	50	GaAs 0.179 nm/s
Ga <sub>68</sub> Al <sub>32</sub> As		620.0	380.0	100	AlAs 0.084 nm/s
GaAs		620.0	2.8	0.5	GaAs 0.02 nm/s
Ga		350.0	17.4	0.34	
					<b>Comment</b> mask M15_2 Tpyro=556°C(586°C) As=50%=1.98E-5 1.2 ML of Ga  (Grown by V. Zolatanosha)



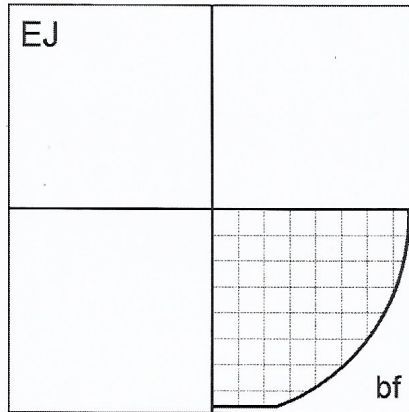


Sample: **A0540\_1**  
 Material: GaAs  
 Orientation: (100)  
 Wafer: WV/23966/Un/46  
 Rotation: 0  
 Pressure (mBar):  $2.88 \times 10^{-8}$   
 Date: 01.08.2017  
 File: a0540\_1.asi

		300K	77K	4.2K	1K
dark	$\mu$ [cm <sup>2</sup> / Vs]				
	n [cm <sup>-2</sup> ]				
illum	$\mu$ [cm <sup>2</sup> / Vs]				
	n [cm <sup>-2</sup> ]				

Layer	Loop	T [°C]	Dur. [s]	Thickn. [nm]	growth rate
GaAs		620.0	279.3	50	GaAs 0.179 nm/s
Ga <sub>88.0</sub> Al <sub>12.0</sub> As		620.0	380.0	100	AlAs 0.084 nm/s
GaAs		620.0	2.8	0.5	GaAs 0.02 nm/s
Ga		350.0	17.4	0.34	
					Comment mask M15_2 Tpyro=565°C(595°C) As=50%=1.98E-5 1.2 ML of Ga (Grown by V. Zolatanosha)

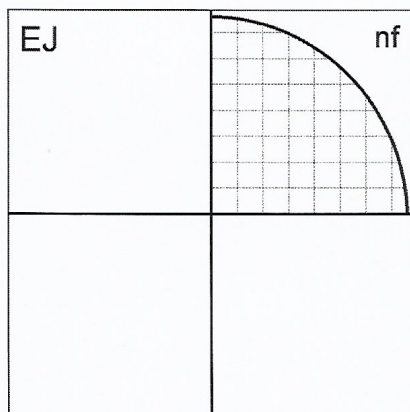


Sample: **A0540\_2**  
 Material: GaAs  
 Orientation: (100)  
 Wafer: WV/23966/Un/46  
 Rotation: 0  
 Pressure (mBar):  $1.09 \times 10^{-9}$   
 Date: 01.08.2017  
 File: a0540\_2.asi

		300K	77K	4.2K	1K
dark	$\mu$ [cm <sup>2</sup> / Vs]				
	n [cm <sup>-2</sup> ]				
illum	$\mu$ [cm <sup>2</sup> / Vs]				
	n [cm <sup>-2</sup> ]				

Layer	Loop	T [°C]	Dur. [s]	Thickn. [nm]	growth rate
Ga		300.0	112.7	11.2	GaAs 0.099 nm/s
					Comment mask M15_2  @ Ga deposition cryo pump_off 40ML  (Grown by V. Zolatanosha)



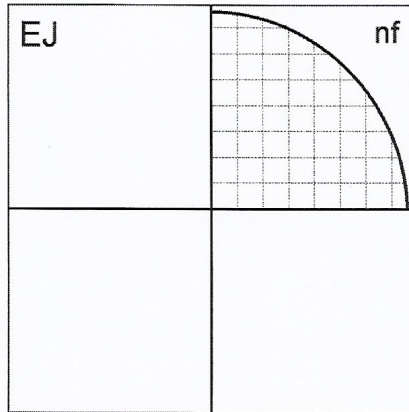


Sample: **A0558\_1**  
 Material: GaAs  
 Orientation: (100)  
 Wafer: WV/23966/Un/49  
 Rotation: 0  
 Pressure (mBar):  $3.59 \times 10^{-8}$   
 Date: 10.08.2017  
 File: a0558\_1.asl

**300K                      77K                      4.2K                      1K**

dark	$\mu$ [cm <sup>2</sup> / Vs]				
	n [cm <sup>-2</sup> ]				
illum	$\mu$ [cm <sup>2</sup> / Vs]				
	n [cm <sup>-2</sup> ]				

Layer	Loop	T [°C]	Dur. [s]	Thickn. [nm]	growth rate
GaAs		620.0	257.2	50	GaAs 0.192 nm/s
Ga <sub>0.62</sub> Al <sub>0.38</sub> As		620.0	340.7	100	AlAs 0.099 nm/s
GaAs		620.0	2.6	0.5	GaAs 0.02 nm/s
Ga		350.0	17.4	0.34	
					Comment mask M15_2  Tpyro=560°C(590°C) As=50%=1.96E-5  1.2ML of Ga
					(Grown by V. Zolatanosha)

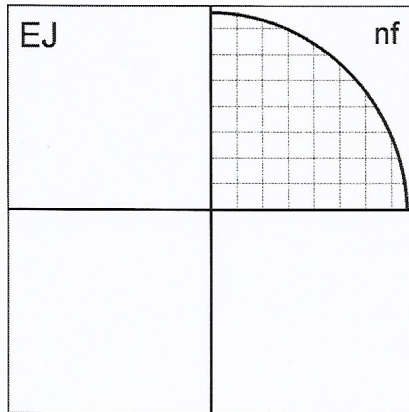


**Sample: A0558\_2**  
**Material: GaAs**  
**Orientation: (100)**  
**Wafer: WV/23966/Un/49**  
**Rotation: 0**  
**Pressure (mBar):  $3.45 \times 10^{-9}$**   
**Date: 10.08.2017**  
**File: a0558\_2.asl**

		300K	77K	4.2K	1K
dark	$\mu$ [cm <sup>2</sup> / Vs]				
	n [cm <sup>-2</sup> ]				
illum	$\mu$ [cm <sup>2</sup> / Vs]				
	n [cm <sup>-2</sup> ]				

Layer	Loop	T [°C]	Dur. [s]	Thickn. [nm]	growth rate
Ga		400.0	112.7	11.2	GaAs 0.099 nm/s
					<i>Comment</i> mask M15_2  cryo pump_off Tsub=400°C 40ML of Ga  (Grown by V. Zolatanosha)



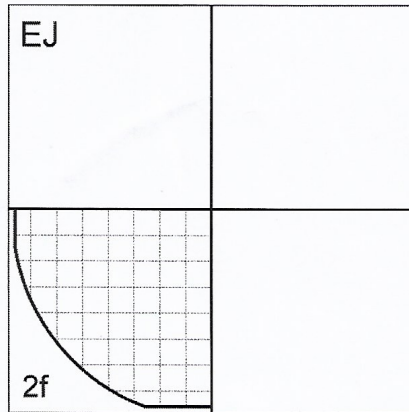
**Sample:** A0584\_1  
**Material:** GaAs  
**Orientation:** (100)  
**Wafer:** WV/24209/Un/23  
**Rotation:** 0  
**Pressure (mBar):**  $4.11 \times 10^{-8}$   
**Date:** 29.08.2017  
**File:** a0584\_1.asl

		300K	77K	4.2K	1K
dark	$\mu$ [cm <sup>2</sup> / Vs]				
	n [cm <sup>-2</sup> ]				
illum	$\mu$ [cm <sup>2</sup> / Vs]				
	n [cm <sup>-2</sup> ]				

Layer	Loop	T [°C]	Dur. [s]	Thickn. [nm]	growth rate
GaAs		620.0	286.2	50	AlAs 0.099 nm/s
Al <sub>0.62</sub> Ga <sub>0.38</sub> As		620.0	365.3	100	GaAs 0.172 nm/s
GaAs		620.0	2.9	0.5	
					<b>Comment</b> mask M15_2  Tpyro=560°C(590°C) As=70%; As=50%=1.79E-5 without saturation layer  (Grown by V. zolatanosha)







**Sample: A0601\_2**  
**Material: GaAs**  
**Orientation: (100)**  
**Wafer: WV/24209/Un/10**  
**Rotation: 0**  
**Pressure (mBar):  $3.0 \times 10^{-9}$**   
**Date: 20.09.2017**  
**File: a0601\_2.asl**

		300K	77K	4.2K	1K
dark	$\mu$ [cm <sup>2</sup> / Vs]				
	n [cm <sup>-2</sup> ]				
illum	$\mu$ [cm <sup>2</sup> / Vs]				
	n [cm <sup>-2</sup> ]				

Layer	Loop	T [°C]	Dur. [s]	Thickn. [nm]	growth rate
Ga		100.0	7.8	0.77	GaAs 0.099 nm/s
					<b>Comment</b> mask M15_2  cryo pump_off 2.75 ML of Ga annealing at 400°C for 5 min   (Grown by V. Zolatanosha)

# List of Publications

Parts of this thesis have already been published in journals and conference proceedings.

## Scientific publications

1. V. Zolatanosha and D. Reuter, *Robust  $Si_3N_4$  masks for 100 nm selective area epitaxy of GaAs-based nanostructures*, *Microelectronic Engineering*, 180 (2017).
2. V. Zolatanosha and D. Reuter, *Site-controlled droplet epitaxy of GaAs quantum dots by deposition through shadow masks*, *Journal of Vacuum Science Technology B*, 36 (2018).

## Submissions to conferences

1. V. Zolatanosha and D. Reuter, *Microfabricated SiN-masks for selective area epitaxy of InAs and GaAs*, DPG Spring Meeting. Regensburg, 2016.
2. V. Zolatanosha and D. Reuter, *Robust  $Si_3N_4$  masks for 100 nm selective area epitaxy of GaAs-based nanostructures*, E-MRS Fall Meeting. Warsaw, 2016.

3. V. Zolatanosha and D. Reuter, *Site-controlled droplet epitaxy of GaAs quantum dots by deposition through shadow masks*, 33rd North American Molecular Beam Epitaxy Conference. Galveston, 2017.
4. V. Zolatanosha and D. Reuter, *Site-controlled Ga droplet epitaxy by deposition through shadow masks*, The Austrian MBE Workshop. Vienna 2017.



# Acknowledgements

At this point, I would like to express my gratitude to everyone who have helped me in one way or another to accomplish this work.

First of all, I want to thank **Prof. Dr. Dirk Reuter** who accepted me as a PhD candidate under his supervision and gave me the opportunity to work on this interesting topic in his group of Optoelectronic Materials and Devices (OMD). His continuous support and encouraging, his kindness and understanding together with his great professional expertise helped me a lot on my way to this thesis.

Secondly, I thank **Prof. Dr. Cedrik Meier**, **Prof. Dr. Ulrich Hiller-  
ingmann** and **Prof. Dr. Christine Silberhorn** for making the scientific equipment and knowledge of their groups available to be used for this dissertation.

I also thank **Prof. Dr. Cedrik Meier** for his work as my second reviewer.

I would like to thank to all the OMD colleagues for the great atmosphere they have created during the working and non-working time, which we spent together, as well as for their kind support.

- I would like to thank **apl. Prof. Dr. Donat J. As** for his advices and recommendations, both technical and administrative.
- I am very thankful to my colleague and friend **Dr. Stepan Shvarkov**

for introducing me details of OL, PECVD, RTA systems and other important processes, for his assistance during my work in the cleanroom as well as for his guidance and many helpful discussions during the thesis writing.

- I am grateful to **Dr. Nand Lal Sharma** for his help during my work in the cleanroom at any time.
- Many thanks to my office-mate **Bastian Aisenbrey** for the productive working atmosphere as well as for his technical knowledge and support at any point.
- I thank **Anja Blank** for her administrative support and for being such a reliable person.
- I acknowledge also my other (ex-)colleagues **Dr. Sarah Blumenthal, Dr. Alexander Trapp, Dr. Tobias Wecker, Dr. Michael Deppe, Tobias Henksmeier, Timo Langer, Siegfried Igges, Falco Meier, Fabian Tacken** and **Jannick Alexander Saatz** for a pleasant and productive working atmosphere. Personally, I would thank to **Tjorven Rebeccah Christin Grottemeyer-Bagnall** for her help to improve my grasp on the English language.

I would like to thank all coworkers of my collaboration partner at the University of Bochum. Special thanks to **Prof. Dr. Andreas Wieck, Nadine Viteritti, Dr. Sergej Markman, Dr. Rüdiger Schott** and **Sascha René Valentin** for administrative and technical support.

Furthermore, I am very thankful to the **Bundesministerium für Bildung und Forschung** via the *Q.com* program and the **Deutsche Forschungsgemeinschaft** via the *TRR 142* for the financial support.

I cannot end this section without expressing my gratitude for the continuous support I received from **my parents** and my husband **Guwan**. I am thankful for their love, understanding and patience. I thank my lovely daughter **Eva**, who was accompanying me at the last stages of the experimental part and came to the world just in time to provide the best motivation during the thesis writing.